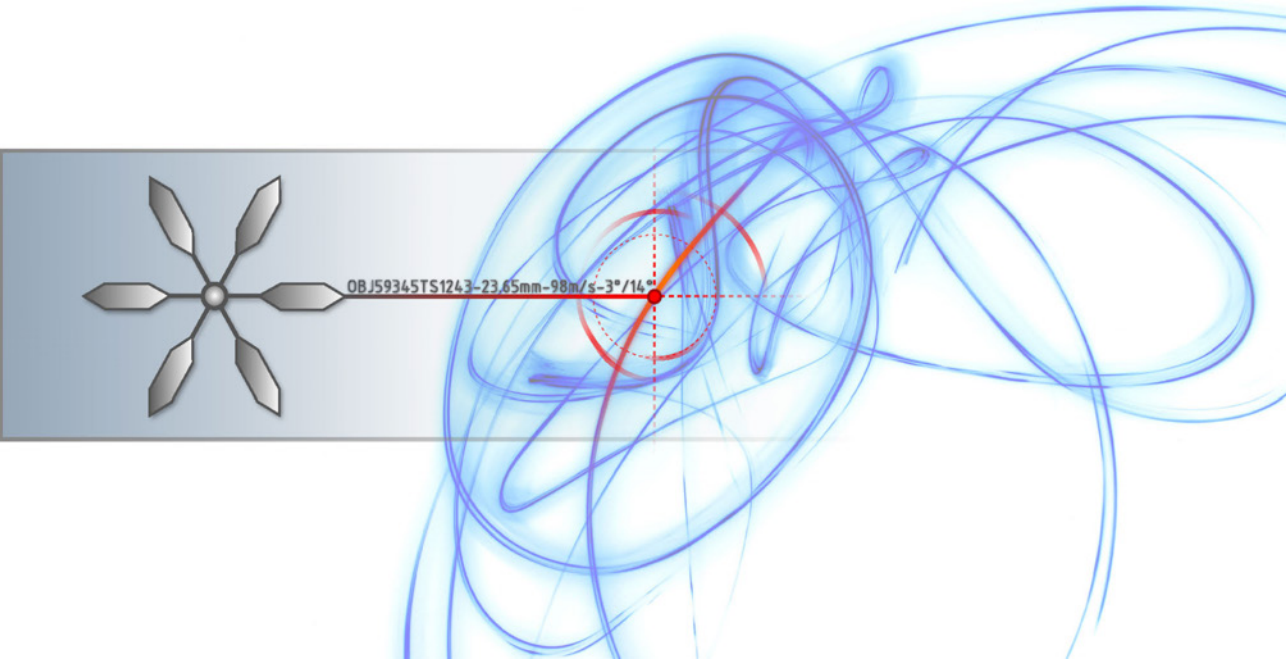

FAU Forschungen, Reihe B, Medizin, Naturwissenschaft, Technik 2

Gabor Vinci

Six-Port Based Direction Finding and Ranging

FAU UNIVERSITY PRESS

Gabor Vinci

Six-Port Based Direction Finding and Ranging

FAU Forschungen, Reihe B

Medizin, Naturwissenschaft, Technik

Band 2

Herausgeber der Reihe:
Wissenschaftlicher Beirat der FAU University Press

Gabor Vinci

Six-Port Based Direction Finding and Ranging

Sechstor-basierte Ortung und Entfernungsmessung

Erlangen
FAU University Press
2014

Bibliografische Information der Deutschen Nationalbibliothek:
Die Deutsche Nationalbibliothek verzeichnet diese Publikation in der Deutschen Nationalbibliografie; detaillierte bibliografische Daten sind im Internet über http://dnb.d-nb.de abrufbar.

Verlag und Auslieferung:

FAU University Press, Universitätsstraße 4, 91054 Erlangen

Druck: docupoint GmbH

ISBN: 978-3-944057-16-3
ISSN: 2198-8102

Six-Port Based Direction Finding and Ranging

Sechstor-basierte Ortung und Entfernungsmessung

Der Technischen Fakultät der
Friedrich-Alexander-Universität Erlangen-Nürnberg
zur Erlangung des Grades
DOKTOR-INGENIEUR

vorgelegt von
Gabor Vinci
aus Este

Name: Gabor Vinci
E-Mail 1: gabor.vinci@fau.de
E-Mail 2: gabor.vinci@ieee.org
Tel.: +49 (0)176 23 959797

Als Dissertation genehmigt von
der Technischen Fakultät der
Friedrich-Alexander-Universität Erlangen-Nürnberg

Tag der mündlichen Prüfung: 05. Februar 2014
Vorsitzende des Promotionsorgans: Prof. Dr.-Ing. habil. Marion Merklein
Gutachter: Prof. Dr.-Ing. Dr.-Ing. habil. Robert Weigel
Prof. Dr.-Ing. Reinhard Knöchel

When I observe the luminous progress and expansion of natural science in modern times, I seem to myself like a traveler going eastwards at dawn, and gazing at the growing light with joy, but also with impatience; looking forward with longing to the advent of the full and final light, but, nevertheless, having to turn away his eyes when the sun appeared, unable to bear the splendor he had awaited with so much desire.

Leonardo da Vinci

Abstract

Direction finding and ranging techniques find a large number of applications from security and military purposes through the medical sector to industrial automation. As for the latter application scenario, advanced positioning and sensor feedback tasks in automation processes often require distance displacement detection, for example, to measure and track the movement of robots. Several automation technologies rely on high precision positioning sensors to track linear as well as rotational movements of various machinery.

As an example for medical applications within this field, high measurement accuracy is required to guarantee the safety of patients and the quality of therapies through vital sign monitoring systems. For instance, heartbeat and breath rate monitoring is of primary interest and can be achieved with particularly accurate displacement detection techniques.

Generally speaking, within this large variety of environments, several different requirements need to be satisfied. This is often a great challenge for sensors that rely on different physical principles, depending on which application they have been designed for.

In this work, an innovative measurement technique based on the Six-Port receiver principle will be presented. The purpose of this dissertation is to introduce the Six-Port receiver as a valid technology for direction finding and distance measurement tasks satisfying the requirements imposed by certain applications addressed in this work.

The measurement properties of the Six-Port receiver recently raised the interest of the scientific community. The excellent phase resolution offered by this alternative microwave receiver leads to high accuracy distance and angular measurement capabilities. Furthermore, the Six-Port technology proves to be immune to several undesired effects influencing common distance and rotation measurements.

Historically, the Six-Port receiver was used as a reflectometer. Following the evolution of radar and microwave technology the Six-Port receiver has been also used as an alternative vector network analyzer for sensing applications. Mainly due to the progress in material and process technology the Six-Port technique has lately found several other implementation possibilities.

Furthermore, the Six-Port receiver can be easily integrated on Monolithic Microwave Integrated Circuit (MMIC) technology as an alternative receiver for millimeter-wave frequencies.

The presented measurement techniques based on the Six-Port receiver and the evaluation of their performance are the purpose of this work and will be addressed in dedicated chapters along with results from hardware prototypes developed by the author during the research activities on this topic. With the proposed techniques angular measurements in the range of a few milli-degrees for direction of arrival detection as well as a distance measurement resolution in a one-digit micrometer range have been achieved.

Zusammenfassung

Abstandsmessung und Ortung sind für verschiedenste Applikationen nicht nur im Bereich der Sicherheits- und Verteidigungstechnik sondern auch für die Medizintechnik, die Industriemesstechnik und die Automatisierungstechnik besonders relevant. Im Industriebereich erfordern hochkomplexe Positionierungsverfahren von Industriemaschinen und Robotern eine zuverlässige und genaue Abstands- und Winkelmessung, um die Informationsgewinnung im Steuergerät zu ermöglichen. Die Funktionsweise vieler derartiger Applikationen hängt von der Sensorinformation ab, zum Beispiel um lineare Bewegungen und Rotationsbewegungen zu erfassen.

Als Beispiel für medizinische Anwendungen, die von einer genauen Abstandermittlung profitieren können, ist die Vitalparameterüberwachung bei Patienten während medizinischer Behandlungen zu nennen. Damit wird die Sicherheit und Qualität der Therapie insgesamt verbessert. Die Herzschlag- und Atemdetektion ist besonders wichtig im medizinischen Umfeld und kann mittels einer hochgenauen Messung der Abstandsänderung zum Patienten durchgeführt werden, da die Atemzyklen eine Ausdehnung des Brustkorbs verursachen und Herzschläge kleinste periodische Vibrationen auf die Haut hervorrufen.

Die unterschiedlichen Anforderungen dieser vielfältigen Applikationsszenarien stellt eine Herausforderung für die Implementierung des Messsystems dar. In dieser Arbeit wird eine innovative Messtechnik basierend auf der Sechstor Empfängerarchitektur präsentiert. Ziel ist es, die Sechstor-Empfängertechnik als zuverlässiges Verfahren für Abstands- und Richtungsschätzung bei einer Reihe von Anwendungen einzuführen.

Die besonderen Funktionen der Sechstor-Empfängertechnik haben in letzter Zeit das wissenschaftliche Interesse geweckt. Die hochgenaue Phasenauflösung dieses alternativen Empfängers führt zu präzisen Abstands- sowie Richtungsmessungen. Zudem besitzt die Sechstor-Empfängertechnik eine hohe Robustheit gegenüber unerwünschten Effekten, die traditionelle Abstands- und Richtungsschätzungstechniken beeinflussen.

Die Sechstor-Empfängertechnik ist zunächst als Messverfahren zur Bestimmung von Reflexionen in Mikrowellenschaltungen eingeführt worden. Dank

der Entwicklungen in der Radar- und Mikrowellentechnik ist der Sechstorempfänger später auch als alternativer vektorieller Netzwerkanalysator für verschiedene Sensorapplikationen verwendet worden. Auf Grund der Entwicklungen in der Werkstofftechnik und in der Prozesstechnik hat die Sechstortechnik in den letzten Jahren viele neue Anwendungsmöglichkeiten gefunden. Eine weitere Entwicklung des Sechstor-Empfängers in monolithisch integrierter Mikrowellenschaltungstechnik ermöglicht einen hohen Integrationsgrad und die Implementierung des Sechstors als alternativen Millimeterwellenempfänger.

Verschiedene Sechstor-basierte Messtechniken und Messergebnisse werden in dieser Arbeit vorgestellt und diskutiert. Dedizierte Hardwaredemonstrationen, die vom Autor während der Forschungsarbeit entwickelt wurden, werden näher dargestellt. Es werden Winkelmessgenauigkeiten im Milligrad-Bereich für Richtungsmessverfahren sowie Abstandsmessgenauigkeiten im einstelligen Mikrometerbereich erreicht.

Contents

List of Figures

1 Introduction

1.1 Direction Finding and Ranging

The definition of direction finding and ranging can assume several different interpretations depending in which context it is introduced. A clear definition is hereby proposed to ease the understanding of the concepts and techniques described hereafter. The purpose of direction finding is to estimate a certain angular quantity with respect to a reference, that identifies a certain target.

As for ranging, this implies the estimation of a distance from a reference point to the observed target. In other words, direction finding applies to finding the alignment of the target to the own position and ranging applies to distance metering with targets. Combining direction finding and ranging repetitively through time results in the tracking of the target under observation.

Direction finding and ranging are commonly referred to radio and microwave technology, mainly through RADAR (RAdio-Detection-And-Ranging) systems or similar devices being able to detect and localize passive targets as well as active transmitting radio sources. Nevertheless, there are several other direction finding and ranging techniques that are based on other physical principles.

In this work, direction finding and ranging will be generally referred, unless otherwise specified, to radar-like techniques with the purpose of detecting, localizing and tracking targets through microwave measurements, making use of the propagation and material interaction properties of electromagnetic waves.

Within this defined framework, direction finding and ranging techniques are of major interest for a large number of applications in different fields. Security and military applications include advanced radar techniques for tar-

get detection, localization and tracking. Techniques hereby involved have been developed roughly starting from Second World War, with primitive early warning hostile airborne threat detection, up to nowadays sophisticated radar based automatic missile guidance systems.

Direction finding and ranging techniques are interesting not only for security and defense purposes, but also for a large variety of different fields, for instance in industrial automation. Advanced positioning and sensor feedback technology in automation processes often requires distance and displacement detection, for example, to measure and track the movement of robots. Several automation technologies rely on high precision positioning sensors to track linear as well as rotational movements of various machinery. The tracked positioning information provided by the sensor interface determines the accuracy of the positioning system, thus, the quality of the overall industrial automation process.

Another field in which ranging techniques are of great interest, is the medical environment where applications such as heartbeat and breath rate monitoring require high measurement accuracy to guarantee the safety of patients and the quality of therapies and vital sign monitoring systems. For instance, the ability to observe the breath and heartbeat of a patient over night allows to detect sleep disorders or anomalies. Nowadays, this can be achieved by monitoring a patient contact-free from a distance with radar technology featuring very high distance detection accuracy. The patient's body movements can be detected and analyzed to reconstruct breath rate and heartbeat.

Generally speaking, within this large variety of environments, several different measurement requirements need to be satisfied. This is often a great challenge for many sensors that rely on different physical principles, depending on which application they have been designed for. As an example, the tough requirements imposed by industrial environments often lead to great challenges for these kind of sensors.

A large variety of radar technologies has been developed in the last decades satisfying the requirements of the above mentioned applications. New emerging technologies are constantly developing within the scientific community and the industry featuring better and better detection properties. In the following chapters, a general categorization of different measurement scenarios and receiver topologies will be given, to ease the understanding of the innovative direction finding and ranging technique hereby proposed. To perform direction finding and ranging of passive targets as well as of ac-

tive sources a microwave receiver is needed. The information used to localize the target is contained in the received signal. Therefore, the properties of the receiver used for the direction finding and ranging applications are essential to reach the detection performances for the different applications addressed.

In this work, the Six-Port technique is introduced to perform different kind of direction finding and ranging measurements. Throughout the basic theory describing the Six-Port receiver architecture, innovative measurement concepts will be introduced purposely addressing specific application scenarios to demonstrate the benefits of this alternative receiver technology.

The Six-Port receiver concept works with four additive superpositions of two radio frequency (RF) input signals resulting in constructive or destructive interference in a way similar to optical interferometry. Thus, the Six-Port receiver is often called microwave interferometer. The relationship between the resulting output signals expressed by the Six-Port receiver theory allows the detection of the relative phase shift between the two input signals. The direction finding and ranging information lies in the relative phase difference between the two input signals at the Six-Port receiver. A detailed explanation of the Six-Port technique will be given in chapter 4.

Historically, the Six-Port receiver has been used as a reflectometer. Following the evolution of radar and microwave technology the Six-Port receiver has been also used as an alternative vector network analyzer for sensing applications and as a transceiver for high-speed data transmission [1]. Mainly due to the progress in material and manufacturing process technology the Six-Port technique has lately found several other implementation possibilities. For instance, the Six-Port receiver can be easily integrated on Monolithic Microwave Integrated Circuit (MMIC) technology as an alternative receiver for very high millimeter-wave frequencies [2].

The Six-Port receiver has also found various exotic applications involving direction finding and ranging, where other techniques show several drawbacks. For instance, the Six-Port receiver can be used in automotive workshops to adjust and align the long-range radar sensor of a car. Automatic distance control used in Automatic Cruise Control (ACC) systems, is a technology of major interest for the automotive industry as regulations about traffic safety become more and more restrictive, requiring ACC systems to be available on all vehicles by law in the future. These systems periodically need a high-accuracy alignment and calibration to guarantee safety standards. The main advantage of the Six-Port as an alignment tool lies in its

excellent phase resolution thus leading to very high misalignment detection accuracy, that is a kind of direction finding problem. An insight on this particular application is given in section 10.1 [3].

1.2 Description and Aim of This Work

In this work, different innovative measurement techniques based on the Six-Port receiver principle will be presented. The purpose of this dissertation is to introduce the Six-Port receiver as a valid technology for direction finding and distance measurement tasks satisfying the requirements imposed by different applications.

The measurement properties of the Six-Port receiver recently raised the interest of the scientific community and of the industry. The excellent phase resolution of the Six-Port receiver leads to high accuracy distance and angular measurement capabilities.

Several innovations to the state-of-the-art Six-Port technique are hereby presented, leading to the solution of certain problems related to the Six-Port receiver (such as ambiguity issues) that where questioning the applicability of this receiver architecture for many application scenarios.

For sake of completeness, it has to be mentioned, that the Six-Port technique does not only refer or is limited to microwave technology. For instance, several applications in optics also benefit from the properties of this particular receiver. Nevertheless, the methods for direction finding and ranging described in this work are based on the propagation and scattering effects of electromagnetic waves in the radio frequency and microwave spectrum. Furthermore, other methods based on optical, acoustical and mechanical principles exist but will not be considered since they are not in the focus of this work.

2 Direction Finding Techniques

Hereby, an overview will be given of direction finding techniques, also called Direction of Arrival (DOA) detection of a radio signal emitted from a source. The purpose of direction finding techniques is to estimate the direction of propagation of a detected electromagnetic wave with respect to a well known geometrical reference coordinate system. The final goal is to locate the transmitting source or a reflecting target once the propagating direction of the wave is known.

The topic of direction finding has been extensively investigated for location and tracking signal sources in both civilian and military applications [4]. A large number of advanced DOA algorithms have been proposed, working on digital signal processing in baseband. These methods based on algorithms such as MUSIC or ESPRIT, are described in dedicated literature [5]. The overall basics of DOA estimation are described in reference textbooks on the topic, such as "Classical and Modern Direction of Arrival Estimation" by Engin Tuncer and Benjamin Friedlander [6]. The reader is encouraged to browse this reference book to gain an insight in the wide topic of DOA estimation.

The purpose of this chapter is to introduce the very basics of DOA estimation from the physical point of view of electromagnetic wave propagation, without introducing the digital signal processing analysis mostly used by modern techniques, as presented in the above mentioned literature. It will be shown, that DOA estimation basically relies on amplitude or phase evaluations of received signals with one, two or more antennas (or antenna arrays), independently from the type of the signal received.

For sake of clarity, from now on only active sources will be addressed. Thus, the DOA detection will focus on the estimation of the direction of propagation of electromagnetic waves emitted from a source. Nevertheless, the concepts introduced hereon are valid also for other targets such as passive scatterers where the direction of propagation of the reflected wave has to be

detected in order to estimate their position.

Obviously, to locate the target, the DOA information is not sufficient since the ranging information is needed as well. Nevertheless, the purpose of the techniques hereby described is to evaluate the angular information only.

2.1 Properties of an Electromagnetic Wave

Before introducing the direction finding techniques and its related concepts, a brief summary about electromagnetic wave propagation and its main properties will be given. Commonly, a time-harmonic complex wave[1] propagating into a certain type of medium is identified by a wave vector, with a magnitude and a direction in space. A complex propagating wave $\underline{\vec{\psi}}$ can be described as [9]:

$$\underline{\vec{\psi}}(\vec{r},t) = A(\vec{r})\ \cos(\vec{k}\cdot\vec{r}-\omega t+\phi) + jA(\vec{r})\ \sin(\vec{k}\cdot\vec{r}-\omega t+\phi), \tag{2.1}$$

where $\vec{r}$ is the unity three dimensional direction vector, A is the amplitude of the wave, ω the angular frequency of oscillation, ϕ the phase and $\vec{k}$ the wave vector. Its magnitude $\left|\vec{k}\right|$ is the wavenumber

$$\left|\vec{k}\right| = \frac{2\pi}{\lambda}, \tag{2.2}$$

that is inversely proportional to the wavelength λ, and its direction identifies the wave's direction of propagation if certain conditions are satisfied. These conditions will be explained hereafter. Without loss of generality, from now on the purely real definition of a wave will be used, to ease readability and understanding:

$$\vec{\psi}(\vec{r},t) = A(\vec{r})\ \cos(\vec{k}\cdot\vec{r}-\omega t+\phi). \tag{2.3}$$

Two other relevant quantities that describe a propagating wave are the phase velocity $\vec{v}_p$ and the group velocity $\vec{v}_g$. The phase velocity is given in terms of the wave's angular frequency ω and wave vector $\vec{k}$ by [10]

[1] For sake of completeness, the definition of a general time-harmonic wave in complex form is hereby reported. However, in dedicated literature, this is sometimes described as a real quantity (see eq. (2.3)). This does not have to be confused with the so called "Wave equation" [7,8] also used in electromagnetics.

$$\vec{v}_p = \frac{\omega}{\vec{k}} = \frac{1}{\sqrt{\mu\epsilon}}\,\vec{r}, \tag{2.4}$$

with ϵ being the dielectric permittivity and μ the magnetic permeability of the medium in which the wave propagates. The phase velocity describes how far each wavefront progresses per unit time. However, phase velocities cannot be measured directly, since no physical signal is a pure single tone sinusoid and all finite-duration signals have more than one frequency component. Therefore, if $\epsilon(\omega)$ is a function of frequency, as it is usually the case in dielectric media, then each frequency component will have its own phase velocity. Defining c as the velocity of an electromagnetic signal in free space ($c = \frac{1}{\sqrt{\mu_0\epsilon_0}}$), for a plane time-harmonic wave in a dielectric medium it can be shown that [10]

$$\vec{v}_p(\omega) = \frac{\omega}{\vec{k}(\omega)} = \frac{1}{\sqrt{\mu\epsilon(\omega)}}\,\vec{r} = \frac{c}{n(\omega)}\,\vec{r}, \tag{2.5}$$

$$n(\omega) = \sqrt{\epsilon_r(\omega)}, \tag{2.6}$$

where $n(\omega)$ described by eq. (2.6) is the refractive index and $\epsilon_r(\omega) = \epsilon(\omega)/\epsilon_0$ is the relative dielectric permittivity of the medium, with the permittivity of vacuum $\epsilon_0 \approx 8.854187 \cdot 10^{-12} F \cdot m^{-1}$. The different signal components will travel at different velocities, and the signal will become distorted because the sum of the various sinusoidal components changes with distance. Such dielectrics are called dispersive media[2].

On the other hand, the group velocity is the velocity with which the wave's envelope (shape of the wave's amplitude, or modulation) propagates through a medium. The group velocity is defined by [10]

$$\vec{v}_g = \frac{\delta\omega}{\delta\vec{k}(\omega)} = \frac{d\omega}{d\vec{k}} = \frac{1}{d\vec{k}(\omega)/d\omega}. \tag{2.7}$$

Only for non-dispersive media, in which ϵ and μ are not functions of frequency, the group and phase velocities are equal. In this case [10]:

[2] The phenomenon of dispersion is covered in [10] where the fundamental difference between normal dispersion (phase velocity decrease with increasing frequency $\vec{v_p} \propto 1/\omega$ or the refractive index described in eq. (2.6) is $n(\omega) \propto \omega$) and anomalous dispersion where $\vec{v_p} \propto \omega$ and $n(\omega) \propto 1/\omega$ is explained.

$$\vec{k} = \omega\sqrt{\mu\epsilon}\,\vec{r} \Rightarrow d\vec{k}/d\omega = \sqrt{\mu\epsilon}\,\vec{r}, \tag{2.8}$$

$$\vec{v_g} = \frac{d\omega}{d\vec{k}} = \frac{1}{\sqrt{\mu\epsilon}}\,\vec{r} = \vec{v_p}. \tag{2.9}$$

In other words, all frequency components travel at the same velocity in non-dispersive media, so that there is no distortion as the wave propagates.

Considering an electromagnetic wave, with an electric field $\vec{E}$ and a magnetic field $\vec{B}$ (such that $\vec{B} = \mu\vec{H}$) eq. (2.3) can be used to describe the electric and magnetic fields with a simplified sinusoidal solution to the general electromagnetic wave equation as [10]:

$$\vec{E}(\vec{r_E}, t) = \vec{E_0}(\vec{r_E})\cos(\vec{k}\cdot\vec{r_E} - \omega t + \phi), \tag{2.10}$$

$$\vec{B}(\vec{r_B}, t) = \vec{B_0}(\vec{r_B})\cos(\vec{k}\cdot\vec{r_B} - \omega t + \phi). \tag{2.11}$$

Eq. (2.10) and (2.11) imply the linearity of Maxwell's equations in lossless isotropic media, such as vacuum [10]. Assuming that the $\vec{E}$ and $\vec{B}$ fields feature a single angular frequency ω and by using Maxwell's equations, the electromagnetic wave equations (2.10) and (2.11) can be simplified to the Helmholtz equations [11]:

$$\left(\nabla^2 + \vec{k}^2\right)\vec{E} = 0 \Rightarrow \nabla^2\vec{E} + \omega^2\mu\epsilon\vec{E} = 0, \tag{2.12}$$

$$\left(\nabla^2 + \vec{k}^2\right)\vec{H} = 0 \Rightarrow \nabla^2\vec{H} + \omega^2\mu\epsilon\vec{H} = 0. \tag{2.13}$$

Therefore, a generic electromagnetic wave with angular frequency ω can be expressed with eq. (2.12) and (2.13). A three-dimensional general solution for the Helmholtz equations (2.12) and (2.13) can be expressed with the help of spherical Bessel functions. The interested reader can refer to dedicated literature on electromagnetic field theory and its analytical description [10–14].

The direction in which the wave propagates is defined as the direction of the wave's energy flow, or the group velocity $\vec{v}_g$. This is identified by the direction of the time average Poynting vector $\vec{P}$ (average power density) [15]:

$$\vec{P}(\vec{r}) = \frac{1}{2}\Re\left\{\underline{\vec{E}} \times \underline{\vec{H}}^*\right\}, \tag{2.14}$$

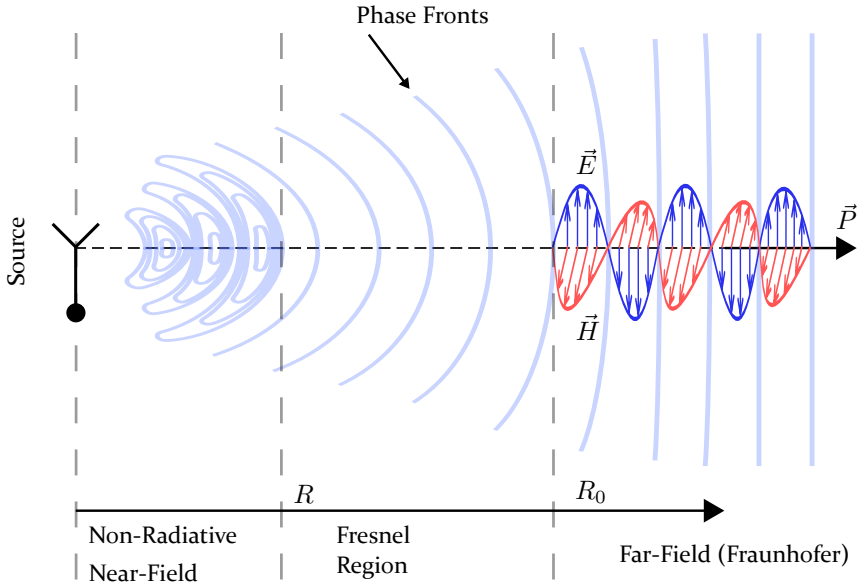

Figure 2.1: Representation of the near-field, Fresnel region as well as far-field of a radiating antenna, according to [16]. Boundaries for the different regions are marked by R and R_0.

Its has to be remarked that eq. (2.14) represents the time average power transmitted in the direction of $\vec{r}$ and is derived from the definition of the complex Poynting vector

$$\underline{\vec{P}}(\vec{r}) = \underline{\vec{E}} \times \underline{\vec{H}}^{*}. \tag{2.15}$$

Eq. (2.14) can be derived from eq. (2.15) with the help of the complex Poynting vector theorem[3]. Additionally, the wave vector is oriented in the direction of the phase velocity $\vec{v}_p$. This means that the wave vector is orthogonal to constant phase surfaces, also called wavefronts.

The orientation of the wave vector $\vec{k}$ coincides with that of the Poynting vector $\vec{P}$ for waves propagating in lossless isotropic media. In this case, the phase velocity and the group velocity are equal as shown in eq. (2.9). If the propagation takes place in lossy media, $\vec{k}$ does not identify the direction

[3] The derivation of the complex Poynting vector theorem from Maxwell's equations can be found in [7] at page 37 / 38.

of propagation of the wave. The wave has to be homogeneous in order to have the wave vector matching the direction of propagation. If the wave is homogeneous, constant phase surfaces feature also constant amplitude values. For a wave propagating in lossy media, this cannot be satisfied. In this case the wave is inhomogeneous, featuring constant phase surfaces that differ from constant amplitude wavefronts [17].

It has to be remarked that the wave vector $\vec{k}$ is defined to be always orthogonal to surfaces of constant phase. Nonetheless, from what stated above, if a wave propagates in a lossy medium, the wave will be inhomogeneous. Thus $\vec{k}$ will not identify the direction of propagation of the wave [18][4].

Therefore, from now on, the Poynting vector $\vec{P}$ will be used to describe the direction of propagation of a wave, even if it is assumed that the propagation takes place in a lossless isotropic medium under ideal conditions (vacuum) and that the propagating wave is considered as a plane wave with Transverse ElectroMagnetic (TEM) propagation properties. Assuming that the emitted propagating wave features TEM properties[5] (i.e. a plane-wave[6]), it can be therefore stated that DOA detection consists in the estimation of the wave's Poynting vector $\vec{P}$.

It has to be mentioned that the properties of the wave and therefore the possible principles and techniques of direction finding strongly depend on the electric distance from the radiating source and on the source type itself [16]. Generally, three possible distance ranges from the transmitter can be specified [20]:

- non-radiative near-field (reactive near-field),
- radiative near-field (Fresnel region),
- far-field (Fraunhofer region).

These regions are depicted in Fig. 2.1. The non-radiative near-field surrounds the transmitting antenna within a range R. The electromagnetic field in this region features local electric and magnetic field maximas as well

[4] The effect that the wave vector does not necessarily identify the direction of propagation of a wave in lossy anisotropic media and that the wave's energy flow may differ from $\vec{k}$ has been investigated by Musgrave who described this phenomenon in his article from 1959 [19].

[5] TEM waves are extensively explained in [11] at page 95. Plane waves are also examples of TEM waves, since there are no field components in the direction of propagation.

[6] The exact definition of a plane wave can be found in [11]. Furthermore, at page 15 the Helmholtz equations (2.12) and (2.13) are simplified for plane waves in lossless medium for a simple time domain representation. The interested reader is invited to follow this reference for a comprehensive description.

as minimas with accumulation of electric and magnetic energy in local resonating modes around the radiator. In this region, an electromagnetic wave is being radiated outward and a reactive component to the electromagnetic field (with local energy storage) is also present. This energy is swapped from the antenna to the non-radiative near-field [20].

After that, the radiative near-field begins where the generated wave starts to propagate with quasi TEM properties. The radiative near-field, or Fresnel region, is defined up to a range R_0 from the antenna [20]. The radiative near-field features reactive field components that can be neglected since it is too far from the antenna. The mutual coupling of the fields with the antenna cannot efficiently store energy as in the reactive near-field. Thus, in the radiative near-field the energy is nearly all radiant [20].

The far-field (or Fraunhofer Region) is defined for a distance larger than R_0, although a continuous transition between these zones is present in which both near-field and far-field effects are taking place. In this region, near-field behavior (local electric and magnetic energy accumulation) decays leaving far-field effects as dominant interactions [20]. Only within the far-field region the propagating wave features plane phase fronts and TEM properties [20]. In other words, "the spherical wavefront radiated by the source becomes a close approximation to the ideal planar phase front of a plane wave. This approximation applies over the aperture area of the antenna, and so depends on the maximum dimension of the antenna" [11]. The ranges R and R_0 are defined as [11, 20]

$$R = 0.62 \sqrt{\frac{D^3}{\lambda}}, \tag{2.16}$$

$$R_0 = 2 \frac{D^2}{\lambda}, \tag{2.17}$$

where D is the aperture of the transmitting antenna and λ is the wavelength of the electromagnetic wave. By introducing the definitions in eq. (2.16) and (2.17) a source with $D > \lambda$ can be defined as a highly directional antenna. In the far-field both $\vec{E}$ and $\vec{H}$ fields are perpendicular to the direction of propagation, therefore to the Poynting vector [21].

For sake of clarity, it is hereby initially assumed (unless elsewhere specified) that the observer is situated in the far-field region from the radiating source, therefore satisfying the TEM properties of the propagating wave. In the following, a linear polarization of the wave will be assumed, nevertheless, all conclusions are valid for arbitrary polarization schemes.

2.2 Direction-of-Arrival Detection of a Wave

A reference three dimensional Cartesian coordinate system with $\vec{x}$, $\vec{y}$ and $\vec{z}$ as orthogonal unity vectors is hereby defined (see Fig. 2.2). The complex electric field $\underline{\vec{E}}$ and the complex magnetic field $\underline{\vec{H}}$ are hereby used. In general, $\underline{\vec{E}}$ and $\underline{\vec{H}}$ vector fields can be described as complex quantities with $\vec{x}$, $\vec{y}$ and $\vec{z}$ components in space as $\underline{\vec{E}}(x, y, z)$ and $\underline{\vec{H}}(x, y, z)$. The Poynting vector can be expressed as the vector product of the two vector fields $\underline{\vec{E}}$ and $\underline{\vec{H}}$ as described in eq. (2.14).

Without loss of generality and for sake of clarity, all methods, concepts and formulas hereby proposed refer to a mono-dimensional detection of the DOA considering only an azimuthal direction of arrival angle (azimuth plane). The problem and the proposed concepts can be extended to a multidimensional detection by introducing polar coordinates and its related mathematics (azimuth and elevation).

Since the polarization of the wave is hereby assumed to be linear and a linearly polarized receiving antenna is used to detect the signal, without loss of generality, the electric field vector $\underline{\vec{E}}$ is here defined as always aligned in the same direction in space (here the $\vec{z}$ component), orthogonal to the Poynting vector $\vec{P}$ and to the magnetic field vector $\underline{\vec{H}}$ (according to the TEM properties assumed).

Thus, the problem can be now illustrated in two-dimensions on a reference plane defined by the unity orthogonal vectors $\vec{x}$ and $\vec{y}$. The Poynting vector $\vec{P}(x, y)$ lies on the (x,y) azimuth plane as well as the magnetic field vector $\underline{\vec{H}}(x, y)$ while the electric field vector $\underline{\vec{E}}(z)$ is orthogonal to the azimuth plane. $\underline{\vec{E}}$ is hereby considered as the detected signal from the receiver. This signal is a complex quantity that can be described as:

$$\left|\underline{\vec{E}}(z)\right| = \underline{E}_z = \underline{S}_{RX} = A_{RX}\, e^{j\phi_{RX}}, \tag{2.18}$$

$$\underline{S}_{RX} = A_{RX}\, \cos(2\pi f t + \phi_{RX}) + jA_{RX}\, \sin(2\pi f t + \phi_{RX}), \tag{2.19}$$

where A_{RX} is the amplitude, f the frequency and ϕ_{RX} the phase of the signal. From the observer's point of view it is therefore possible to monitor a complex received signal with amplitude and phase variations. The relevant information about the direction of the Poynting vector (hence about the propagation direction of the electromagnetic wave) can be extracted from amplitude or phase measurements on the received signal $\underline{S}_{RX}$. These techniques will be explained in the following sections.

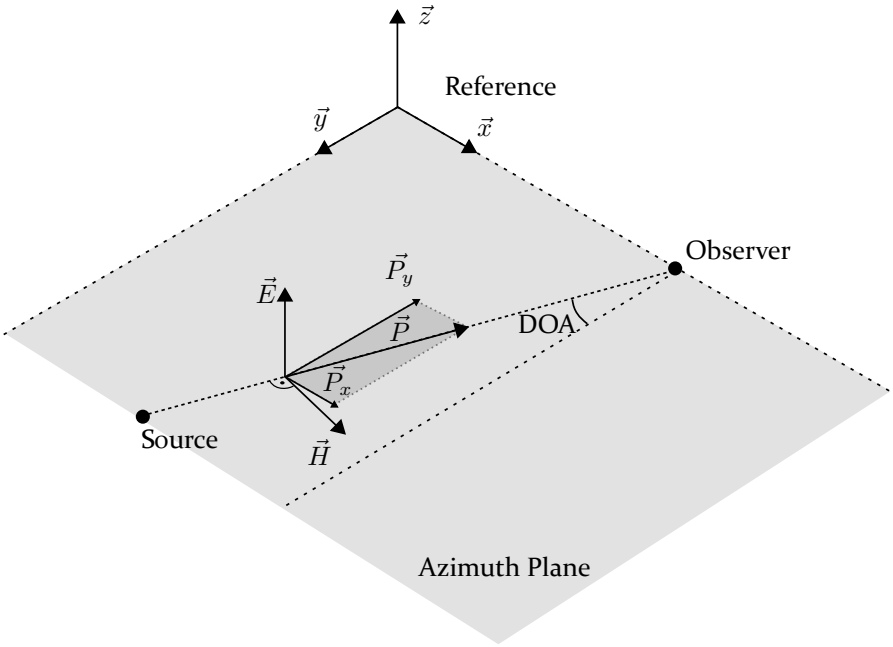

Figure 2.2: Geometrical representation of the electromagnetic wave vector fields $\vec{E}$ and $\vec{H}$ as well as the Poynting vector $\vec{P}$ with respect to the reference coordinate system.

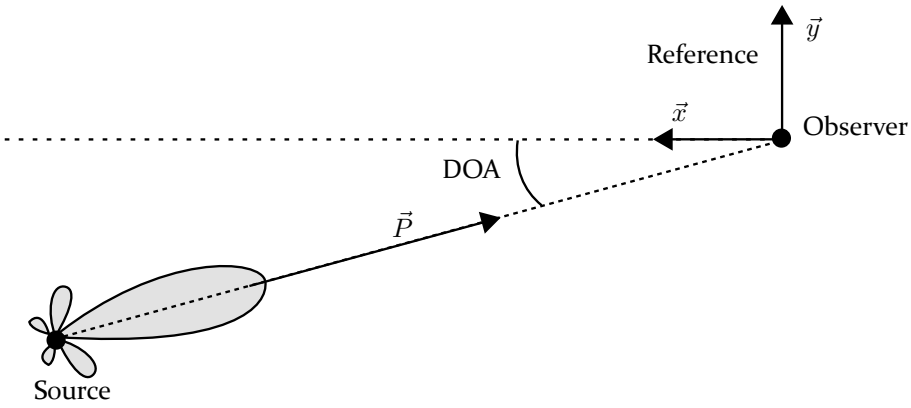

Figure 2.3: Schematical representation of a DOA detection arrangement. The position of the source is unknown and the DOA detection delivers the angular position of the source with respect to the observer's reference coordinate system.

From the beginning of this chapter it has been assumed that the purpose of DOA detection is to estimate the direction of propagation of a detected electromagnetic wave with respect to a well known geometrical reference coordinate system (set for instance by the observer) in order to estimate the position of the transmitting source (Fig. 2.3). This source has not been further specified and has been therefore assumed as a general radiating antenna with an arbitrary radiation pattern and an unknown position. The only aspect of the radiating antenna that has been introduced is the aperture D that influences the definition of the near-field and Fresnel region for the propagation properties.

Another important scenario is now being introduced. It is hereby assumed that the position of the radiating source is known (aligned to the observer on a reference axis) and that the transmitting antenna features a certain directivity with a main lobe in the far-field radiation pattern (Fig. 2.4). The generated electromagnetic wave starts to propagate towards the observer that is therefore within the main radiation lobe. The Poynting vector of the wave emitted from the radiating antenna defines the direction in which the transmitter is aligned and defines the symmetry axis of the main lobe of the radiation pattern.

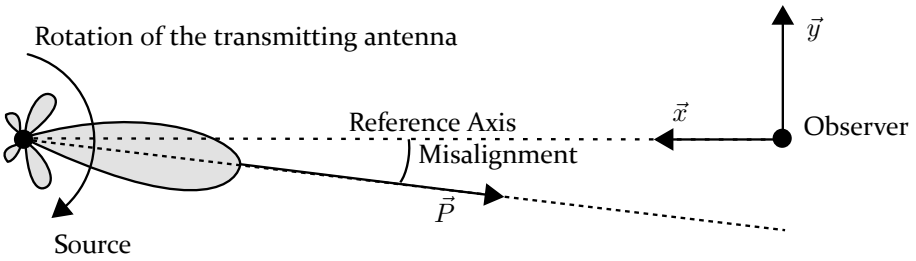

Figure 2.4: Misalignment detection concept of the transmitting source with respect to a reference axis. The position of the radiating antenna is known and the misalignment angle of the radiating antenna with respect to a reference axis is evaluated.

Since the position of the transmitter is known the purpose of the observer is to determine the orientation of the radiating antenna with respect to a geometrical reference axis between the transmitter and the observer. In other words, the alignment of the transmitting antenna with respect to a reference has to be determined. This makes sense only if the transmitting antenna features a certain directivity. A possible application is the accurate alignment of highly focused antennas for instance to adjust and calibrate au-

tomotive radar units. This application will be further discussed in section 10.1.

It is therefore important to distinguish between two measurement scenarios:

- DOA detection of a propagating wave, i.e. detection of the position of the radiating source (Fig 2.3). In this case the position of the source is unknown and the DOA detection delivers the angular position of the source with respect to the observer's reference coordinate system.
- Misalignment detection of a focused antenna (Fig 2.4). In this scenario the position of the radiating antenna is known and the misalignment angle of the radiating antenna with respect to a reference axis is evaluated (angle between the Poynting vector and the reference alignment axis connecting source and observer).

2.3 Amplitude Measurement Based Direction Finding

In this section, direction finding techniques will be discussed that make use of received signal amplitude evaluations to determine the DOA angle of a propagating wave. As introduced before, the received signal $\underline{S}_{RX}$ is a complex quantity with a certain amplitude value A_{RX}. By observing the amplitude of the signal from a single receiving antenna it is possible to detect the direction of propagation of the wave. This depends on the type of the receiving antenna.

Assuming that the receiving antenna is an isotropic radiator a change in the received amplitude does not deliver a DOA information since the antenna features an omnidirectional radiation pattern[7]. To make use of the amplitude information for DOA detection purposes the receiving antenna should feature a certain directivity, related to an antenna gain. By knowing the directivity of the receiving antenna and rotating the antenna around its axis it

[7] The definition of omnidirectional radiation pattern has to be handled carefully. As explained in [15] at page 8, an isotropic radiator is defined as a "hypothetical lossless antenna having equal radiation in all directions". Often, a Hertzian dipole is referred as an omnidirectional source. However, it has to be underlined that such a source is omnidirectional in the azimuth plane only, not in the elevation. Since in section 2.2 it has been assumed that the detection of the DOA is performed only on an azimuthal angle (azimuth plane), in this case, even a Hertzian dipole can be referred as an omnidirectional source (isotropic radiator).

is possible to determine the DOA of the received signal [22]. This is the position of the receiving antenna around its rotational axis where the maximum received signal amplitude is reached. This is the most primitive technique that has been used for DOA detection purposes since the beginning of radio location and radar technology.

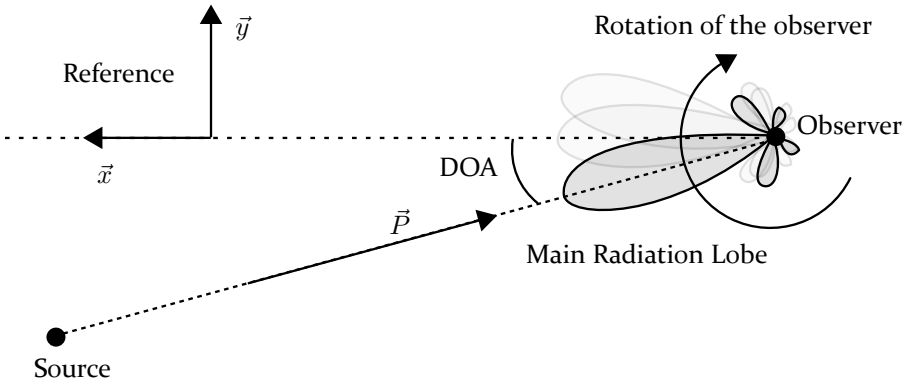

Figure 2.5: DOA detection technique making use of the amplitude information of the received signal by the observer when rotating the receiving antenna with respect to a reference coordinate system. The DOA is estimated where the maximum received signal amplitude is reached.

It is obvious that this technique is strongly dependent on the radiation pattern of the receiving antenna used to perform the DOA detection. To achieve a high-resolution DOA detection, a radiation pattern with a very narrow main radiation lobe has to be used to allow a precise scan of the azimuth plane and detect minor received signal amplitude variations over small rotation angles. Furthermore, this technique implies a mechanical rotation of the receiving antenna. This leads to a strong influence of mechanical tolerances on measurement results as well as scanning times that depend on the rotation speed of the antenna. An electronic beam steering antenna element is nowadays commonly used instead of the mechanical rotation (for instance with the help of digital beam-forming techniques [15, 23]). Nevertheless, the angular resolution reached by such systems is relatively low and implies complex beam steering techniques to allow a precise beam scan over the DOA range of interest.

Nevertheless, for certain applications with different geometrical arrangements further information can be gained if monitoring the amplitude of the signal received by the observer. For the already described misalignment de-

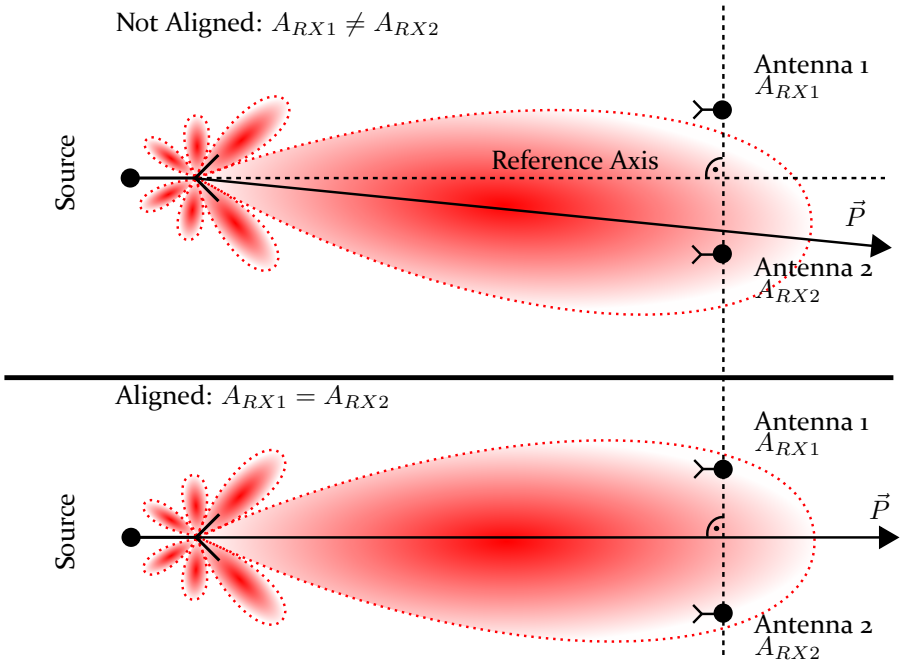

Figure 2.6: Antenna alignment technique based on an amplitude measurement. In far-field conditions as soon as the amplitude of the received signals at the two observer antennas is equal, the alignment in respect to the reference axis is met.

tection scenario, by making use of two receiving antennas with two received signals

$$\underline{S}_{RX1} = A_{RX1}\, e^{j\phi_{RX1}}, \tag{2.20}$$

$$\underline{S}_{RX2} = A_{RX2}\, e^{j\phi_{RX2}}, \tag{2.21}$$

it is possible to detect the proper alignment of the transmitting source. The exact misalignment angle cannot be determined, but the correct alignment of the Poynting vector to a reference axis (zero misalignment angle condition) can be detected.

Two receiving antennas are therefore aligned orthogonally to the reference axis. The alignment with respect to the reference axis can be met if the following condition is satisfied:

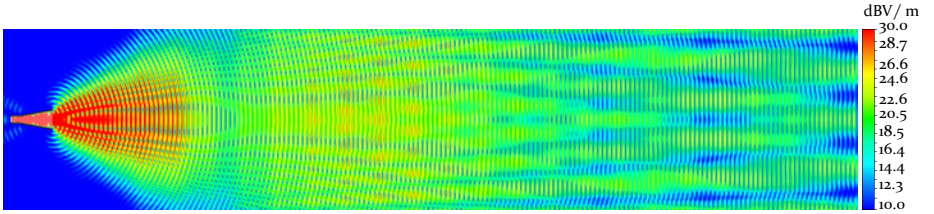

Figure 2.7: Absolute value of the electric field amplitude of the electromagnetic wave irradiated from a horn antenna (15 dBi). Destructive and constructive superposition of the propagating wave can be observed.

$$A_{RX1} = A_{RX2}. \tag{2.22}$$

This requires that the main radiation lobe of the transmitting antenna features a perfect symmetry of the signal amplitude distribution with respect to the wave propagation vector (Poynting vector). A correct alignment of the transmitter is therefore strongly dependent on the shape of the radiation pattern.

Furthermore, when monitoring the amplitude of the received signals on the two receiving antennas by the observer, the amplitude variations in the near-field, within the main radiation lobe lead to false interpretations.

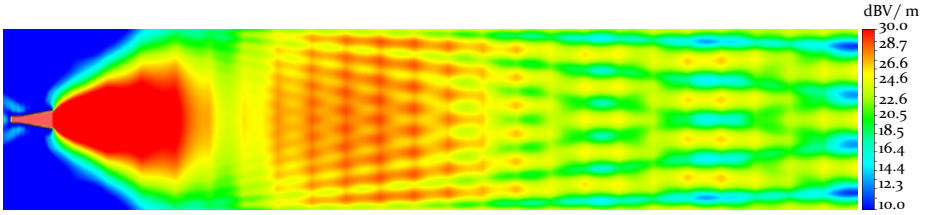

Figure 2.8: Average of the electric field amplitude over time. Local maximas and minimas of the electric field amplitude can be seen.

Due to the beam forming and focusing of the radiated signal the amplitude distribution directly in front of the transmitting antenna is deformed. This can be observed in Fig. 2.7 where a simulation of an electromagnetic wave irradiated from a horn antenna with 15 dBi gain is shown[8]. The antenna emits a signal at 5 GHz within a vacuum volume. A length of 5 m is used

[8] The simulation depicts a scenario for illustrative purposes only.

for the wave propagation[9]. In Fig. 2.7 the absolute value of the electric field amplitude at a phase of 0 RAD is depicted. Destructive and constructive superpositions can be observed. The wavefronts can be recognized as lines along which maxima of the electric field amplitude (as absolute values) are present. However, if evaluating the amplitude A_{RX} of a received complex signal the average of the electric field amplitude over time has to be taken into account (as depicted in Fig. 2.8). The wavefronts cannot be recognized anymore and the local maxima and minima of the electric field amplitude due to constructive and destructive superposition can be noticed.

An even distribution of the amplitude values cannot be found within the main radiation lobe. The amplitude distribution around the Poynting vector within the non-radiative near-field and Fresnel regions is not regular. Local constructive and destructive field superpositions create amplitude maxima and minima around the axis defined by the Poynting vector.

This irregular amplitude distribution is typical for the two mentioned near-field regions. Nevertheless, even in the beginning of the far-field certain amplitude irregularities can be often observed since the boundary between the different regions is only vaguely defined by eq. (2.16) and (2.17). In other words, the amplitude distribution with respect to the axis defined by the Poynting vector does not feature a monotone decay with an increasing distance from the mentioned axis. Therefore, the unknown amplitude pattern does not necessarily allow a correct evaluation of the beam direction if the condition expressed in eq. (2.22) is met.

On the other hand, a correct misalignment detection of the propagating wave can be performed by monitoring the phase of the received signals by the observer. This technique will be introduced in the next section.

2.4 Phase Measurement Based Direction Finding

As introduced before in this chapter, for DOA detection purposes it is possible to monitor one or more complex received signals as described in eq. (2.19). Up to now A_{RX} has been used to get the DOA information. However, also the phase ϕ_{RX} of the received complex signal $\underline{S}_{RX}$ can be used to determine the propagation direction of the electromagnetic wave.

The phase ϕ_{RX} is a periodic value hereby expressed in radians, of a quantity

[9] Boundary conditions for the time domain full-wave solver used where defined as open (continuous propagation in free space with no obstacles).

that is defined between $-\pi$ and $+\pi$. Without an absolute phase reference it is not possible to correctly define ϕ_{RX}. Theoretically, ϕ_{RX} is referred as the phase of the received complex signal from the observer as:

$$\phi_{RX} = M(\phi - \phi_{TX}), \tag{2.23}$$

with $\phi \in [-\pi, +\pi]$, $M \in \mathbb{Z}$ and ϕ_{TX} the phase of the transmitted signal at the source. ϕ_{RX} is therefore defined as an integer multiple of a value between $-\pi$ and $+\pi$ with respect to the phase of the signal emitted by the source. However, for DOA and misalignment detection applications, the reference phase ϕ_{TX} of the signal origin is unknown. Therefore, another phase definition has to be used. For this reason, a relative phase difference will be addressed between two or more receiving antennas that are not related to the transmitting source. From now on, unless otherwise specified, two receiving antennas will be considered at the observer.

A relative phase difference $\Delta\phi$ can be therefore defined as:

$$\Delta\phi = \phi_{RX2} - \phi_{RX1}, \tag{2.24}$$

where ϕ_{RX1} and ϕ_{RX2} are the phase values of the two complex received signals $\underline{S}_{RX1}$ and $\underline{S}_{RX2}$ already defined in section 2.3 by eq. (2.20) and eq. (2.21).

The observer can evaluate these two signals received by two antennas that are aligned on a reference geometrical axis (antenna axis). The arrangement is depicted in Fig. 2.9. The source (which is purposely not shown within the represented cut-out plane) radiates the electromagnetic wave with a certain radiation pattern. Part of the main radiation lobe is depicted in the picture, where the electric field vector component $\vec{E}_z$ is shown. Two antennas are placed in this scenario, receiving the two complex signals $\underline{S}_{RX1}$ and $\underline{S}_{RX2}$. The phase fronts are highlighted in the picture as well.

To better represent the arrangement referenced to the phase fronts of the propagating wave when the direction of propagation is changing, further graphical representations are hereby presented in Fig. 2.10 and in Fig. 2.11. In the first one, the Poynting vector is orthogonal to the antenna axis, leading therefore to

$$\phi_{RX1} = \phi_{RX2} \Rightarrow \Delta\phi = 0. \tag{2.25}$$

When this condition is met the wave propagates with a direction exactly

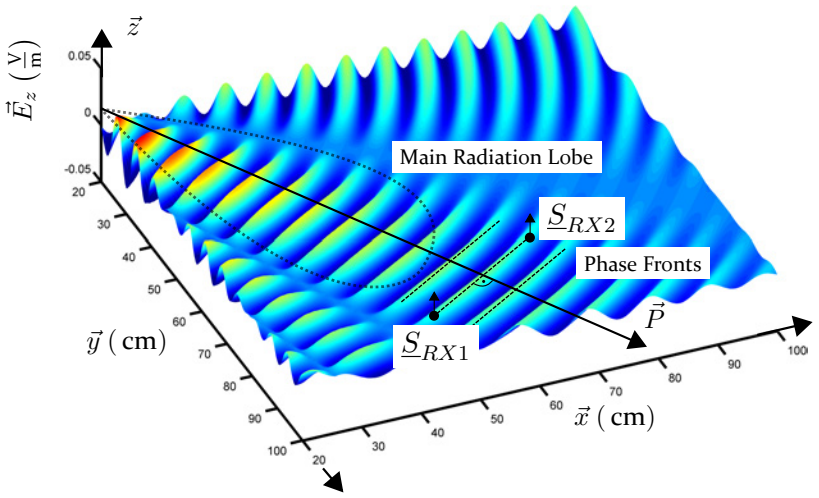

Figure 2.9: $\vec{E}_z$ of an electromagnetic wave propagating from a source into the far-field. The phase fronts within the main radiation lobe are orthogonal to the Poynting Vector $\vec{P}$. The two complex signals $\underline{S}_{RX1}$ and $\underline{S}_{RX2}$ are received from two antennas by the observer.

orthogonal to the antenna axis. On the other hand, as soon as $\phi_{RX1} \neq \phi_{RX2}$, thus $\Delta\phi \neq 0$ the direction of propagation is not orthogonal to the antenna axis anymore. This situation can be observed in Fig. 2.11.

For a simple "zero alignment" application, only the condition expressed in eq. (2.25) has to be met and this can be easily implemented with appropriate receivers comparing the phase of the two signals $\underline{S}_{RX1}$ and $\underline{S}_{RX2}$. When both signals are in-phase, the alignment is correct. For this purpose, no further information is necessary, not even the wavelength of the detected signal.

This is similar to the technique discussed in section 2.3 with eq. (2.22). The main difference is, that the phase information is way more exact to identify the Poynting vector than the amplitude information. If the TEM properties are satisfied, the phase fronts are orthogonal to the Poynting vector and feature a much more regular distribution around the radiating antenna (as can be seen in Fig. 2.12, if compared to the amplitude variations, as shown in Fig. 2.8). On the other hand, it is also possible to exactly detect a DOA angle that is not orthogonal to the antenna axis. This will be discussed further on in section 2.4.3.

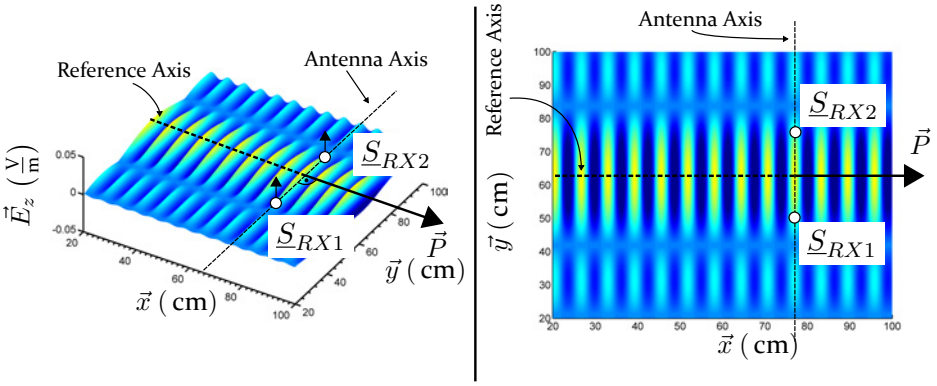

Figure 2.10: Geometrical arrangement of the two receiving antennas with the reference axis and the propagating wave. In this case, the Poynting vector is orthogonal to the antenna axis, therefore, $\phi_{RX1} = \phi_{RX2}$, so that $\Delta\phi = 0$.

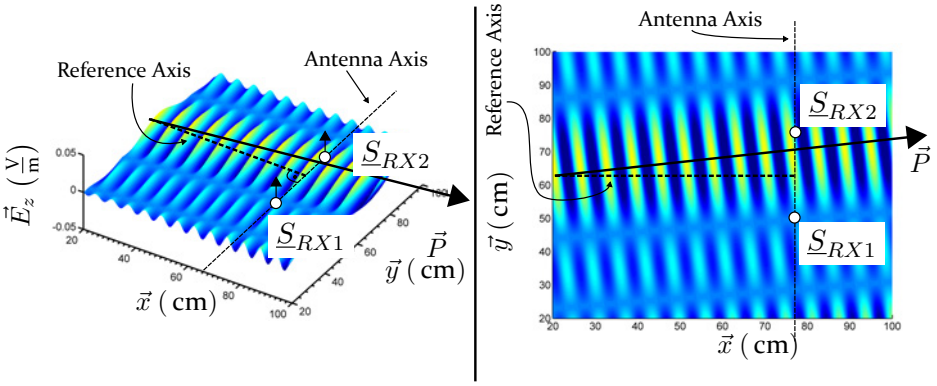

Figure 2.11: In this case, the wave features a propagation direction (Poynting vector $\vec{P}$) that is not orthogonal to the antenna axis. Therefore, $\phi_{RX1} \neq \phi_{RX2}$, and $\Delta\phi \neq 0$.

Figure 2.12: Phase of the electric field of the propagating wave radiated from the antenna. The phase fronts can be clearly identified as a regular pattern that helps to detect the direction of propagation.

2.4.1 The Phase Center

The phase center is the origin of the spherical wavefronts of the electromagnetic wave emitted by a radiating antenna (Fig. 2.13) [14]. The phase fronts are subject to a great change over the full solid angle depending on which antenna is radiating the wave. The phase center is usually obtained by rotating the antenna about a geometrical axis and determining, for a certain solid angle of interest, the position where a measured phase variation is neglectable over the desired solid angle [15]. This experimental method is demanding in terms of time and equipment, especially because the phase center changes for different radiation pattern directions. Alternatively the phase center can be numerically obtained by full-wave simulations. In the next paragraph the role of the phase center for antenna misalignment detection and the relation between the phase center position and the measured phase difference will be explained.

2.4.2 The Role of the Phase Center for Antenna Misalignment Detection

It has to be underlined, that for a directional antenna (as the one hereby taken in consideration for misalignment detection purposes) within the main lobe, even as close to the source as in the Fresnel region, the wave approximates a plane wave with straight phase fronts, thus satisfying the TEM propagation properties already mentioned. This is due to the phase center shift for directional antennas.

For an isotropic radiator, the phase center is exactly at the same position as the geometrical center of the antenna (that is its rotational pivot, or the feed of the antenna). In this case, the radiator features no directivity. Obviously

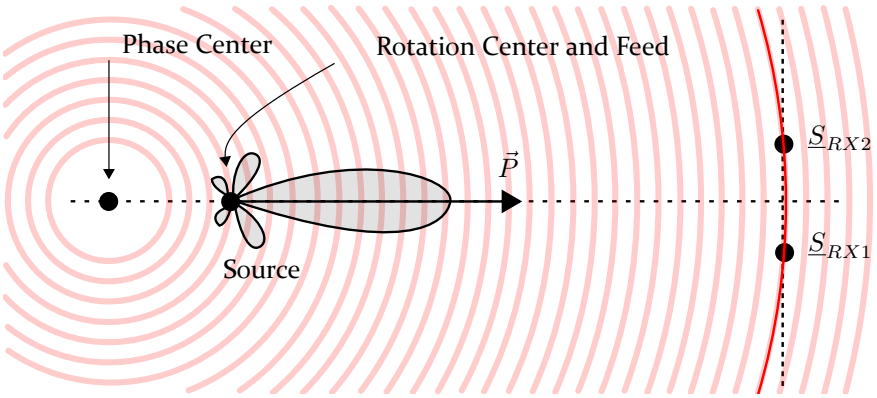

Figure 2.13: Schematic representation of the phase center, referred to the main radiation lobe of a focused source. The position of the phase center does not coincide with the rotation center and feed of the directional radiator. In this case the transmitting antenna is aligned on an axis orthogonal to the receiving antennas, therefore, the detected phase difference is $\Delta\phi = \phi_{RX2} - \phi_{RX1} = 0$.

a rotation around its geometrical center does not affect the orientation of the radiation pattern, since it is omnidirectional.

As soon as the antenna element increases the directivity in a certain direction in space, the phase center of the electromagnetic wave moves away from the geometrical center (feed) of the antenna in the direction opposite to the one in which the main radiation lobe develops (defined by the Poynting vector $\vec{P}$). The curvature of the phase fronts is related to the phase center and not to the feed of the antenna. When rotating the transmitting antenna around its feed the phase center is therefore also moved (as shown in Fig. 2.14). Thus a misalignment angle measurement for directional antennas is possible by measuring the orientation of the phase fronts with respect to a well known reference. This is possible because the rotation of the antenna around its feed causes also a rotation of the phase center.

2.4.3 DOA Angle and Misalignment Angle Measurement

As introduced up to now, both the DOA angle of a wave as well as the misalignment angle of a focused radiator with respect to a reference cause a phase difference at two receiving antennas by the observer, aligned on a reference axis. In case of a DOA orthogonal to the reference axis and in

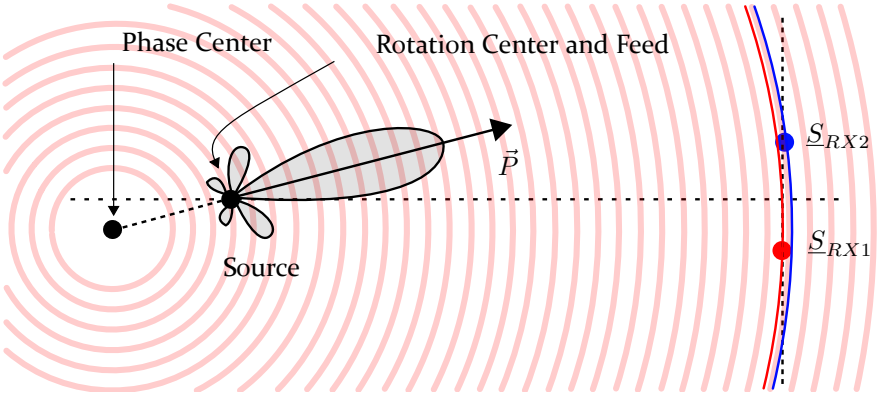

Figure 2.14: In this case the transmitting antenna is rotated around its feed and is not aligned to the reference axis anymore. This causes a movement of the phase center thus tilting the phase fronts within the main radiation lobe. The measured phase difference in this case is $\Delta\phi = \phi_{RX2} - \phi_{RX1} \neq 0$.

case of a zero misalignment angle, the phase difference at the two receiving antennas is zero. Nevertheless, not only a zero alignment or a precise orthogonal DOA can be detected by a phase measurement. The DOA and the misalignment angle can be exactly measured if some extra information is available [4].

For sake of clarity, a simplified geometrical setup is hereby introduced, as depicted in Fig. 2.15. The DOA measurement is addressed, nevertheless, the relationships introduced are valid for a misalignment angle detection as well. As can be understood from Fig. 2.15, the measured phase difference can be easily related to the actual DOA angle α by simple trigonometric rules [6]. Therefore, the DOA angle can be calculated from the phase difference $\Delta\phi$ through

$$\alpha = \sin^{-1}\left(\Delta\phi \, \frac{\lambda}{2\pi L}\right), \tag{2.26}$$

where λ is the wavelength of the signal and L is the distance between the two receiving antennas. L can be optimized for a specific measurement so that:

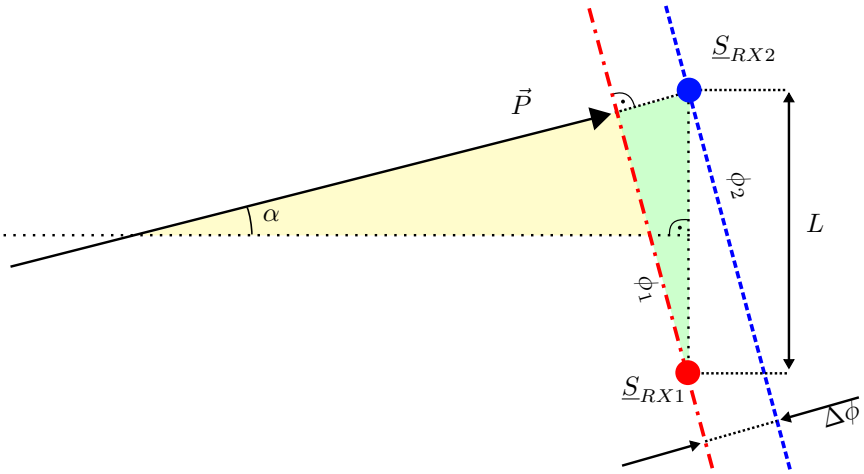

Figure 2.15: Simplified geometrical representation of a DOA or a misalignment angle detection by a phase measurement. The measured phase difference $\Delta\phi$ can be easily related to the actual DOA angle α by means of trigonometric rules.

$$L_{max} = \frac{\lambda\,\Delta\phi_{max}}{2\pi\,\sin\left(\alpha_{max}\right)}, \tag{2.27}$$

$$\alpha_{min} = \sin^{-1}\left(\frac{\lambda\,\Delta\phi_{min}}{2\pi\,L_{max}}\right). \tag{2.28}$$

$\Delta\phi_{min}$ is the minimum measurable phase difference (capability of the phase measurement system), α_{min} is the minimum angle that can be measured, $\Delta\phi_{max}$ is the maximum phase difference (not more than π RAD) and α_{max} is the maximum DOA angle that has to be measurable by the system.

It is now clear that by performing a phase difference measurement between two antennas aligned on a reference axis, the DOA angle or the misalignment angle can be calculated [6]. To measure a phase difference, the two complex signals $\underline{S}_{RX1}$ and $\underline{S}_{RX2}$ have to be acquired by an appropriate complex receiver. The phase information has to be consequently extracted from the complex signal quantities. There are several techniques to implement such a receiver. To introduce the reader to the different receiver characteristics an architecture overview is given in the next chapter.

3 Receiver Architecture Overview

The purpose of a receiver is generally to convert a received signal from the high-frequency carrier used for the transmission down to baseband in order to extract the information inherent in the signal itself. This frequency conversion is achieved through a so called mixing process performed by mixer components. There is a large variety of mixers for several different applications all featuring advantages as well as disadvantages. The purpose of this chapter is not to illustrate the pros and cons nor to perform a comparison between the different architectures and techniques, but to give the reader a brief overview that helps to understand the basic process of radio signal reception. There is an overwhelming amount of highly specialized literature on the topic of RF mixing and the interested reader is addressed to investigate classic graduate level textbooks of electronics [24] as well as professional detailed articles and transactions. Hereby, for sake of clarity, only a short and summarized overview will be given.

3.1 Multiplicative Mixing Technique

The multiplicative mixing technique is a nonlinear process that involves two signals to be multiplied to generate the complex output signal. If two signals with frequencies f_1 and f_2 are mixed together with a multiplicative mixer (Fig. 3.1**(a)**), the output presents frequencies that are the sum and difference of the two input frequencies $f_{sum} = f_1 + f_2$ and $f_{diff} = f_1 - f_2$. This can be explained by describing the input signals as [25]

$$I_1 = A_1 \sin(2\pi f_1 t), \tag{3.1}$$
$$I_2 = A_2 \sin(2\pi f_2 t), \tag{3.2}$$

and performing a multiplication to generate the output. By using standard

trigonometrical methods, it is possible to describe the output signal O as [25]:

$$O = \frac{1}{2} A_1 A_2 \left[\cos\left(2\pi\left(f_1 - f_2\right)t\right) - \cos\left(2\pi\left(f_1 + f_2\right)t\right)\right]. \tag{3.3}$$

The two terms $f_{sum} = f_1 + f_2$ and $f_{diff} = f_1 - f_2$ are therefore present. For a direct conversion receiver, the signal component of the output f_{sum} is usually not of interest, since it represents a signal at a very high frequency and is therefore usually filtered out. On the other hand, the component featuring the frequency f_{diff} is used for the conversion to baseband.

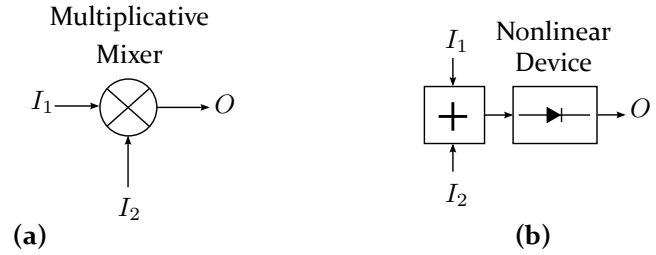

Figure 3.1: Ideal multiplicative **(a)** and additive **(b)** mixers.

3.2 Additive Mixing Technique

Besides multiplicative mixers, also additive mixers can be used to down-convert a signal to baseband (Fig. 3.1**(b)**). From a mathematical point of view a multiplication between two input signals I_1 and I_2 is necessary to obtain the frequency terms f_{sum} and f_{diff}. Nevertheless, this multiplication can be done indirectly. Additive mixing makes use of nonlinear devices to perform the down-conversion as multiplicative mixers do, though with a main difference: the necessary multiplication is performed due to the nonlinear characteristic of the mixing device. The two input signals are first added together (linear superposition) resulting in [25]:

$$I_{sum} = I_1 + I_2 = A_1 \sin\left(2\pi f_1 t\right) + A_2 \sin\left(2\pi f_2 t\right). \tag{3.4}$$

I_{sum} is now passed to the actual nonlinear device (a diode, for instance) that generates an output described by:

$$O = \sum_{k=1}^{\infty} p_k \cdot I_{sum}^k. \tag{3.5}$$

Eq. (3.5) comprises all terms of the nonlinear transformation with appropriate weighting coefficients p_k. It is therefore valid for all kinds of nonlinear devices and signal types. Nevertheless, only one component of the sum expressed in eq. (3.5) is essential for the frequency conversion process. The quadratic term ($k = 2$) is used and the others are suppressed by proper filtering.

For sake of clarity, it is hereby assumed that the nonlinear device is ideal featuring a purely quadratic characteristic ($p_2 = 1, p_k = 0$ for $k \neq 2$). Therefore, the quadratic term can be expressed by the relation:

$$O|_{k=2} = (I_1 + I_2)^2 = I_1^2 + 2I_1I_2 + I_2^2. \tag{3.6}$$

In eq. (3.6) three signal components I_1^2, I_2^2 and $2I_1I_2$ make up the term $O|_{k=2}$. These components can be written as:

$$\begin{aligned} I_1^2 &= A_1^2 \sin^2(2\pi f_1 t), & (3.7)\\ I_2^2 &= A_2^2 \sin^2(2\pi f_2 t), & (3.8)\\ 2\,I_1I_2 &= 2\,A_1 \sin(2\pi f_1 t)\;\; A_2 \sin(2\pi f_2 t). & (3.9) \end{aligned}$$

Due to trigonometric relationships for the square of sine functions, the components I_1^2 and I_2^2 present frequency components which are either zero or twice the frequencies f_1 and f_2 respectively (as described by eq. (3.3)). These components are filtered out thus leaving only $2I_1I_2$. Eq. (3.9) can be rewritten with the help of eq. (3.3) as:

$$2\,I_1I_2 = A_1A_2\;\left[\cos(2\pi(f_1 - f_2)\,t) - \cos(2\pi(f_1 + f_2)\,t)\right]. \tag{3.10}$$

The two components $f_{sum} = f_1 + f_2$ and $f_{diff} = f_1 - f_2$ are clearly visible in eq. (3.10). Nevertheless, by applying filtering to eliminate I_1^2 and I_2^2 as mentioned above (band-pass filtering, denoted by "BP") the component f_{sum} vanishes as well, leading to:

$$[O|_{k=2}]_{BP} = A_1A_2\;\cos(2\pi(f_1 - f_2)\,t). \tag{3.11}$$

Since the two input signals are added and then converted to baseband with the help of a nonlinear device (by using the quadratic term of the complete conversion) this mixing process is called additive in contrast to the multiplicative technique mentioned in section 3.1, where the two signals are in fact multiplied.

Obviously, for real-world passive nonlinear components the weighting factors are always smaller than one ($p_k < 1$). Eq. (3.11) is only valid for purely quadratic devices with an ideal quadratic transfer function ($y = x^2$, where x is the input and y the output of the transfer function). This explains why the output signal $[O|_{k=2}]_{BP}$ expressed in eq. (3.11) features an amplitude larger than the one resulting from the multiplication of the two signal amplitudes A_1 and A_2 as expressed in eq. (3.3). In fact, for non-ideal devices eq. (3.11) should be rewritten as:

$$[O|_{k=2}]_{BP} = p_2 \; A_1 A_2 \; \cos\left(2\pi \left(f_1 - f_2\right) t\right), \tag{3.12}$$

where the weighting coefficient p_2 appropriately scales the signal amplitude of the quadratic term. Only for active devices the condition $p_2 \geq 1$ can be satisfied.

3.3 Homodyne Receiver

Beside the main categorization of mixing techniques used by different receiver types, an important definition of receiver architectures is hereby summarized. Principally, receivers can be sorted into two different groups: homodyne receivers and heterodyne receivers. Several different names are used to define these two categories often identifying subgroups within these two main definitions. In specialized literature receivers are often referred to as direct-conversion, synchrodyne, "zero-IF", "low-IF", superheterodyne or neutrodyne receivers. However, these definitions are merely sinonyms referring to the two main categories introduced in the following.

A homodyne receiver down-converts an incoming signal to baseband by using a Local Oscillator (LO) reference source with a frequency identical to the carrier frequency of the incoming signal. This method is in contrast to the heterodyne receiver technology where an initial conversion to an Intermediate Frequency (IF) takes place. The result of the homodyne mixing process is a demodulated output directly in baseband. In other words, the conversion to baseband is done in a single step [26].

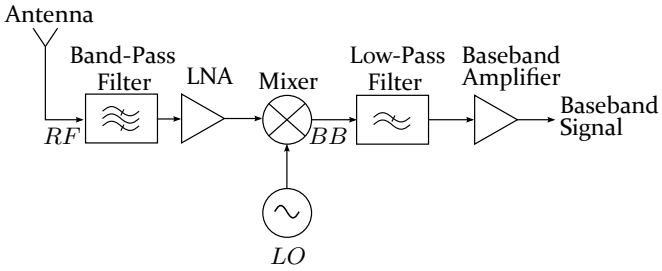

Figure 3.2: Schematic of a homodyne receiver. The LO frequency equals the carrier frequency of the RF signal. Therefore, the frequency conversion through the one-stage mixing with the LO demodulates the RF signal directly to baseband.

In this way the complexity of the receiver is reduced, as opposed to the complex circuit design of heterodyne receivers with at least two frequency conversions and intermediate frequency stages as well as image rejection issues.

Nevertheless, this technique presents disadvantages as well. For instance, the synchronization between the incoming signal carrier and the LO used for the direct conversion can be quite challenging. This problem is solved with Phase-Locked-Loop (PLL) circuits synchronizing the LO to the carrier signal. For example, direct reception of signals with amplitude or frequency modulation schemes requires the LO to be synchronized with a PLL to the carrier frequency.

Another issue of the homodyne receivers is, that the amplitude of the signal in baseband depends directly on the amplitude of the received signal. Since the amplitude of the received signal can change abruptly depending on the reception quality, also the output level at baseband varies over a very wide dynamic range. This is one technical challenge which limits the practicability of the design.

However, when using quadrature detection [27] in a homodyne receiver concept (for instance, by using diode-based additive mixers featuring a quadratic transfer function) and by implementing some compensation strategies in digital signal processing some of the mentioned problems can be solved. This is commonly done in modern software defined radio techniques.

A major problem that affects homodyne receivers is that due to signal leakage in the receiver, the LO signal can pass through the mixer stage into the input signal path and get self-mixed into baseband, as if it was a component of the received signal. This creates a DC offset signal in baseband that re-

duces the overall dynamic range of the receiver. Therefore, a high isolation between the two signals that are involved in the down-mixing process has to be guaranteed in order to achieve a high dynamic range. This issue will be addressed in chapter 8 describing ranging techniques using the proposed Six-Port receiver.

In the past, the above mentioned issues inherent in the homodyne receivers made this technique impractical, thus slowing down further development in favor of the alternative heterodyne technique [28]. Nevertheless, in the last years homodyne receivers gained relevance and find place in many applications, from software defined radios to microwave interferometry. In the latter one, for instance, the reference signal generated by the LO is used as a common source also for the signal that is used for the interference process, thus avoiding the PLL circuitry. Direct-conversion receivers are now incorporated in many receiver applications, from consumer products to special applications making use of high data rate transceivers [1].

3.4 Heterodyne Receiver

While in homodyne detection the LO has the same frequency as the received signal, in heterodyne detection the LO is frequency-shifted [29]. In this way, new frequencies other than baseband are created by mixing these two input signals.

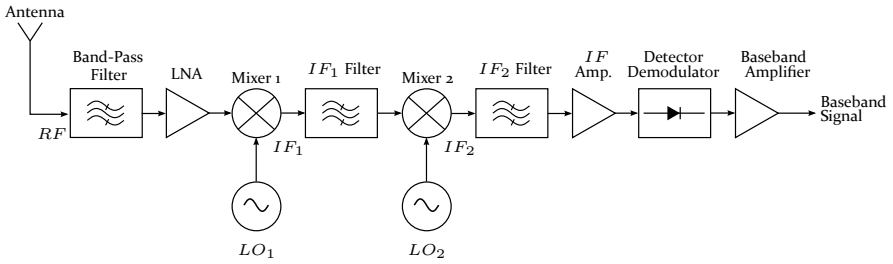

Figure 3.3: Schematic of a double-stage superheterodyne receiver. In this case, the RF signal is converted to a lower IF through two mixing stages and finally, from the lower IF_2 to baseband through a demodulator (nonlinear device).

The heterodyne receiver, invented by R. Fessenden in 1901 [30], shifts the carrier signal into a new frequency range, called Intermediate Frequency by combining it with the LO in a nonlinear mixing device. The IF signal

is amplified and filtered before it is sent to an envelope detector [25]. The most widespread type is the superheterodyne receiver, invented by E. H. Armstrong in 1918 [31]. Historically it has been called superheterodyne referring to the "super-sonic" frequency range of the IF (above human hearing frequency range).

The advantage of this technique is that the received carrier signal is converted to IF before tuning. Thus, the complicated RF amplifier and bandpass filter stages (which in homodyne receivers have to be tunable to receive different incoming signal frequencies) can be built to work at one fixed frequency. This simplifies their design [32] since tunable filters and amplifiers in the RF range are more difficult to design than in the IF band, mainly because the IF is at a considerably lower frequency than the RF of the incoming signal.

4 The Six-Port Receiver

A special type of homodyne receiver based on the additive mixing technique is the Six-Port receiver. This circuit has been introduced in the 1960s by G. Engen and C. Hoer for power measurement applications. Engen and Hoer where working in the area of microwave measurements focusing on reflectometer techniques [33–36] and inter-comparison of different microwave power meters [37]. Later work at the beginning of the 70s [38] evolved in what today is known as the Six-Port receiver [39]. Through further research in calibration techniques for the newly introduced system [40], Engen finally developed in 1977 the Six-Port receiver as an alternative network analyzer [41], leading further on to an efficient implementation of the Six-Port [42].

Nevertheless, Engen still addressed the test and measurement scenario as an application for the Six-Port [43,44] developing though further knowledge in this field and introducing for the first time the "Dual Six-Port" concept[1] [45]. As will be shown later on, Six-Port receivers use only scalar measurements from four power detectors to extract both magnitude and phase information. Thus, they can be used to implement a vector network analyzer. To build a Six-Port based two-port network analyzer, two Six-Port receivers are needed (thus, a total of eight power detectors). Such vector network analyzers are very accurate and usually employed in standards laboratories, such as the National Institute of Standards and Technology (NIST) [8].

The Six-Port network is nowadays known as an alternative receiver setup for microwave and millimeter-wave frequencies [46,47]. Independent from the design, a Six-Port receiver is a passive structure featuring two input ports and four output ports [48]. As the Six-Port receiver is based on the interferometric principle, the two input signals are superimposed with each other

[1] The dual Six-Port introduced by Engen was aiming at vector network analysis applications and has not to be mistaken with the dual Six-Port concept introduced by the author of this work (further on described in chapter 6).

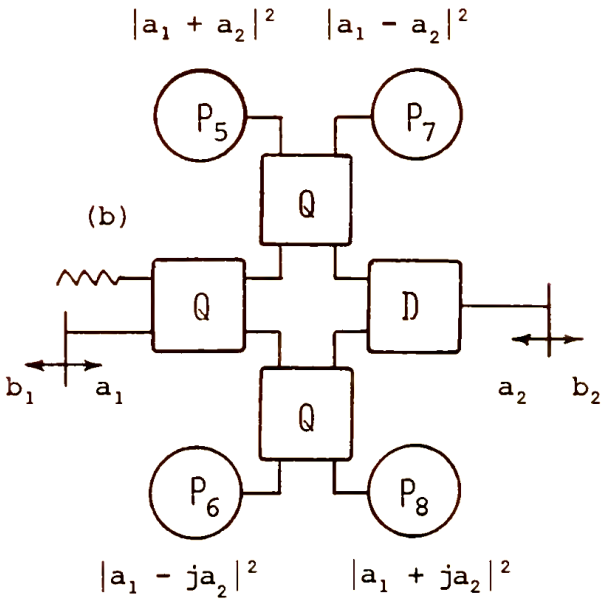

Figure 4.1: First schematical drawing made by Hoer in his publication in 1975 illustrating the Six-Port receiver [33].

under four different relative phase shifts. Depending on phase difference and amplitudes of the two input signals, constructive and destructive interaction takes place at the four output ports.

4.1 Theory of the Six-Port Receiver

Two complex input signals $\underline{P_1}$ and $\underline{P_2}$ with carrier frequency f can be defined as:

$$\underline{P_1} = A_1\, e^{j(2\pi f t+\phi_1)} = A_1\,[\cos(\omega t+\phi_1)+j\,\sin(\omega t+\phi_1)]\,, \quad (4.1)$$

$$\underline{P_2} = A_2\, e^{j(2\pi f t+\phi_2)} = A_2\,[\cos(\omega t+\phi_2)+j\,\sin(\omega t+\phi_2)]\,, \quad (4.2)$$

with the radial frequency $\omega = 2\pi f$, the amplitude values A_1 and A_2, the phase values ϕ_1 and ϕ_2. Considering the relative quadrature phase differences between $\underline{P_1}$ and $\underline{P_2}$ of 0, $\pi/2$, π and $3\pi/2$ RAD at the output ports,

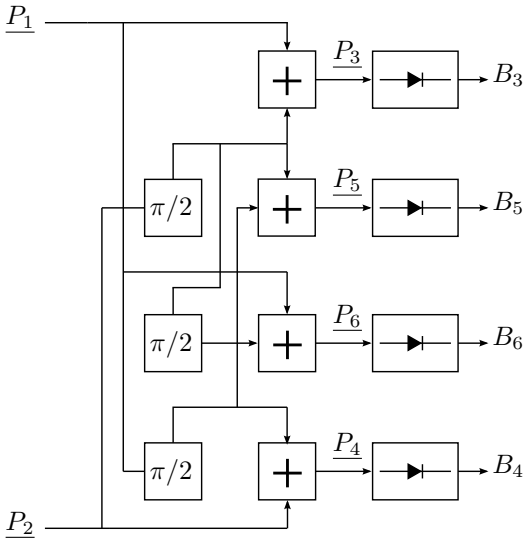

Figure 4.2: Six-Port receiver architecture.

the complex output signals $\underline{P_3}$, $\underline{P_4}$, $\underline{P_5}$ and $\underline{P_6}$ can be calculated as [33, 47]:

$$\underline{P_3} = 0.5\left(\underline{P_1} + j\underline{P_2}\right), \tag{4.3}$$
$$\underline{P_4} = 0.5\left(j\underline{P_1} + \underline{P_2}\right), \tag{4.4}$$
$$\underline{P_5} = 0.5\left(j\underline{P_1} + j\underline{P_2}\right), \tag{4.5}$$
$$\underline{P_6} = 0.5\left(\underline{P_1} - \underline{P_2}\right). \tag{4.6}$$

Down-conversion to baseband by power detectors delivers the following baseband voltages B_3 to B_6 [33, 47]:

$$B_3 = \left|\underline{P_3}\right|^2 = 0.25\left|\underline{P_1} + j\underline{P_2}\right|^2, \tag{4.7}$$
$$B_4 = \left|\underline{P_4}\right|^2 = 0.25\left|j\underline{P_1} + \underline{P_2}\right|^2, \tag{4.8}$$
$$B_5 = \left|\underline{P_5}\right|^2 = 0.25\left|j\underline{P_1} + j\underline{P_2}\right|^2, \tag{4.9}$$
$$B_6 = \left|\underline{P_6}\right|^2 = 0.25\left|\underline{P_1} - \underline{P_2}\right|^2. \tag{4.10}$$

Due to the fact that the relative phase shifts between the four output ports are multiples of $\pi/2$ RAD, there is a complex representation $\underline{Z}$ for the baseband signals. The in-phase component I as well as the quadrature component Q can be split up in two pairs with a relative phase shift of π RAD in

between. As a result, the baseband signals B_3, B_4, B_5, B_6 can be handled like differential I/Q-signals [33, 47].

$$I = \Re\{\underline{Z}\} = (B_5 - B_6), \tag{4.11}$$
$$Q = \Im\{\underline{Z}\} = (B_3 - B_4), \tag{4.12}$$
$$\underline{Z} = I + jQ = (B_5 - B_6) + j(B_3 - B_4). \tag{4.13}$$

Calculating the argument of the complex expression $\underline{Z}$ leads to [33, 47]:

$$\arg\{\underline{Z}\} = \tan^{-1}\left(\frac{\Im\{\underline{Z}\}}{\Re\{\underline{Z}\}}\right) = \tan^{-1}\left(\frac{B_3 - B_4}{B_5 - B_6}\right). \tag{4.14}$$

Because of the nature of the arc tangent function (defined only between $-\pi/2$ and $\pi/2$) a careful definition of eq. (4.14) has to be given depending on the sign of $\Re\{\underline{Z}\}$ and $\Im\{\underline{Z}\}$. The conditions hereby stated have to be taken into account when calculating the argument of $\underline{Z}$:

$$\arg\{\underline{Z}\} = \begin{cases} \tan^{-1}\left(\frac{Q}{I}\right) & \text{for } I > 0, \\ \tan^{-1}\left(\frac{Q}{I}\right) + \pi & \text{for } I < 0, Q \geq 0, \\ \tan^{-1}\left(\frac{Q}{I}\right) - \pi & \text{for } I < 0, Q < 0, \\ +\pi/2 & \text{for } I = 0, Q > 0, \\ -\pi/2 & \text{for } I = 0, Q < 0, \\ 0 & \text{for } I = 0, Q = 0. \end{cases} \tag{4.15}$$

The circumstances expressed in eq. (4.15) are essential to correctly evaluate the expressions that follow. In some mathematical software environments the above stated conditions are summarized under a function named "atan2". From eq. (4.15) it is therefore evident, that $\arg\{\underline{Z}\}$ is affected by an ambiguity inherent in the definition of the arc tangent. Multiple values of the function are defined upon one input combination. Q/I can be positive if both Q and I are positive but also if both are negative, as well as Q/I can be negative for Q or I being negative as well. This ambiguity can be solved only if monitoring I and Q separately.

Through complex calculus it is possible to insert eq. (4.1) and (4.2) in (4.7)

to (4.10) resulting in [33, 47]:

$$B_3 = 0.25\left[A_1^2 + A_2^2 + 2A_1A_2\ \sin(\phi_2 - \phi_1)\right], \tag{4.16}$$
$$B_4 = 0.25\left[A_1^2 + A_2^2 - 2A_1A_2\ \sin(\phi_2 - \phi_1)\right], \tag{4.17}$$
$$B_5 = 0.25\left[A_1^2 + A_2^2 + 2A_1A_2\ \cos(\phi_2 - \phi_1)\right], \tag{4.18}$$
$$B_6 = 0.25\left[A_1^2 + A_2^2 - 2A_1A_2\ \cos(\phi_2 - \phi_1)\right], \tag{4.19}$$
$$\tag{4.20}$$

and calculate $\underline{Z}$ described by A_1, A_2, ϕ_1 and ϕ_2 with eq. (4.13) as:

$$\underline{Z} = A_1A_2\cos(\phi_2 - \phi_1) + jA_1A_2\sin(\phi_2 - \phi_1). \tag{4.21}$$

When calculating $\arg\{\underline{Z}\}$ it can be shown that[2]:

$$\arg\{\underline{Z}\} = \tan^{-1}\left[\frac{A_1A_2\ \sin(\phi_2 - \phi_1)}{A_1A_2\ \cos(\phi_2 - \phi_1)}\right] = \phi_1 - \phi_2 = \Delta\phi. \tag{4.22}$$

$\Delta\phi$ is equal to the phase shift between the two input signals.

If $\underline{P_1}$ is defined as a received signal from an antenna and $\underline{P_2}$ as a reference signal from an LO, with eq. (4.22) the phase of the received signal can be detected. Since the output signals B_3 to B_6 are in baseband, the Six-Port is a homodyne receiver. The additive superposition of the received signal $\underline{P_1}$ with the reference signal $\underline{P_2}$ is performed directly in RF. A phase detection is particularly accurate, since the two signals in RF are forced to additively interfere with each other at the high frequency of the carrier. Minor phase variations will result in changes of the amplitudes of the four baseband signals B_3 to B_6 due to the mentioned additive superpositions.

Furthermore, by creating four interferences of the two input signals with quadrature phase shifts between each other, two differential signal pairs in baseband are created. This makes the Six-Port receiver more robust against non-idealities due to the benefit of a differential signal representation.

The relationship between the baseband signals B_3 to B_6 as well as of I and Q with the phase shift $\Delta\phi$ between the two input signals $\underline{P_1}$ and $\underline{P_2}$ is represented in Fig. 4.3. A sample time scale from 0 to 20 s is hereby represented and it has been chosen for representative purposes only. From this plot, it can be noticed that the B_3 and B_4 as well as B_5 and B_6 are differential pairs.

[2] The complete derivation can be found in [47], at page 50.

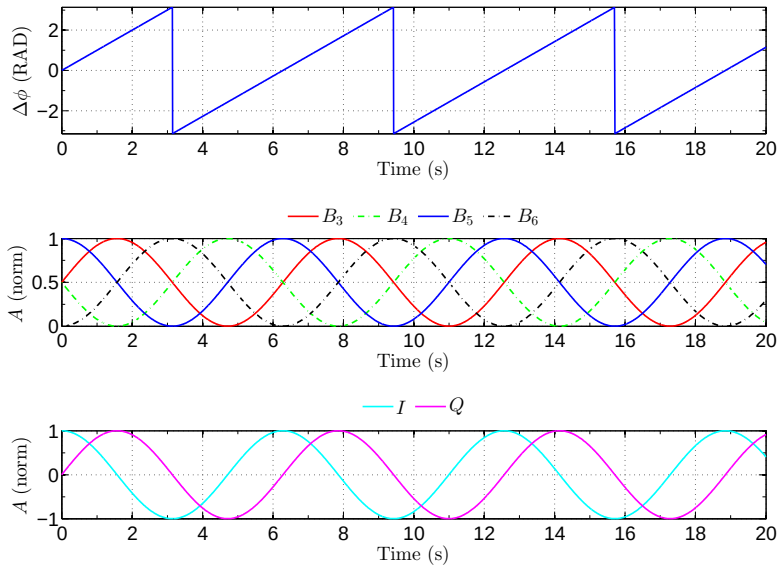

Figure 4.3: Relationship of the baseband output signals B_3 to B_6 and of I and Q with the phase shift $\Delta\phi$ between the input signals.

4.2 The Six-Port Receiver Implementation

Typically, the additive superposition necessary for the Six-Port receiver (Fig. 4.2) is done by combining the signals through coupler structures, while the phase shifts can be easily implemented by delay lines or special couplers. As nonlinear devices for the down-conversion, diode-based power detectors are used, nevertheless, several different nonlinear components have been used so far, showing advantages and disadvantages depending on the application for which the receiver has been used for [49].

There are several ways to combine in hardware the input signals in order to achieve the functionality of the Six-Port network illustrated in Fig. 4.2. Dealing typically with microwave frequencies of the input signals, several technologies can be chosen nowadays to implement the receiver in hardware. Classical waveguide structures feature high-performance and low-loss and can deal with high-power signals. Nevertheless, the cost of the components and mechanical complexity as well as tolerance sensibility and low repeatability are an issue of this technique.

At the beginning of microwave technology back in the Second World War, waveguides where the only feasible transmission lines that could be used to create circuits and systems at frequencies in the GHz range. This technology dominated the world of microwaves throughout the 60s, 70s and 80s, as no valid alternative technique could be successfully implemented with existing manufacturing processes. This is the main reason that stopped the diffusion on a large scale of the Six-Port receiver for decades, as a discrete waveguide implementation of such a receiver is quite expensive, bulky and fragile. Furthermore, the digital signal processing hardware needed to calibrate the Six-Port front-end was not available or very expensive. Thus, the Six-Port receiver introduced in the 1970s was limited as a test and measurement equipment in microwave laboratories for power measurement applications [41].

As Printed Circuit Boards (PCB) started to spread, better and better etching techniques as well as more performant planar substrate materials where developed, allowing the implementation of planar circuitry in always higher frequency ranges. The outstanding performance of waveguide transmission lines has never been reached, but several applications started to benefit from the planar, compact form factor of this new technique.

Due to the recent progress in material technology and manufacturing processes the Six-Port receiver can be successfully implemented nowadays in planar microstrip circuits to efficiently operate at higher microwave frequencies. Furthermore, planar microstrip circuits are suitable for low-cost mass production, enabling the implementation of microwave circuitry. The reader is addressed to reference textbooks "Microstrip Lines and Slot-lines" R. Garg, P. Bhartia, K. C. Gupta [50] and "Foundations of Interconnect and Microstrip Design" from T. C. Edwards and M. B. Steer [51] for detailed information about microstrip technology and transmission line theory.

4.2.1 Planar Microstrip Technology

There are several planar transmission line structures. The most common transmission lines are microstrip, coplanar waveguide, slot-line, and coplanar strips. Though,the microstrip line is the most popular of these transmission structures, with several variations such as the inverted microstrip, suspended microstrip, microstrip with overlay, strip dielectric waveguide, and inverted strip dielectric waveguide [50]. The popularity of this transmission line is primarily because it can be fabricated by photolithographic process and also the fact that the mode of propagation in a microstrip is

quasi TEM [11]. This allows an easy approximate analysis as well as wide band circuits to be implemented [51].

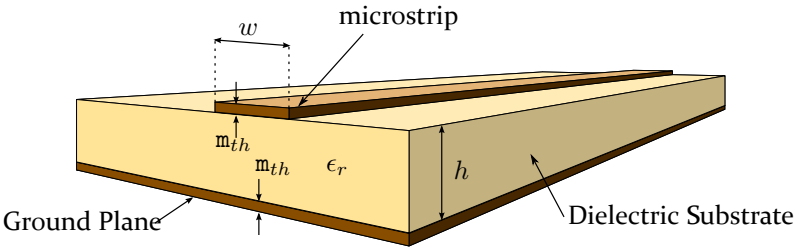

Figure 4.4: Geometry of a microstrip transmission line.

A microstrip structure is a two-conductor single-ended transmission line. The configuration is obtained by inserting a dielectric slab with thickness h between two conductors, one being a large reference ground plane and the other a metallic strip with a smaller width w as the ground plane. The described structure can be observed in Fig. 4.4. Microstrip lines differ considerably from other transmission lines. For instance, the microstrip structure is open at the top. The structure is therefore asymmetrical [50]. As a consequence, the dielectric medium of the transmission line is inhomogeneous, consisting of the dielectric plate and the air volume above the conductor strip. This open configuration makes a microstrip very convenient for use in RF PCBs where discrete lumped devices must be mounted on the circuit. Furthermore, small adjustments or tuning can be performed after fabrication. However, the open structure of a microstrip causes some complications in microstrip analysis and design [11]. This is due to the presence of the dielectric-air interface. An equivalent dielectric constant ϵ_{req} can be therefore calculated for a microstrip line according to [11]:

$$\epsilon_{req} = \frac{\epsilon_r + 1}{2} + \frac{\epsilon_r - 1}{2} \frac{1}{\sqrt{1 + 12h/w}}. \tag{4.23}$$

This value can be used to calculate the line impedance Z_0 for a desired signal frequency together with the geometrical parameters as follows [11]:

$$Z_0 = \begin{cases} \frac{60}{\sqrt{\epsilon_{req}}} \ln\left(\frac{8h}{w} + \frac{w}{4h}\right) & \text{for } w/h \leq 1, \\ \frac{120\pi}{\sqrt{\epsilon_{req}}[w/h + 1.393 + 0.667 \ln(w/h + 1.444])} & \text{for } w/h \geq 1. \end{cases} \tag{4.24}$$

Furthermore, the length of the transmission line can be used to perform

phase shifts on a signal with a frequency f. The relationship between the length L of the transmission line and the phase shift ϕ is expressed by

$$L \approx \frac{c}{2\pi f \sqrt{\epsilon_{req}}} \cdot \phi \frac{\pi}{180 \text{ DEG}}. \tag{4.25}$$

With the help of eq. (4.23), (4.24) and (4.25) it is possible to design microstrip circuit components with distributed elements properties. The metal thickness m_{th} can be ignored for a first approximate evaluation of microstrips. However, for a detailed analysis, the metallization thickness has a non-neglectable influence on the line impedance for higher frequencies, when m_{th} is compared to the wavelength.

The so called "side-wall" effect [50] influences the equivalent width of the microstrip conductor due to fringing fields that further couple the vertical metal walls of the strip to the ground-plane through the substrate. Therefore, this decreases the line impedance. This is one of the non-ideal effects that take place in a real-world microstrip line. These effects cannot be neglected at higher microwave frequencies and need particularly accurate, material dependent nonlinear analytical models to be described correctly [52]. However, such complex analytical equation systems soon reach limitations in the description of the model behavior. That is why numerical methods are nowadays commonly used to correctly estimate the parameters of a microstrip at higher frequencies [53].

In the following, different circuit components will be discussed, aiming at implementing the complete Six-Port receiver in microstrip technology. Several different circuit topologies have been developed to implement a Six-Port receiver. In this work, a well known circuit architecture will be presented, similar to the one introduced in [47, 54].

As mentioned before, a Six-Port network provides altogether two input and four output ports. Fig. 4.5 shows the circuit schematic of the proposed Six-Port architecture. The two inputs are denoted as $\underline{P_1}$ and $\underline{P_2}$ while the four output signals in baseband are B_3, B_4, B_5 and B_6. A power divider (PD) and three quadrature hybrid couplers (H) generate the mentioned phaseshifts and superimpose the signals additively. The four output signals $\underline{P_3}$, $\underline{P_4}$, $\underline{P_5}$, $\underline{P_6}$ are therefore result of an additive combination of the two input signals $\underline{P_1}$ and $\underline{P_2}$ according to eq. (4.3), (4.4), (4.5) and (4.6).

Diode-based power detectors are used as nonlinear devices for the down-conversion to baseband as described by eq. (4.7), (4.8), (4.9) and (4.10). One port of a quadrature hybrid coupler is terminated with a $50\,\Omega$ matched

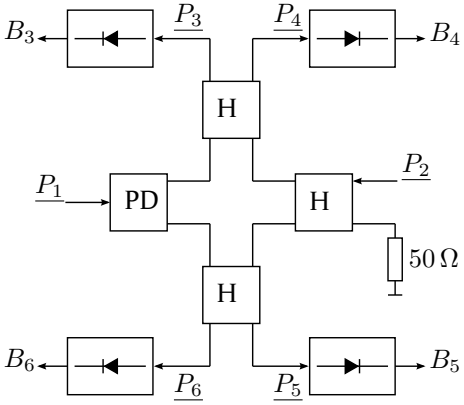

Figure 4.5: Implementation of the Six-Port receiver with circuit components.

load (assuming that the reference microstrip line impedance is set to the standard value of $50\,\Omega$). A Wilkinson power divider is hereby introduced in the PD circuit component, nevertheless, other types of power dividers can be implemented as well. In the following sections, these microstrip components will be presented and discussed, explaining the signal relationships leading to the core function of the overall Six-Port receiver.

4.2.2 Wilkinson Power Divider

Power dividers are passive microwave components used for power division or power combining. For power division, an input signal is divided into at least two signals [11]. In case of a two-signal power splitting the divider is a common three-port component. The introduced power divider is of equal-division type (input signal power is equally splitted to the two outputs) nevertheless, unequal power division can also be reached, according to the weighting of the different impedances in the circuit.

The increasing diffusion of microstrip circuits led to the development of planar dividers such as the Wilkinson power divider (Fig. 4.6) which splits the input power from port 1 to the output ports 2 and 3, keeping ports 2 and 3 isolated from each other [55]. The circuit can be conveniently analyzed with an "even-odd" mode analysis as described in [11]. However, in this section, only a brief overview will be given. Its behavior can be summarized with the complex scattering parameter matrix of a three-port device as [11]:

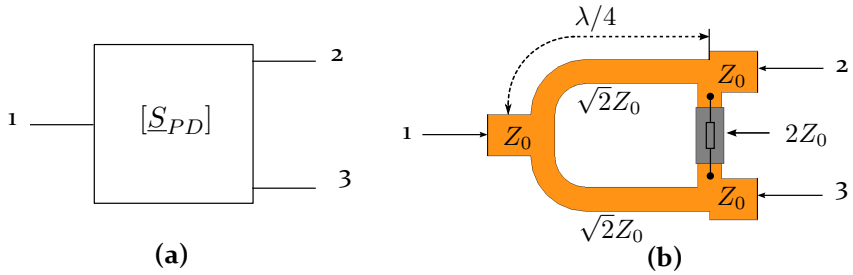

Figure 4.6: Schematic three-port network representation of the Wilkinson power divider **(a)** and its implementation in microstrip technology **(b)**.

$$[\underline{S}_{PD}] = \begin{bmatrix} 0 & \frac{-j}{\sqrt{2}} & \frac{-j}{\sqrt{2}} \\ \frac{-j}{\sqrt{2}} & 0 & 0 \\ \frac{-j}{\sqrt{2}} & 0 & 0 \end{bmatrix}. \tag{4.26}$$

Essentially, the power divider is made of an input port represented by a microstrip line with reference line impedance $Z_0 = 50\,\Omega$ connected to the two output ports (microstrip lines with $Z_0 = 50\,\Omega$ as well) through two quarter-wave transformers ($\lambda/4$ length) with $\sqrt{2}Z_0$ line impedance. Furthermore, between the two output ports a lumped impedance match of $2Z_0$ is present.

The Wilkinson power divider requires a lumped component to be placed on the microstrip circuit as an impedance match for the output ports [50]. Nevertheless, as discussed earlier, since in microstrip technology the transmission lines are directly exposed on the dielectric/air interface, the placement of lumped components on the surface of the microstrip line is not a problem. That is the reason why the Wilkinson power divider is so widespread in microstrip technology and is hereby chosen as a power divider for the Six-Port receiver.

4.2.3 Quadrature Hybrid Coupler

Directional couplers are modeled as four-port networks. Generally, any reciprocal, lossless, matched four-port network is a directional coupler [11]. Signal power at port 1 is delivered to port 2 and partially coupled to port 3 (Fig. 4.7). In an ideal directional coupler, no power is delivered to port 4, that means, port 4 is isolated [11].

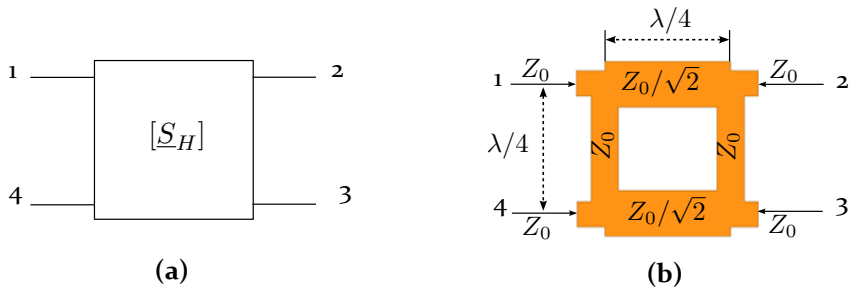

Figure 4.7: Schematic four-port network representation of the quadrature hybrid coupler **(a)** and its implementation in microstrip technology **(b)**.

To describe a directional coupler, Coupling (C), Directivity (D) and Isolation (I) are hereby introduced. The C relates the power coupled to the output port 3 with the input power at port 1. The D indicates the coupler's ability to separate forward and reverse waves and is therefore related to I describing the ratio between parasitic signal power coupling on port 4 and input power at port 1 [11]. Coupling, directivity and isolation are related as follows:

$$I = D + C \,\text{dB}. \tag{4.27}$$

Hybrid couplers are special cases of directional couplers, where the coupling factor is $C = 3\,\text{dB}$. Hybrid junctions have either a 90 DEG or a 180 DEG phase shift between the output ports 2 and 3. The quadrature hybrid has a 90 DEG phase shift between ports 2 and 3. This behavior can be summarized with the complex scattering parameter matrix of a four-port device as [11]:

$$[\underline{S}_H] = \begin{bmatrix} 0 & \frac{1}{\sqrt{2}} & \frac{j}{\sqrt{2}} & 0 \\ \frac{1}{\sqrt{2}} & 0 & 0 & \frac{j}{\sqrt{2}} \\ \frac{j}{\sqrt{2}} & 0 & 0 & \frac{1}{\sqrt{2}} \\ 0 & \frac{j}{\sqrt{2}} & \frac{1}{\sqrt{2}} & 0 \end{bmatrix}. \tag{4.28}$$

The quadrature hybrid coupler features four ports matched at the reference line impedance $Z_0 = 50\,\Omega$. Quarter-wave transmission lines connect port 1 and port 4, as well as port 2 to port 3, while quarter-wave branches with $Z_0/\sqrt{2}$ line impedance are placed between ports 1 and 2 as well as between port 4 and 3 (Fig. 4.7). This symmetric construction leads to the 3 dB cou-

pling factor. The isolation of port 4 is due to destructive superposition of wave components deriving from port 1.

Of course, this implies that the coupler is accurately designed to match the quarter-wave dimensions. In a real-world design this is not a trivial task, since (as explained in section 4.2.1) the wavelength depends on the substrate material on which the microstrips are build. The dielectric constant ϵ_r of the substrate is often not exactly known or is not constant over all the substrate. Thus, the equivalent wavelength of the signal propagating through the microstrip line is not precisely known. Therefore, a perfect isolation on port 4 is never reached and small portions of the signal coupled on port 1 leak through port 4, leading to a finite isolation value (I).

4.2.4 Diode-Based Power Detector

A power detector is a two port device (Fig. 4.8). The two ports of a detector are the RF port 1 (input) and the so called "video"[3] port 2 (output). The detector rectifies an input RF signal at port 1, converting it to baseband at port 2 by using the transfer function of a nonlinear device. Common nonlinear devices used in detectors are diodes such as Schottky or tunnel diodes [20]. Beside the down-converted amplitude modulation, the output signal at the video port will contain also a DC offset because of the rectifying process [25].

As already mentioned, the most relevant component of the detector circuit is the nonlinear device, in this case, a Schottky diode. The nonlinear voltage-current transfer function enables a power-to-current conversion that is needed for the power detection process. An RF signal with a certain voltage amplitude is rectified by the diode as a unipolar current flow through the device (Fig. 4.9). In other words, the diode rectifies the incident power (interpreted as the square of the RF signal voltage amplitude) into an output current signal of one polarity with an amplitude proportional to the input power level [20]. The proportionality is given due to the so called "square-law" behavior of the nonlinear transfer function in the ideal case (this will be explained later on). This current is then transformed in a voltage signal by a resistor (the so called "video" resistor) taking advantage of the linearity of Ohm's law. Therefore, a positive voltage is generated as an output.

A capacitor, called video capacitance of the detector circuit, is placed after the diode to serve as an RF ground and a low-pass filter for the output cur-

[3] The term "video" has a historic origin, deriving from the development of television signal reception.

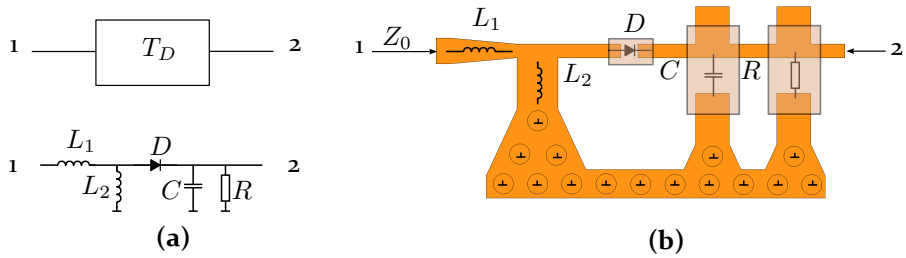

Figure 4.8: Two-port network representation of a detector (transfer function T_D) with a lumped element circuit schematic **(a)** and its implementation in microstrip technology **(b)**. The ground symbols on the microstrip picture **(b)** represent ground vias that connect to the lower ground plane of the PCB. Lumped components, such as D, R and C are marked with their packages.

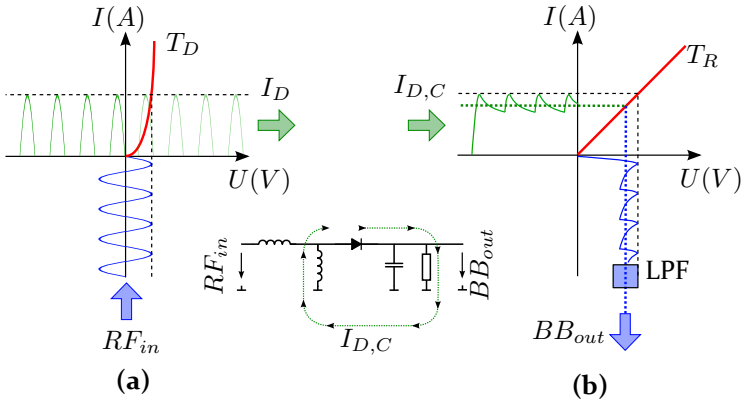

Figure 4.9: Voltage-current transfer function (T_D) of the detector diode **(a)** and of the video resistor (T_R) **(b)**. The input RF signal (RF_{in}) is rectified into a unipolar current signal (I_D) which is "smoothed" by the video capacitor ($I_{D,C}$). The current flows through the video resistor generating the output baseband voltage (BB_{out}) then returning to the diode through the DC return path (inductive RF choke).

rent signal from the diode. This capacitor determines the upper frequency limit of the video signal's bandwidth which is related to the minimum rise and fall time of the detector circuit (thus, how short a detectable RF pulse can be). A detector's output voltage is proportional to its incident power at port 1. This is valid for a certain range of power levels, if it is assumed that the transfer function of the diode is purely quadratic. This is normally not the case for real-world diodes.

However, this condition can be fairly approximated for a certain working-point region of the detector diode, where the quadratic term of the non-linear transfer function dominates over higher order terms[4]. As explained in section 3.2, all terms of the nonlinear transformation from the input to the output are generally present and weighted by appropriate coefficients p_k that can be seen in eq. (3.5). The quadratic term ($k = 2$) is hereby assumed to dominate over the other terms. The working-point region for which this condition is assumed is called "square-law" region. Furthermore, the ratio of output voltage to incident power

$$K = \frac{V_{out}(\,\mathrm{mV})}{P_{in}(\,\mathrm{mW})}, \tag{4.29}$$

is called open circuit voltage sensitivity (output of the detector diode is not loaded). For the square-law region K is therefore constant.

The diode usually does not feature a good input impedance match at the reference line impedance ($Z_0 = 50\,\Omega$), therefore, a matching network has to be implemented (inductive matching L_1 and L_2). Furthermore, in order for a detector to generate a DC voltage as an output, a DC return path must be implemented (Fig. 4.9). This is done by placing an RF choke (in form of an inductor L_2) in the input impedance match of the detector. At RF frequencies the inductor acts in worst case as an open circuit and has no effect, but at baseband frequencies it provides a low-impedance path to ground, allowing DC components to return to the reference potential.

The sensitivity of a diode can be improved by biasing the structure. This consists in adding a small DC voltage over the diode to drift the working-point slightly closer to forward conduction. This is useful for diodes with a

[4] An interesting description of detectors can be found in [55] at chapter 14, page 923. Erik L. Kollberg describes some common detectors explaining the basic semiconductor physics behind the phenomenon of power detection. Construction and packaging of detector devices are also described. Furthermore, at page 937, an optimization of diode detectors is also addressed, explaining low-level power detection as well as saturation of the detector device.

higher forward conduction voltage barrier. However, most detector diodes do not need to be biased. They are referred to as "zero-bias diodes" as through special semiconductor manufacturing processes the forward conduction voltage barrier is brought to a very low value near 0 V[5].

In this work, a detector configuration with inductive stub matching has been investigated. As previously mentioned, the matching network before the diode is formed by two inductive components realized by microstrip stubs. The *MZBD-9161* zero-bias Gallium-Arsenide (GaAs) beam lead Schottky diode from Aeroflex Metelics has been chosen for the hardware demonstrator working at a frequency of 24 GHz. The burn-out power of the diode is +20 dBm. A 1 pF capacitor and a 1 MΩ resistor have been chosen as video components. At low input signal power levels, the detector acts in the mentioned square-law region. At higher signal levels, the detector will become linear, and at even higher levels the detector saturates (Fig. 4.10). Due to the optimal inductive stub matching structure and to the high performance of the GaAs semiconductor device the proposed detector circuit offers a good detection performance for low input power signals down to -50 dBm and a good square-law or linear behavior up to approximately 0 dBm (Fig. 4.10). A silicon diode solution based on the *MSS20141-0402* zero-bias P-type Schottky diode (Aeroflex Metelics) has also been investigated, showing though low detection performance for low-power input signals. Nevertheless, the silicon diode shows excellent linearity.

4.2.5 The Six-Port Receiver Network in Microstrip Technology

With the circuit components introduces above, the complete Six-Port receiver network can be implemented. In Fig. 4.11 the resulting architecture in microstrip technology is shown. A pure Six-Port junction featuring a Wilkinson power divider and three quadrature hybrid couplers is shown in Fig. 4.11 **(a)**. It delivers the phase-shifted superpositions $\underline{P_3}$, $\underline{P_4}$, $\underline{P_5}$ and $\underline{P_6}$ of the input signals $\underline{P_1}$ and $\underline{P_2}$. In Fig. 4.11 **(b)** an optimized, compact receiver form with power detectors at the junctions' outputs is presented.

The latter one delivers the baseband signals B_3, B_4, B_5, and B_6 directly from the input signals $\underline{P_1}$ and $\underline{P_2}$. A complex I/Q receiver is thus implemented. I and Q are delivered as differential pairs as described in eq. (4.11), (4.12) and (4.13). This implies that one of the input signals is treated as reference source (LO). To obtain a correct phase shift relationship between the signals

[5] The reader is addressed again to chapter 14, page 939 of [55] for a complete description of zero-bias detectors.

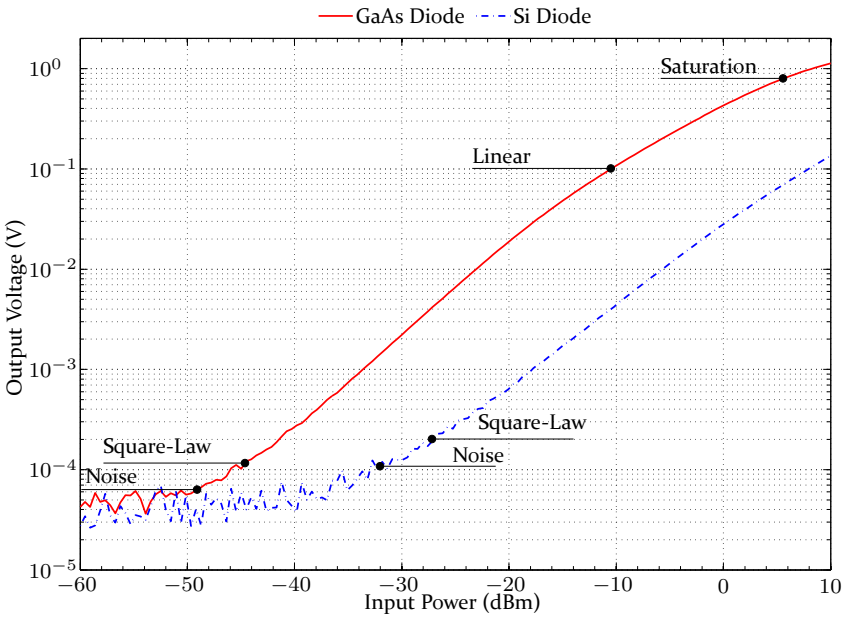

Figure 4.10: Measured detector transfer function for the *MZBD-9161* zero-bias Gallium-Arsenide (GaAs) beam lead Schottky diode and the *MSS20141-0402* zero-bias P-type Schottky diode from Aeroflex Metelics .

$\underline{P_1}$ and $\underline{P_2}$ at all four output ports it is important that the microstrip lines connecting the Wilkinson power divider and the three quadrature hybrid couplers feature the same electrical length.

For circuits where the microstrip components are fairly apart from each other, therefore making parasitic mutual coupling between the passive structures neglectable, this condition can be satisfied by using the same geometrical length for the interconnections. However, for compact designs such as the one presented in Fig. 4.11 **(b)** the phase of the signals at the output ports need to be verified by means of numerical simulations.

As mentioned in section 4.2, one port of a quadrature hybrid coupler is matched with a $Z_0 = 50\,\Omega$ load. This port is usually referred as the 7^{th} port [47]. Theoretically, no signal should pass through this port, as if seen from port 2 it should be perfectly isolated. Nevertheless, since in real-world components a perfect isolation is never reached, possible signal compo-

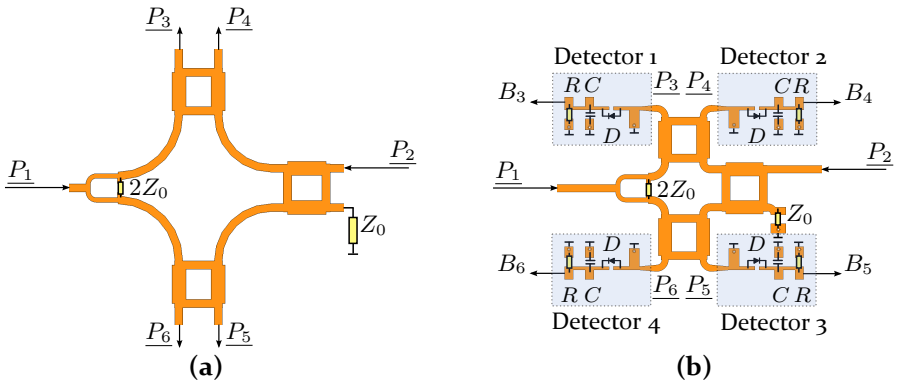

Figure 4.11: The Six-Port receiver network in microstrip technology as a simple combination of a Wilkinson power divider and three quadrature hybrid couplers **(a)** to generate the phase-shifted superposition $\underline{P_3}$, $\underline{P_4}$, $\underline{P_5}$ and $\underline{P_6}$ of the input signals $\underline{P_1}$ and $\underline{P_2}$ and a compact, optimized format featuring the detector circuits 1, 2, 3 and 4 **(b)** for a direct conversion to baseband (B_3, B_4, B_5, and B_6).

nents that leak to port 7 are absorbed by the matched load avoiding a further propagation through the coupler to the rest of the circuit.

The introduced Six-Port receiver can be used to demodulate a complex signal and to perform DOA estimation as well as ranging. The application of DOA estimation for the Six-Port receiver will be presented in the next chapter.

5 Six-Port Based DOA Detection

Direction finding techniques have been addressed and illustrated in chapter 2. It has been mentioned, that a complex receiver is needed to receive two complex signals $\underline{S}_{RX1}$ and $\underline{S}_{RX2}$ to perform a DOA detection. A brief summary is hereby given, aiming at introducing the Six-Port receiver to perform DOA angle detection.

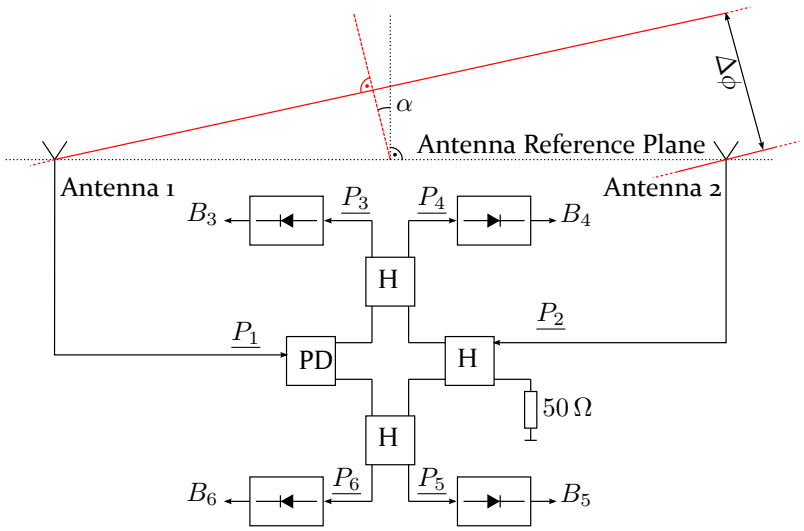

Figure 5.1: Six-Port based direction-of-arrival detector system.

5.1 The Direction-of-Arrival Detector System

Two complex valued signals $\underline{S}_{RX1}$ and $\underline{S}_{RX2}$ are received by two antennas. By performing a phase difference measurement between the two receiving antennas aligned on a reference axis, the DOA angle of an incident wave

with respect to the reference axis can be calculated [6]. This result is expressed by eq. (2.26) derived throughout section 2.4.3. The phase difference between the two complex signals $\underline{S}_{RX1}$ and $\underline{S}_{RX2}$ can be measured by a complex receiver. For this purpose, the Six-Port, introduced in chapter 4, can be successfully implemented. In section 4.1 with eq. (4.14) and (4.22) it has been shown, that the phase difference between the two input signals $\underline{P}_1$ and $\underline{P}_2$ of the Six-Port receiver can be easily calculated from the four baseband signals B_3, B_4, B_5 and B_6 at the output ports of the detectors. It is therefore possible to perform DOA detection by using a Six-Port receiver.

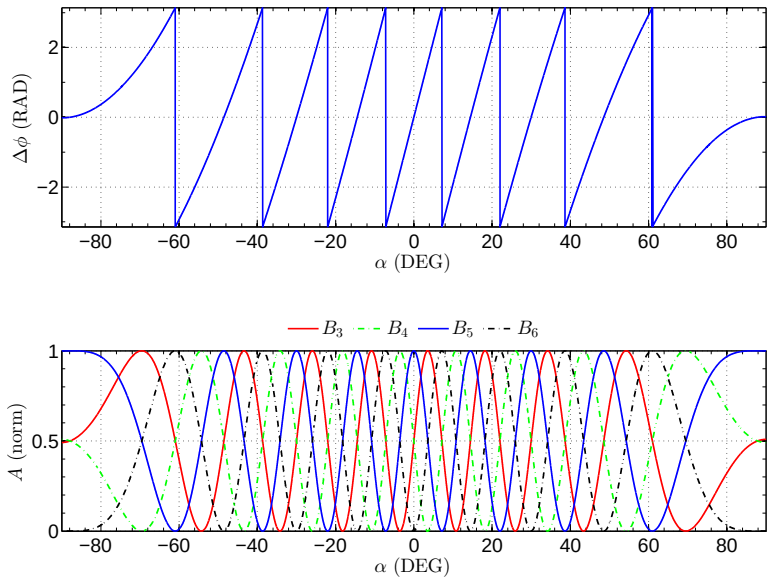

Figure 5.2: Phase difference $\Delta\phi$ and baseband signals B_3, B_4, B_5 and B_6 in function of the incident angle α.

The concept is illustrated in Fig. 5.1. The two antennas needed for the DOA estimation are connected to the two input ports of the Six-Port receiver. The phase fronts of the incident wave are highlighted in red. The two received signals interfere with each other in the Six-Port network generating the four phase-shifted superpositions at the Six-Port's outputs and are subsequently down-converted to baseband by power detectors, as explained in chapter 4. For this configuration, no reference source such as an LO is needed. The system is completely passive in the RF and extremely sensitive to phase variations, being based on the Six-Port interferometer prin-

ciple (additive mixing). Since the received signals are combined together to down-mix themselves to baseband without the need of a reference LO, the phase difference results only from a different incident angle of the detected wave on the reference plane and cannot be caused by phase noise of a reference LO. This implies a very high angular resolution. By combining eq. (2.26) in chapter 2 with eq. (4.14) in chapter 4 it is possible to calculate the DOA angle. The relationship between the incident angle α and the detected DOA angle from the baseband signals B_3, B_4, B_5 and B_6 of the Six-Port receiver, through the phase difference $\Delta\phi$ expressed by eq. (4.22), is therefore given by

$$\alpha = \sin^{-1}\left[\tan^{-1}\left(\frac{B_3 - B_4}{B_5 - B_6}\right)\frac{\lambda}{2\pi L}\right], \tag{5.1}$$

where λ is the wavelength of the signal and L is the distance between the two receiving antennas as explained in section 2.4.3. The detected phase $\Delta\phi$ is

$$\Delta\phi = \tan^{-1}\left(\frac{B_3 - B_4}{B_5 - B_6}\right). \tag{5.2}$$

$\Delta\phi$ and the baseband signals B_3 to B_6 are plotted in Fig. 5.2 for a DOA detector operating at a frequency of 24 GHz ($\lambda \approx 12.5$ mm) and $L = 50$ mm. The DOA range is limited to a half plane, that is from -90 to +90 DEG. This range is give due to the limits of the arc-sine function that is defined only between -90 to +90 DEG. Nevertheless, this is not a limitation for the addressed applications, as explained in [47] (at page 57-59).

5.2 The Ambiguity Issue

The sinusoidal dependency of $\Delta\phi$ on the incident angle α can be easily noticed in Fig. 5.2. Another important phenomenon can be seen as well. The phase difference and the baseband signals feature an irregular periodicity over the incident angle. This "phase wrap" effect is due to the nature of the phase difference of the signals received by the system and depends on the ratio between the wavelength λ of the detected signal and the distance L between the receiving antennas. This effect has major consequences on the DOA detection technique hereby addressed. For $L/\lambda \leq 0.5$, $\Delta\phi$ will not wrap, thus, the complete half-plane DOA range is covered by the range of

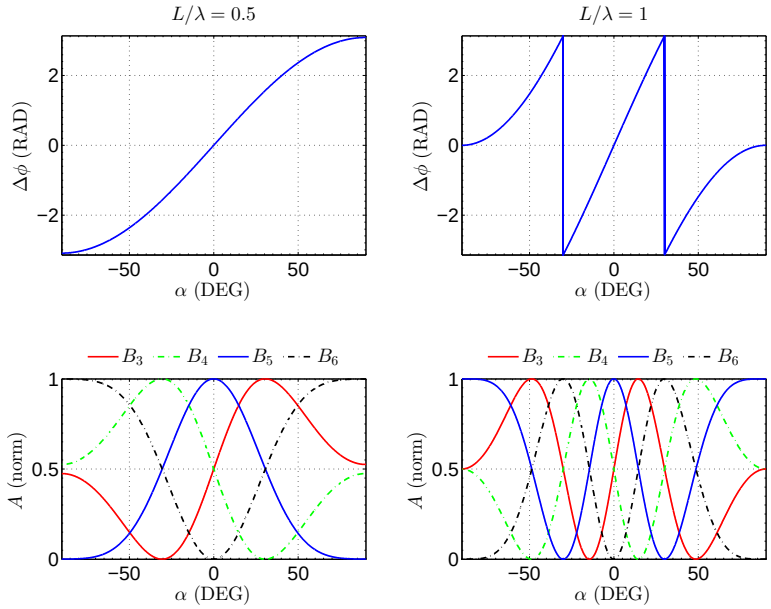

Figure 5.3: $\Delta\phi$ and baseband signals B_3, B_4, B_5 and B_6 in function of the incident angle α for $L/\lambda = 0.5$ and for $L/\lambda = 1$.

$\Delta\phi$. This leads to a non-ambiguous DOA detection. For $L/\lambda > 0.5$, the phase will wrap within the chosen DOA range thus, leading to an ambiguity in the detection. In Fig. 5.3 this dependency is shown for $L/\lambda = 0.5$ and for $L/\lambda = 1$.

At a first glance, this effect appears easily avoidable by simply choosing $L = \lambda/2$. Practically though, this condition is not easy to be satisfied. First of all, the placement of two antennas at a distance of $\lambda/2$ implies a strong coupling between the two structures and is in some cases not feasible. Furthermore, by mapping the complete DOA range of ± 90 DEG on the phase difference range from $-\pi$ to $+\pi$ RAD the detection accuracy decreases because of the limited phase resolution of the receiver, expressed in chapter 2 as $\Delta\phi_{min}$ in eq. (2.28).

Of course, if for the addressed application the DOA detection range of interest is smaller than ± 90 DEG, L has to be chosen according to eq. (2.27). Nevertheless, the angular resolution (that is the smallest detectable DOA angle) described by α_{min} in eq. (2.28) will be limited by L_{max} and $\Delta\phi_{min}$. It is therefore usually a question of trade-off when choosing L between a sys-

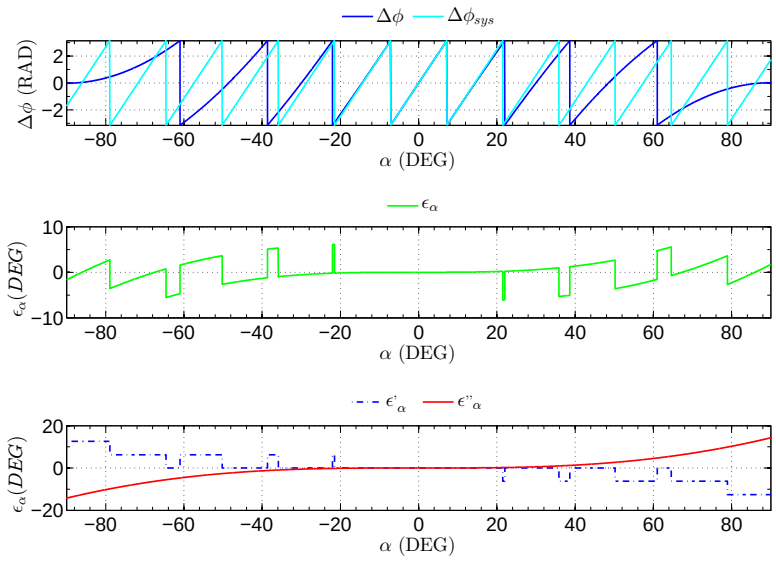

Figure 5.4: Phase difference $\Delta\phi$ caused by an incident angle α and phase difference $\Delta\phi_{sys}$ of a system affected by ambiguity with errors ϵ_α, ϵ'_α and ϵ''_α.

tem that features a large non-ambiguous DOA detection range with limited angular resolution, or a system with high resolution DOA detection and a limited non-ambiguous range.

This problem is referred to as the ambiguity issue and affects generally all DOA detection systems. As a solution to this problem, the dual Six-Port receiver will be proposed, in chapter 6. In case of a system affected by the ambiguity issue, the detected DOA for incident angles α larger than the non-ambiguous range will feature an error

$$\epsilon_\alpha = \sin^{-1}\left[(\Delta\phi - \Delta\phi_{sys})\,\frac{\lambda}{2\pi L}\right] = \epsilon'_\alpha + \epsilon''_\alpha, \tag{5.3}$$

that is characterized by an offset error $\epsilon'_{\Delta\phi}$ with amplitude steps equal to multiples of the half of the non-ambiguous range and a nonlinear error component $\epsilon''_{\Delta\phi}$. This can be observed in Fig. 5.4. The wraps due to $\epsilon'_{\Delta\phi}$ are easy to compensate in digital signal processing with unwrap functions, but the nonlinear error component $\epsilon''_{\Delta\phi}$ cannot be compensated since the DOA de-

tector system inherently makes use of the $\Delta\phi_{sys}$ transfer function instead of the real phase difference $\Delta\phi$ to calculate the DOA angle.

It has to be underlined, that even $\Delta\phi_{sys}$ is not a linear sawtooth-like function but it features sinusoidal nonlinearity within the non-ambiguous range. For small non-ambiguous ranges due to a ratio $L/\lambda >> 0.5$ this nonlinearity becomes negligible.

5.3 DOA Detection and Tracking

As illustrated in Fig. 5.2, 5.3 and expressed by eq. (2.26) in chapter 2 the phase difference $\Delta\phi$ has a sinusoidal dependency on the incident angle α. A fair linear approximation can be done for DOA angles around zero (DOA orthogonal to the reference axis where the receiving antennas are aligned). This can be useful for certain application scenarios, for instance, in case of tracking applications that need to constantly perform a zero alignment of the DOA detection system with the incident angle, for example systems which track and follow radiating sources or passive scatterers.

A detection of the absolute DOA angle is needed for an initial estimate. The detection system is mechanically rotated, therefore, the reference plane for the estimation of the DOA angle can be adjusted. A feedback loop continuously evaluates the DOA angle calculated from the baseband signals of the Six-Port receiver and rotates the reference plane in order to minimize the DOA angle of the incoming signal. The feedback loop is implemented to work in real time. By doing so a transmitting source or a reflecting target can be continuously tracked by DOA estimation and by rotating the reference plane with the goal to reach a DOA angle of zero (zero alignment). This special implementation of the proposed DOA detector system takes therefore an advantage of the linear approximation of the transfer function.

The DOA detection is bound to a nonlinear function dependent on the four output voltage values delivered from the Six-Port receiver and on the distance L between the two receiving antennas as can be seen in eq. 5.1. The arc tangent defining the phase difference $\Delta\phi$ delivers a linear phase difference defined from $-\pi$ to π RAD as expressed in eq. 5.2.

Although the DOA angle is nonlinearly dependent on the phase difference $\Delta\phi$, within a small range around $\Delta\phi = 0$ RAD the DOA angle α expressed in eq. 5.1 can be assumed to be linear (small signal approximation of a sinusoidal function). This range (that can be linearly approximated) can be then

expanded to match the whole phase difference by increasing the distance L between the receiving antennas. In this way, the arc-sine function expressed in eq. 5.1 can be neglected. This simplification is beneficial for systems that perform zero alignments on a reference axis. Furthermore, for DOA detectors with a variable antenna distance L, the DOA detection can start with a coarse approximation when the antennas are close to each other, then an exact detection can take place when the antenna distance L is increased. An exact detection can be performed even ignoring the sinusoidal dependency between $\Delta\phi$ and the DOA angle α.

5.4 Demonstrator Technology Overview

As hardware demonstrators two Six-Port based DOA detectors are hereby presented, addressing different technology implementations as well as different application scenarios. A first demonstrator has been implemented in microstrip technology on an RF substrate, for a detection of microwave signals at 24 GHz. This demonstrator will be presented in section 5.5. Furthermore, a second demonstrator has been built to detect signals at a higher frequency of 77 GHz, featuring an integrated Six-Port receiver in Silicon-Germanium (SiGe) bipolar technology (section 5.6). This integrated receiver has been developed by Dr.-Ing. B. Lämmle during research work for his doctoral thesis and is presented in [56–58].

5.5 Six-Port Demonstrator at 24 GHz

The DOA detection demonstrator has been designed with a variable antenna distance L, to verify the detection and tracking capabilities as described in section 5.3. A System concept overview can be seen in Fig. 5.5. As introduced above, the system transfer function relates the incident angle with the detected phase difference between the receiving antennas on the reference plane.

For a small DOA angle around zero, the sinusoidal transfer function can be assumed to be linear. As soon as a minor difference between the detected DOA angle and the rotation of the reference plane is present, the system counteracts by correcting the position of the reference plane. Within a small range around zero, the DOA detection system features very low nonlinearity, therefore, a very accurate tracking of a target can be performed, even

when implementing a linear approximation of the sinusoidal transfer function expressed by eq. (2.26).

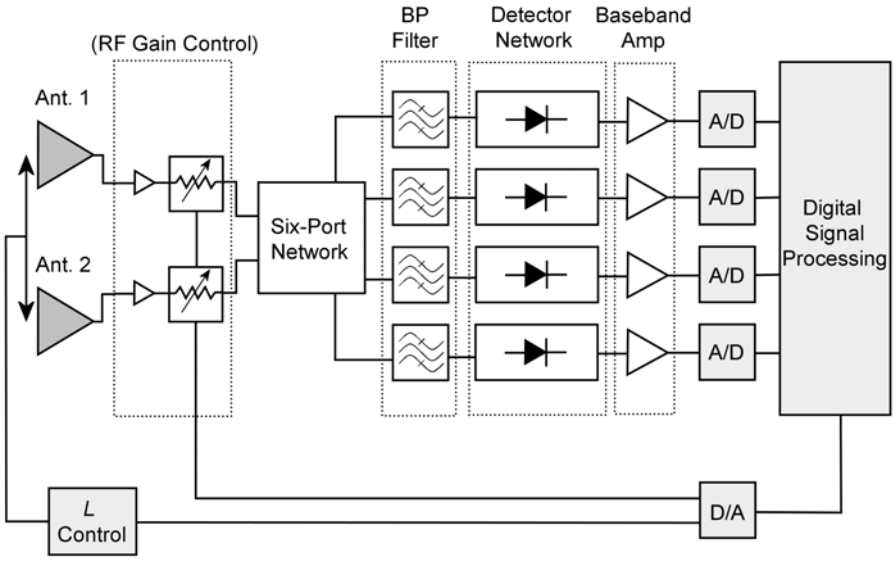

Figure 5.5: Six-Port DOA detection demonstrator system setup at 24 GHz [59]. (Copyright 2010, IEEE)

A system simulation in the Advanced Design System (ADS) software environment verifies the conclusions stated above. A detection starts with a small value of L (Fig. 5.6 **(a)**). The detection range for the angle of incidence is thus large easing the localization of the incoming signal direction with an initially low accuracy. Once a first estimation of the direction of arrival has been done, L can be increased thus decreasing the operational range of the detection system within which no ambiguity occurs (Fig. 5.6 **(b)**) and increasing the detection accuracy. This step can be successively repeated to reach the desired angular resolution.

In the ADS system simulation model the distance L between the two antennas is set initially to 5 cm (Fig. 5.6 **(a)**). As a next step L is increased to 20 cm increasing the accuracy of the system (Fig. 5.6 **(b)**). Ambiguities in the calculation of the DOA angle are evident and delimit the detection range. Measurements (Fig. 5.7 **(a)** and **(b)**) have been performed with the presented system showing excellent agreements to the system simulations in ADS (Fig. 5.6 **(a)**). The plots do not include a measurement offset and show the raw measurement results. The measured angle is compared to the incident angle. A good linearity can be noticed when comparing the curve

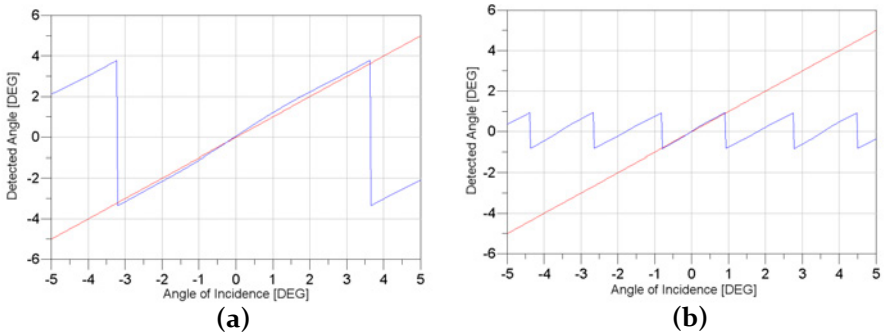

Figure 5.6: Simulation result (ADS) of the detected vs. incident angle with **(a)** $L = 5\,\text{cm}$ and **(b)** $L = 20\,\text{cm}$ according to [59].
(Copyright 2010, IEEE)

to an ideal linear function. A description of the measurement setup is presented in section 5.5.4.

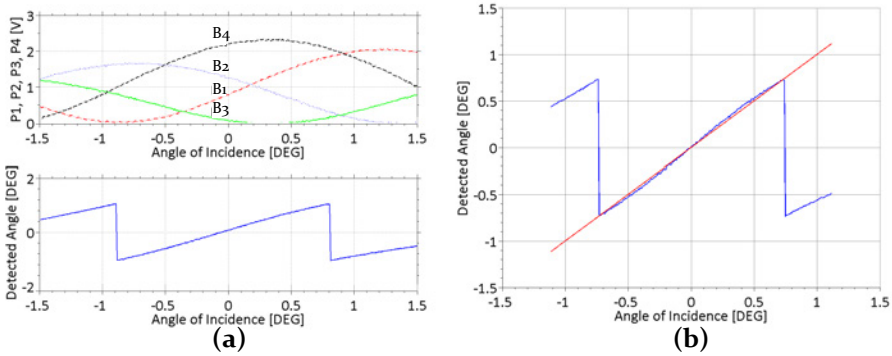

Figure 5.7: Measured output voltages vs. incident angle **(a)** and measured vs. incident angle **(b)** as presented in [59].
(Copyright 2010, IEEE)

5.5.1 Six-Port Network and Front-End Design

As can be seen in Fig. 5.5, apart from the Six-Port network the proposed DOA detection demonstrator consists of other important components. The two input signals arriving from the antennas need to be amplified or attenuated before entering the Six-Port network. Assuming a very low incoming signal power, a proper Low-Noise Amplifier (LNA) stage is required to guarantee an overall good dynamic range. In the demonstrator two Hittite

HMC341LC3B LNAs are used with a gain of 13 dB and a noise figure of 2.5 dB.

The signals on the other hand sometimes also need to be attenuated. If the input power is too high, the GaAs zero-bias detector diodes at the output of the Six-Port receiver are driven in a non-quadratic region of the characteristic transfer function adding higher order terms to the output voltage signals $B_3 \ldots B_6$. This leads to a distortion of the arc tangent function thus increasing the detection error. Therefore, to avoid over-driving the diodes, two variable attenuators have been introduced (Hittite HMC812LC4).

At the four outputs of the Six-Port network, coupled line band-pass filters are introduced before entering the detector stage to avoid the detection of potentially present interferences and to isolate at baseband frequencies the detector network from the Six-Port structure (DC decoupling). Further investigations showed that the band-pass filters are not needed to guarantee good working conditions, therefore, newer Six-Port front-end designs do not include them.

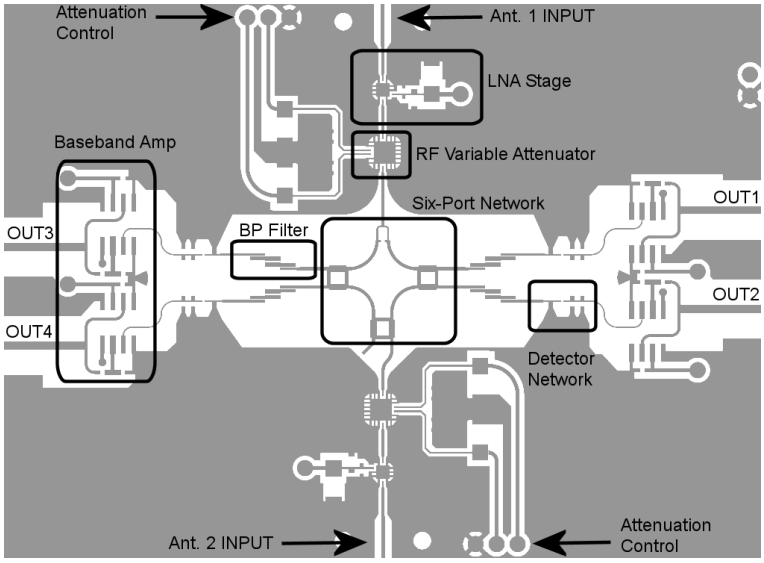

Figure 5.8: PCB layout of the DOA detection system as in [59].
(Copyright 2010, IEEE)

5.5.2 Baseband Signal Conditioning

To calculate the incident angle, the four baseband voltage signals need to be properly processed. For this purpose, the very low voltages present at

the detector diodes are amplified with the LMP7707MA rail-to-rail operational amplifiers from National Semiconductor in non-inverting configuration. From a voltage range of some milli-volts the signals are amplified to a range between 0 and 2 V. The analog voltage signals are then brought to the digital domain by four Analog-to-Digital Converters (ADC) with a resolution of 12 bit. The four ADCs are triggered simultaneously by a synchronous signal and deliver the digitized values at the same time on four 12 bit Serial Peripheral Interface (SPI) bus connections to a central Digital Signal Processing (DSP) board. A feedback from the digital domain to the analog world is provided by a Digital-to-Analog Converter (DAC) that delivers the proper voltages for the RF gain control stage (voltages at the variable attenuators) and positioning information for the antenna stage control to adjust the distance L. Fig. 5.8 shows the analog PCB layout with the RF inputs, RF gain control stages, Six-Port network, BP filters, detector networks and baseband amplification stages. The manufactured PCB can be seen in Fig. 5.9.

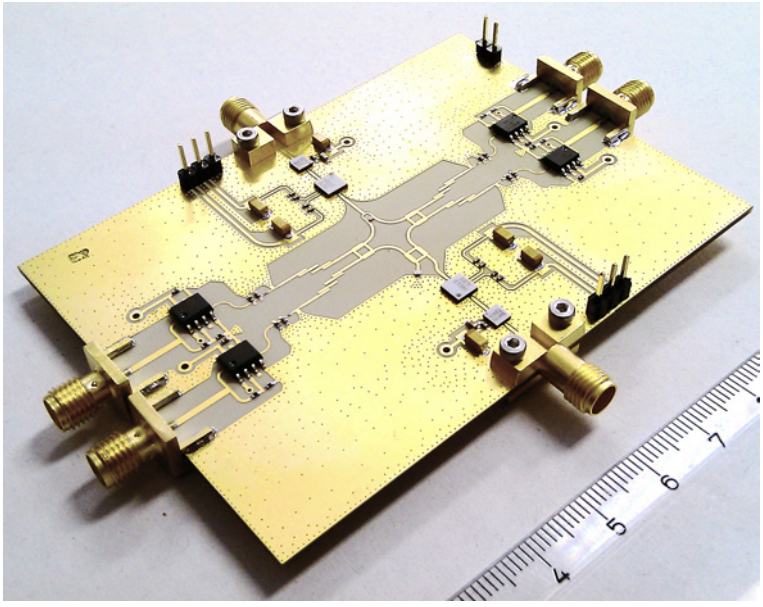

Figure 5.9: Picture of the manufactured PCB as in [59].

5.5.3 Analog - Digital Interface

For the demonstrator setup a dedicated analog-to-digital interface has been developed[1]. The four outputs of the Six-Port receiver are connected to ADCs with 12 bit resolution and 200 KSps sampling rate. The acquisition and the data manipulation is done by a signal processing board based on the Altera Cyclone II (2C35) Field Programmable Gate Array (FPGA). The four ADCs are sampling synchronously delivering the data via a parallel bus to the FPGA. A Nios II softcore processor implemented inside the FPGA calculates the DOA angle and the misalignment angle. The processor also compensates the calculated values with a 5^{th} order polynomial function based on previous calibration procedures. The calibration coefficients are stored inside the board and can be updated remotely via an RS-232 port connected to a computer running Matlab which also acquires the data and plots the results.

5.5.4 Measurement Setup

Following the theory presented in chapter 2, especially the techniques described in section 2.4, both DOA as well as misalignment angles have been measured. Two main scenarios have been investigated. The signal can be radiated from an unknown source that has to be detected and tracked (DOA measurement) or from a reference transmitter where its orientation needs to be determined (misalignment detection).

An evaluation of the detection performances requires a high-precision mechanical setup for coherent results. The setup consist of a dummy transmitter sending a continuous wave at a frequency of 24 GHz and a power level at the antenna connector of 0 dBm as well as a test receiver both positionable with high-precision mechanical rotation and translation stages. The distance between the two systems (transmitter and receiver) is fixed at 2.2 m. The receiver is based on a two-constraints system, that allows to rotate the reference axis on which the two receiving antennas are mounted and to adjust the distance between the receiving antennas.

The dummy transmitter is also based on a two-constraints system. The first degree of freedom is the rotation of the transmitting antenna and the second constraint is the linear translation of the dummy transmitter with two linear stages: a large stage for long translations with moderate accuracy and

[1] The analog-to-digital interface has been designed and build with a joint cooperation project between Stefan Lindner, Francesco Barbon and the author.

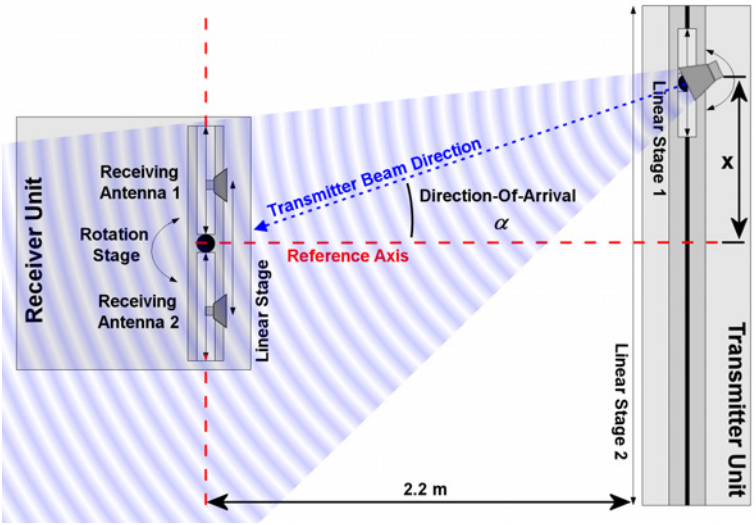

Figure 5.10: Direction-Of-Arrival measurement setup [60].

a small stage for short but accurate translations. As introduced in the previous paragraph, the system under test can be used for two different measurements: DOA detection and misalignment angle measurement. The setup therefore has two different configurations. The two receiving antennas are connected to the Six-Port receiver which compares the phase of the two incoming signals.

5.5.5 Measurement Results for DOA Detection

The first measurement results are based on the DOA detection setup where the transmitter antenna is moved with the long and short linear stages. This linear shift introduces an equivalent DOA angle.

Since the transmitting antenna is directional and strongly focused, a rotation offset has been implemented to keep the receiver within the main radiation lobe of the transmitter. As shown in Fig. 5.11 and Fig. 5.12 the detection system is very accurate for angles of incidence within 2.5 DEG and a good linearity can be noticed also for very small angles within 0.025 DEG. The plots in Fig. 5.11 and Fig. 5.12 are based on raw acquisition data without calibration.

The excellent linearity of the results demonstrate the high accuracy and reli-

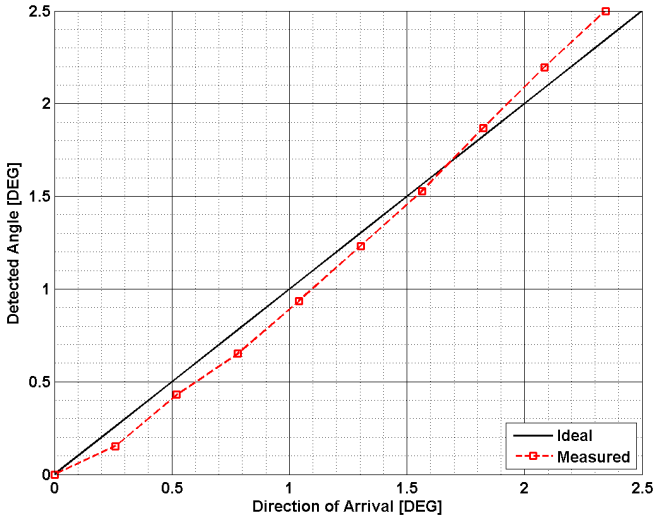

Figure 5.11: DOA measurement: range from 0 to 2.5 DEG [60].
(Copyright 2011, IEEE)

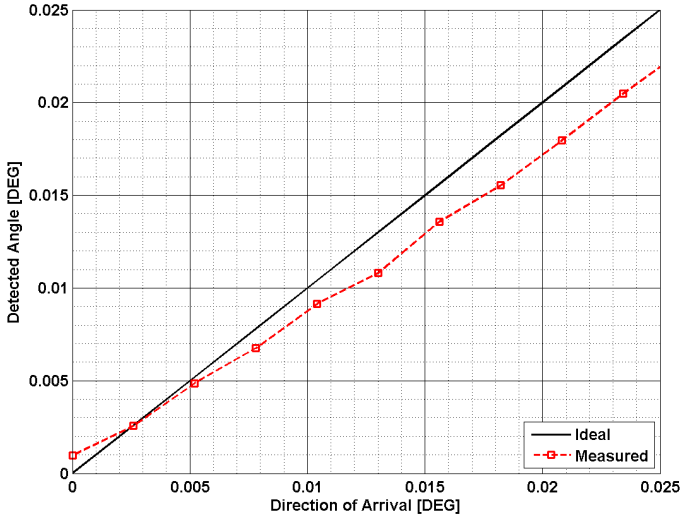

Figure 5.12: DOA measurement: range from 0 to 0.025 DEG [60].
(Copyright 2011, IEEE)

ability of the proposed detection system. The maximum measurement rate of the calculated DOA angle is 500 Sps. The dramatic decay in the measurement frequency from 200 KSps delivered by the ADCs to only 500 angle values per second is due to the delay introduced by the digital signal processing. Nevertheless, the system is still quick enough for a fast feedback and response since 500 Hz is a good refresh rate for most applications.

5.5.6 Measurement Results for Misalignment Angle Detection

Other measurements (Fig. 5.14 and Fig. 5.15) are based on the misalignment angle detection as shown in Fig. 5.13. In this case, the transmitter is

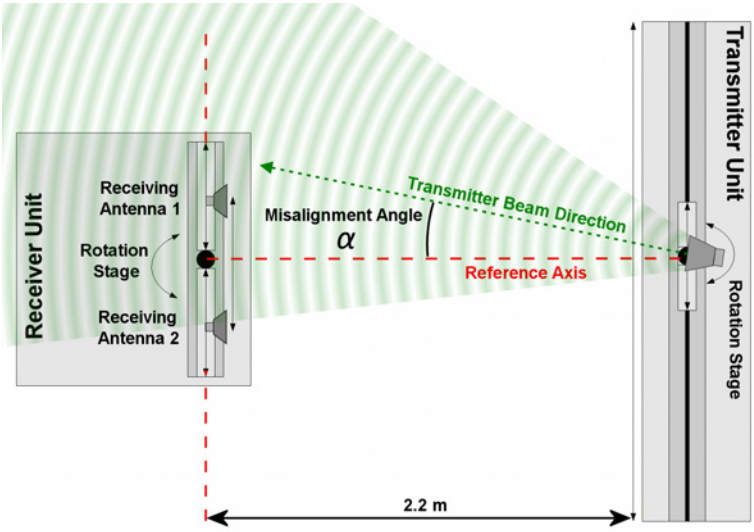

Figure 5.13: Misalignment angle measurement setup [60].
(Copyright 2011, IEEE)

aligned with the receiver's reference axis and the transmitting antenna is rotated introducing a misalignment angle between the reference axis and the transmitter beam direction. In Fig. 5.14 a misalignment angle between -3 and +3 DEG is plotted showing excellent linearity. The measurement curves have been compensated using a 5th order polynomial approximation generated during the calibration procedure. In Fig. 5.15 a misalignment angle from -1 to +1 DEG is shown. The response is still highly linear with some superimposed noise due to environmental influences of the surroundings in the measurement room.

Figure 5.14: Misalignment measurement: range from -3 to 3 DEG [60].
(Copyright 2011, IEEE)

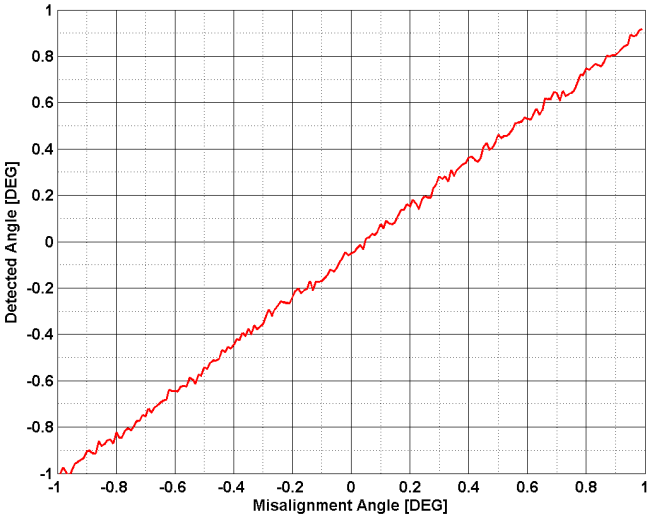

Figure 5.15: Misalignment measurement: range from -1 to 1 DEG [60].
(Copyright 2011, IEEE)

5.6 Six-Port Demonstrator at 77 GHz

In this chapter the design of a 77 GHz direction-of-arrival detector system with an integrated Silicon-Germanium (SiGe) Six-Port receiver and a passive microstrip antenna network is presented. A typical problem of millimeter-wave integration is the interface between the on-chip circuitry and the off-chip system electronics or passives. The antenna design aspects and interconnections are presented with a layouting analysis as well as a system overview of the DOA detector for a flexible, low-complexity and low-cost solution in microstrip technology.

The integrated SiGe Six-Port receiver is embedded in a microstrip-based passive circuit including a chip sink, RF bonding, patch antennas and feeding networks for optimal performance at the system frequency. A set of geometrical constraints due to the desired observation range of the detector and the physical size of the components and microstrip structures drive the design strategy for the complete system. This device is intended to be used as a misalignment angle detector for long-range automotive radar calibration operating at 77 GHz. This application is explained in detail in chapter 10 section 10.1.

5.6.1 The Integrated Six-Port Network

The integrated Six-Port receiver front-end[2] (Fig. 5.16) has two input LNAs, a broadband passive Six-Port network, and four high responsiveness power detectors [58]. The whole integrated circuit has a power consumption of 95 mW from a 5 V supply and is fabricated in a 200 GHz transit frequency SiGe bipolar technology. Total size is 1028 x 1128 μm^2 [61]. The system does not include an oscillator source since the Six-Port is based on the additive self-mixing effect [41] of the two input signals. The fabricated circuit in SiGe technology is not perfectly matched to 50 Ω, but the return loss is lower than -7 dB from 70 to 90 GHz and nearly identical for the two ports (verified by measurements). Therefore, the circuit has to be matched to the antennas having a 50 Ω normalized impedance.

[2] The integrated Six-Port receiver front-end has been developed by Dr.-Ing. B. Lämmle during research work for his doctoral thesis [58] and realized in Silicon-Germanium (SiGe) bipolar technology by Infineon Technologies AG. Further information can be found in [56, 57]. The author would like to thank Dr.-Ing. B. Lämmle for the joint project cooperation and the design of the SiGe chip, Christoph Wagner from DICE GmbH & Co KG, for the bonding of the chip and technical assistance. Furthermore, the author thanks Infineon Technologies AG for the fabrication of the SiGe chip.

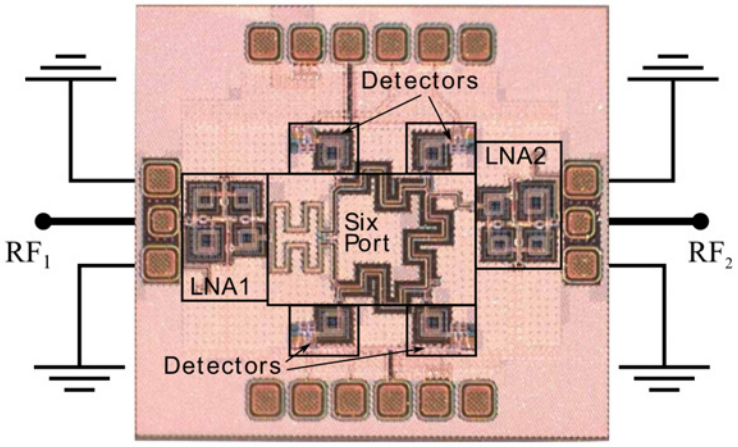

Figure 5.16: The integrated Six-Port receiver (chip) [62].
(Copyright 2012, IEEE)

5.6.2 System Design

The Six-Port receiver is fixed in a chip cavity fabricated on RF substrate with a thickness of 127 µm, the Rogers RT Duroid 5880 glass microfiber reinforced PTFE composite laminate ($\epsilon_r = 2.2$, $\tan\delta = 0.0009$). This specific substrate has been chosen because of its exceptionally low loss and due to its availability in thin laminates. The connecting pads are then bonded with 25 µm wedge/wedge bond wires having a typical bond-arc height of 100 µm. From the bond pads microstrip lines lead to the patch antennas fabricated with same duroid substrate on the 9 µm metallization.

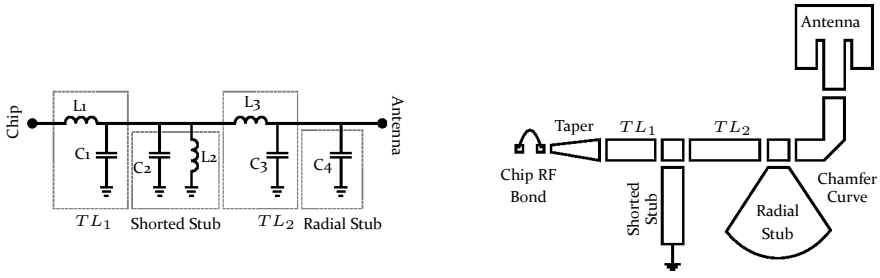

Figure 5.17: Matching network **(a)** and geometry **(b)**.

A mismatch can be found between the chip pads and the antennas due to the unmatched chip contacts and the strong inductive component of the bond wires. To compensate these effects a modified 'π' match is introduced (Fig. 5.17). A brass shielding covers the chip and the feeding networks to prevent unwanted coupling of the incoming signal on the microstrip structures.

The brass shield is coated with an Eccosorb BSR-U magnetically loaded, silicone rubber film that effectively dampens resonances due to its high permittivity and permeability. The patch antennas have been tuned to perform at a center frequency of 77 GHz with 2 GHz of bandwidth and less than -10 dB of return loss (Fig. 5.23). The impedance of 50 Ω is reached with the slot-in match on the microstrip patches. The shielding structure has a relevant influence on the antenna radiation characteristic. Therefore, it is mandatory to coat also the external surfaces of the brass shielding structure with Eccosorb BSR-U rubber. In this way a regular and symmetrical radiation characteristic can be obtained for both antennas (Fig. 5.21).

5.6.3 Geometrical Constraints and Layout

A typical misalignment angle of an automotive radar device installed on a vehicle deviates a maximum of 10 DEG from the geometrical reference axis to which it should be calibrated. It is therefore optimal to limit the observation range of the DOA detector to ± 10 DEG.

The antennas feature a radiation characteristic with a -3 dB main lobe width

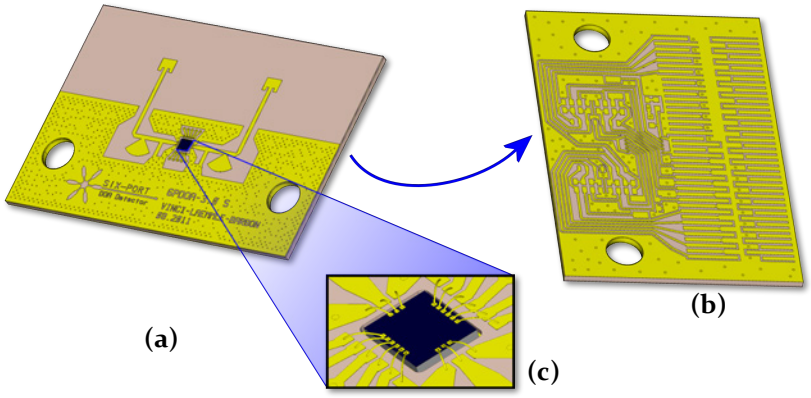

Figure 5.18: CAD model of the fabricated PCB. Top view **(a)**, bottom view **(b)** and the integrated Six-Port receiver **(c)**.

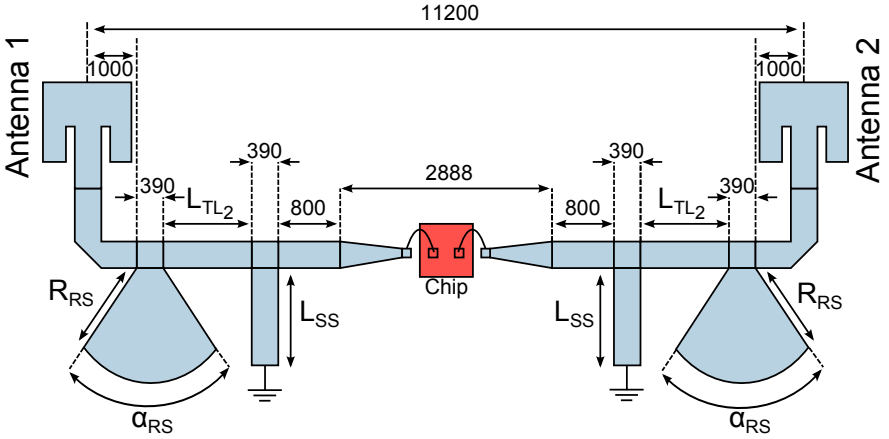

Figure 5.19: Geometrical layout constraints (dimensions in µm) [62].

of ± 30 DEG (Fig. 5.21), therefore, covering the above mentioned observation range of ± 10 DEG. For this purpose a distance of $L = 11.2$ mm between the two receiving antennas [60] can be set:

$$\theta_{obs} = \frac{\lambda\, 360}{2\pi\, L} = \frac{3.98\ \text{mm}\ 360}{2\pi\ 11.2\ \text{mm}} \approx 20\ \text{DEG}. \tag{5.4}$$

This geometrical constraint leads to design considerations for the antenna feed network. As evidenced in Fig. 5.19 the distance between the two antennas limits the tuning possibilities on the modified 'π' match. The fixed distance of 11.2 mm imposes a fixed length for *TL2*. The width of the bonded chip with RF-bonds and an adequate microstrip tapering is technologically fixed at 2888 µm. Input transmission lines in front of the shorted stub are also fixed at 800 µm length. Considering an optimal radius of 1000 µm for the chamfer curves the length of the transmission lines *TL2* is therefore limited to 1576 µm.

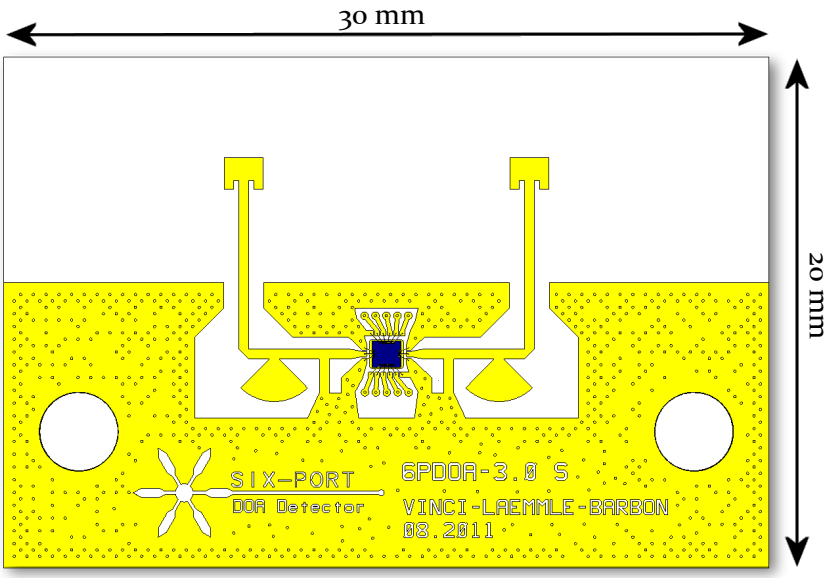

Figure 5.20: Layout of the DOA detector board.

5.6.4 Simulation Results

A CAD model (Fig. 5.20) has been parametrized and simulated with a full 3D electromagnetic solver software CST Microwave Studio using the transient solver covering the frequency range from 60 to 90 GHz. All lossy materials have been modeled with their respective properties. The matching is done by tuning the radius R_{RS} and angle α_{RS} of the radial stub as well as length L_{RS} of the shorted stub.

The return loss measurement data from the integrated Six-Port receiver has been imported as a scattering parameter matrix and connected to the passive structure in the 3D model. The overall analysis and the final results have been obtained with a co-simulation process within the CST Design Studio environment, merging the 3D simulation data and the chip measurements. The results are shown in Fig. 5.23.

A critical part of the manufacturing process is the bonding of the chip. The control over the bonding procedure allows a tolerance of the bond height. As introduced before, a typical RF-bond wire has a height of $h = 100\,\mu\text{m}$ as can be seen in Fig. 5.22. A variation of the height within $\pm 50\,\mu\text{m}$ has to be taken into account when designing the microstrip path to the antennas.

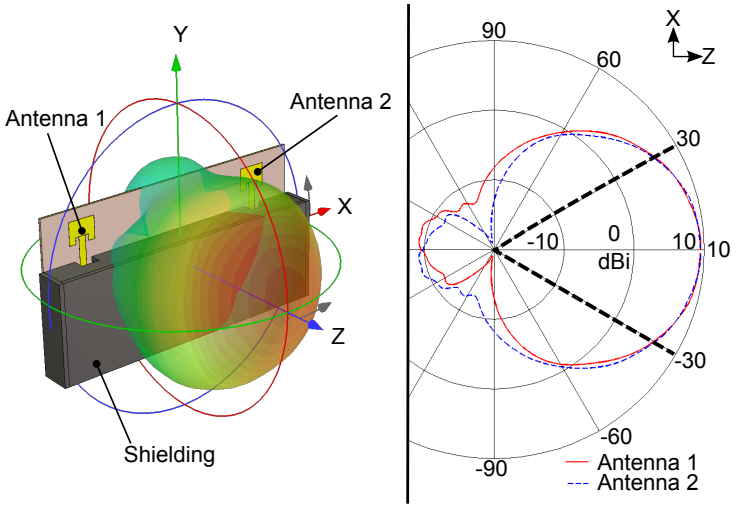

Figure 5.21: Directivity pattern and reference geometry [62].
(Copyright 2012, IEEE)

By means of a yield analysis, the bond height tolerance can be taken into account in the simulation flow. The results show an acceptable variation in the transmission loss as well as tolerable change in the reflection coefficient at the antennas with a variation from 50 µm to 150 µm (Fig. 5.24). The transmission loss, for instance, changes from -5 dB for a bond height of 50 µm to approximately -7 dB for 150 µm.

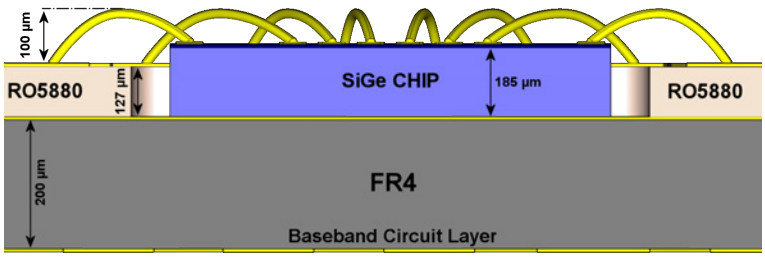

Figure 5.22: Side cut view of the SiGe Six-Port receiver chip in the cavity on the PCB.

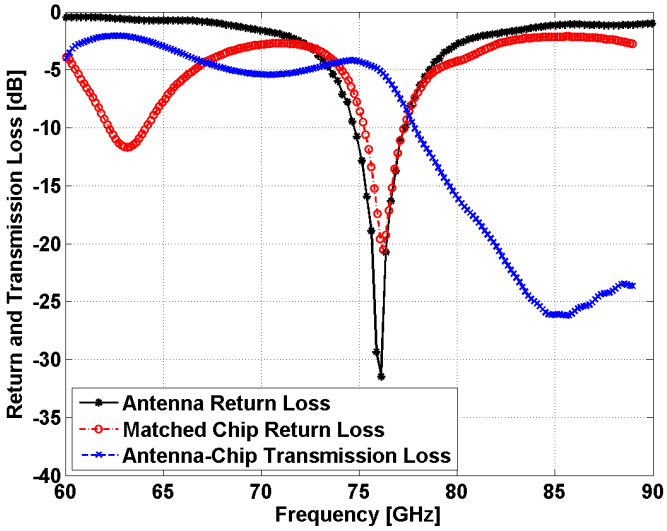

Figure 5.23: Return loss and transmission loss [62].
(Copyright 2012, IEEE)

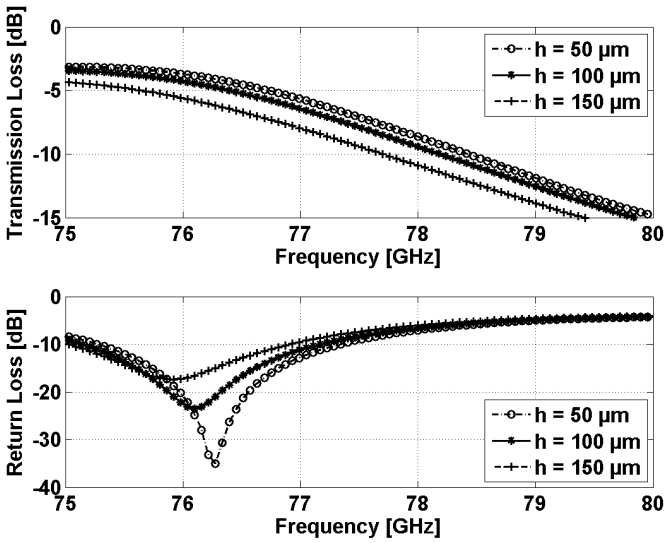

Figure 5.24: Effect of the bond height [62].
(Copyright 2012, IEEE)

5.6.5 Measurement Results

The SiGe chip has been bonded on the PCB which has been covered with a thick-gold metallization to ease the wedge-wedge bond placement. Bonds have been positioned with a semi-automatic bonder, keeping the bond-height within the tolerance range from 50 µm to 150 µm. Minor baseband-processing circuitry has been implemented on the backside of the PCB (Fig. 5.27) in order to differentially amplify the output signals from the chip (in respect to the reference voltages provided on the chip pads).

The amplified differential signals have been sent to a custom-made digital signal processing board. The acquired signals have been recorded and analyzed in a post-processing phase through MATLAB. The results are plotted in Fig. 5.25 where the four signals can be seen as well as the calculated DOA angle (lower part of Fig. 5.25).

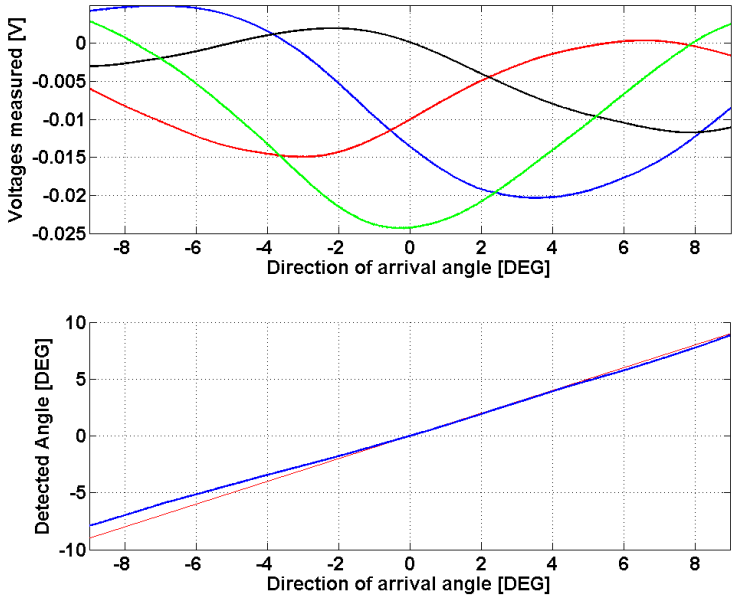

Figure 5.25: Measured voltages at the six-port and detected angle [62].

The setup has been tested with a dummy radiating source formed by a WR10 waveguide horn antenna (W band) with 23 dBi gain connected to a passive frequency trippler fed at IF by the PNA-X vector network analyzer from Agilent ($f_{IF} = 25.66$ GHz@ +16 dBm). The maximum output power from the trippler at 77 GHz is approximately -10 dBm.

A slight measurement error can be noticed for negative DOA angles smaller than -4 DEG. This is due to the drop of the four differential signal voltages for those negative angles. Since the dummy reference source features a highly focused radiation pattern (23 dBi gain horn antenna) the measurement presents errors as soon as the DOA detector setup is not within the -3 dB main radiation lobe (thus, explaining the differential voltage drop of all chip outputs).

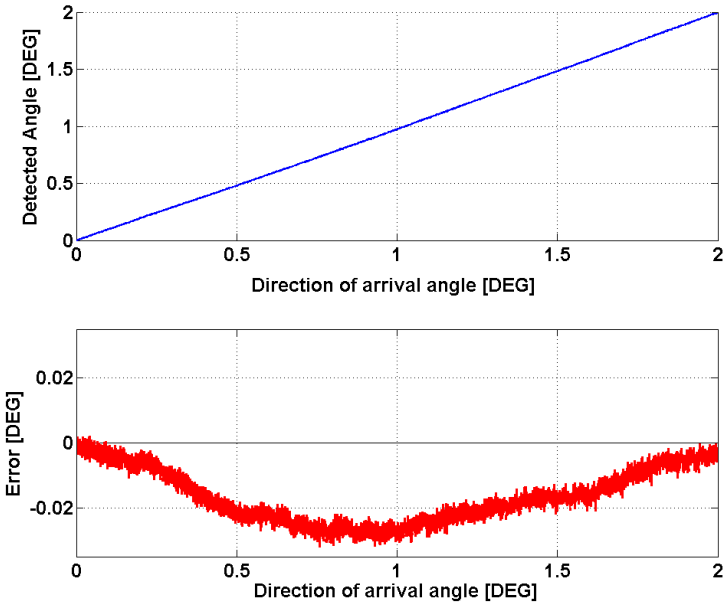

Figure 5.26: Detected DOA angle and measurement error [62].

To better show the accuracy of the presented system a plot of the DOA angle from 0 to 2 DEG is shown in Fig. 5.26. The system response is extremely linear even without any nonlinear calibration procedure. In fact, it has to be underlined that all measurement results presented are calibrated with a simple linear offset and scale factor correction. This ensures that the raw data can be properly evaluated.

The error plotted in the lower part of Fig. 5.26 shows the reproducible nonlinearity of the measurement. As can be noticed from Fig. 5.26, the uncalibrated system error reaches a maximum of 0.025 DEG.

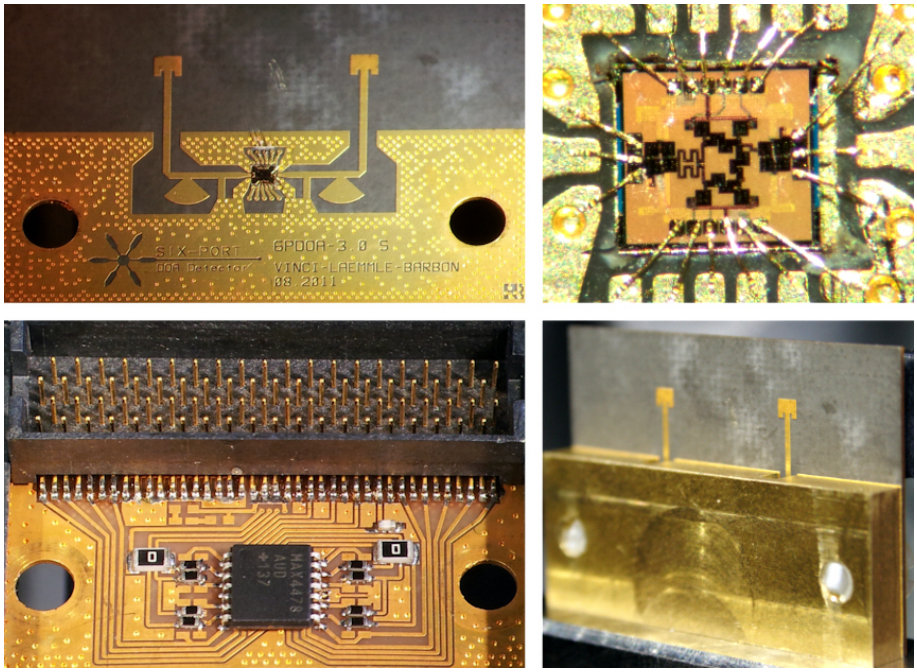

Figure 5.27: Photo of the manufactured hardware prototype [62].

6 The Dual Six-Port Concept

As mentioned in chapter 5, section 5.2 the Six-Port based DOA detector presents ambiguity issues. Depending on the distance between the two receiving antennas at which the phase difference is measured, a quasi-periodical repetition of the detected angle is present as an output. The system is not able to distinguish different angles of arrival whenever the corresponding phase difference exceeds $\pm\pi$ RAD. By reducing the distance between the receiving antennas it is possible to increase the ambiguity-free period and increase the observable angle of incidence. Though, by doing so the detection accuracy decreases since the whole phase difference is mapped onto a wider angle range. On the other hand, increasing the distance between the two antennas shrinks the angle detection range in which no ambiguity occurs and increases the detection accuracy.

The dual Six-Port concept merges these two design strategies keeping the positive side of each configuration and compensating the disadvantages of each other [63–65]. Two parallel Six-Port systems, Six-Port 1 and Six-Port 2, with two input antenna pairs having different relative distance d_1 and d_2 (such that $d_2 = q \cdot d_1$ with $q \in \mathbb{R}$) are connected to one central signal processing unit that analyzes the angles θ_1 and θ_2 detected by Six-Port 1 and Six-Port 2

$$\theta_i = \sin^{-1}\left(\rho_i \, \Delta\phi_i\right), \tag{6.1}$$

$$\rho_i = \frac{c}{f \, d_i \, 2\pi} \quad \text{with } i \in \{1, 2\}, \tag{6.2}$$

where $\Delta\phi_1$ and $\Delta\phi_2$ are the phase differences detected by the Six-Port receivers between the signals at the antenna pairs and ρ_1, ρ_2 are normalizing coefficients that depend on the speed of light c, the distances d_1 and d_2 between the antennas and the frequency f of the detected signal. By making use of the difference function

$$\Delta\theta = \theta_2 - \theta_1, \tag{6.3}$$

between the two detected angles θ_1 and θ_2, it is possible to map the complete angle of incidence range without ambiguity. $\Delta\theta$ leads to the cancellation of the ambiguity in phase with the help of an initial calibration procedure. This calibration will be explained in the next paragraphs. Within a small range around an incident angle of zero, the two detected angles have a quasi-linear period $P[\theta_i]$ (with $i \in \{1, 2\}$) determined by the ratio between the wavelength λ and the distances d_1 and d_2 respectively (6.4).

$$P[\theta_i] = \frac{\lambda\ 360\,\text{DEG}}{2\pi\ d_i} \quad \text{with } i=\{1,\ 2\} \tag{6.4}$$

For large incident angles the detected values θ_1 and θ_2 become highly non-linear changing the periodicity ratio. The nonlinear behavior derives from the trigonometric dependency of the detected phase difference to the DOA angle (sinusoidal dependency). For every incident angle the system calculates the difference function $\Delta\theta$ between the two detected angles. $\Delta\theta$ is a function with a period $P[\Delta\theta]$ that depends on the ratio between d_1 and d_2. By choosing an appropriate factor q such that the period is $P[\Delta\theta] > \theta_{or}$ (θ_{or} is the observation angle range) the function $\Delta\theta$ can be used to map the angle of incidence range that needs to be monitored with no ambiguity.

An example will illustrate the above introduced concept. A DOA detection of a Continuous Wave (CW) signal with a frequency of 24 GHz has to be performed ($\lambda = 12.49\,\text{mm}$). By having $d_1 = 18\,\text{mm}$ and using a factor $q = 3.33$, results in $d_2 = 59.94\,\text{mm}$. With these values non-ambiguous periods $P[\theta_1]$ and $P[\theta_2]$ for the detected angles θ_1 and θ_2 can be calculated as:

$$P[\theta_1] = \frac{12.5\,\text{mm}\ 360\,\text{DEG}}{2\pi\ 18\,\text{mm}} \approx 40\,\text{DEG} \quad -20 < \theta_1 < +20, \tag{6.5}$$

$$P[\theta_2] = \frac{12.5\,\text{mm}\ 360\,\text{DEG}}{2\pi\ 59.94\,\text{mm}} \approx 12\,\text{DEG} \quad -6 < \theta_2 < +6. \tag{6.6}$$

The non-ambiguous period of the difference function is larger than the one of the detected angles alone. Referring to the above stated example, since for a wider range of incident angles periodicity changes due to sinusoidal distortion of θ_1 and θ_2, the wanted condition $P[\Delta\theta] > \theta_{or}$ is reached. In this case to monitor an incident angle from -80 to $80\,\text{DEG}$ ($\theta_{or} = 160\,\text{DEG}$) the ratio $q = 3.33$ satisfies the above stated condition ($P[\Delta\theta] > 160\,\text{DEG}$).

In the observation range the difference function $\Delta\theta$ defines sectors in which the value of the function is constant. These sectors offer the possibility to uniquely identify a subsection of the observation range. In these sectors a known offset can be added to the measured value of θ_2 to determine the actual DOA angle. In other words, by analyzing $\Delta\theta$ the actual period can be determined leading to the cancellation of the ambiguity in phase by a compensating offset. The offset can be mapped "a-priori" in the system during a calibration procedure.

To prove the above described theory two dual Six-Port receiver demonstrators have been developed: the first working at a frequency of 24 GHz based on microstrip technology on an RF PCB and the second one working at a frequency of 77 GHz featuring a chip integrated Six-Port receiver in Silicon-Germanium (SiGe) semiconductor technology.

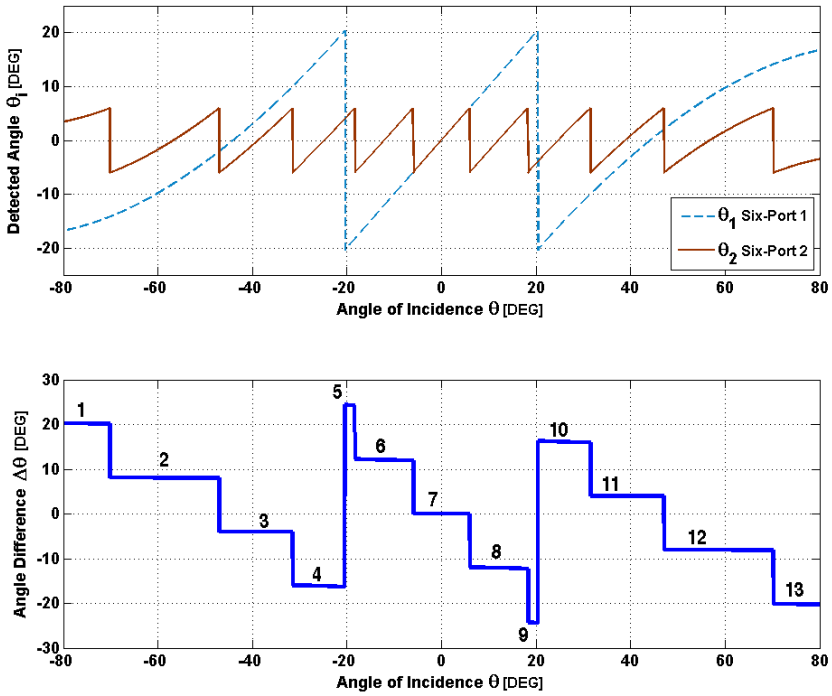

Figure 6.1: Simulation results for the dual Six-Port receiver at 24 GHz [64].

6.1 24 GHz Dual Six-Port DOA Detector

A functional block overview of the complete hardware system is given in Fig. 6.2. The proposed DOA detector is based on two Six-Port receivers with one antenna pair for each receiver (a total of four receiving antennas for the complete system). Since the Six-Port receiver is a purely passive device, a poor dynamic range is a downturn of this concept. Therefore, a double LNA stage is used to amplify the signals coming from the four input antennas for an overall gain of 50 dB with a maximum input power of -5 dBm. These amplified signals are then fed to the Six-Port networks where the additive superposition occurs.

The used power detector is based on the GaAs Schottky diode (*MZBD-9161*) with a dynamic range from -55 dBm to +20 dBm as the one presented in section 4.2.4. Following the link budget table in Fig. 6.3, it is possible to derive the input dynamic range. The system has a dynamic range of 89 dB from -94 dBm up to -5 dBm.

The four outputs of each Six-Port circuit are connected to power detectors that deliver a voltage linearly related to the power of the RF signal at the monitored output port. The detector voltages are amplified by low-noise rail-to-rail baseband amplifiers and fed to ADCs. The ADCs are synchronously triggered to acquire the eight voltages simultaneously. In this way a correct proportionality between the signals is guaranteed, even if the phase difference between the two input signals is rapidly changing.

A feedback from the digital domain to the analog front-end is also provided. DACs serve as an interface to calibrate the RF power at the LNA stages to avoid an overdrive of the RF components and detectors. The DACs also control the gain of the baseband amplifiers to deliver voltage signals at the ADCs within a proper input scale. The data is then processed by an ALTERA Cyclone II (2C35) FPGA board and sent to a computer via an Ethernet connection. Data is finally processed and analyzed by a MATLAB based software that delivers the angle of incidence of the incoming signal with respect to the axis on which the receiving antennas are aligned. Baseband signal conditioning as well as the analog-to-digital conversion (and vice-versa) is described in chapter 5 throughout sections 5.5.2 and 5.5.3.

The demonstrator is built on a stack of multilayer PCB. A total of two main boards have been designed to integrate the whole subsystems. The first board comprises a 3-layer stack RF PCB structure. The top-layer integrates the microwave passive structures, antennas as well as RF front-ends. A CNC-

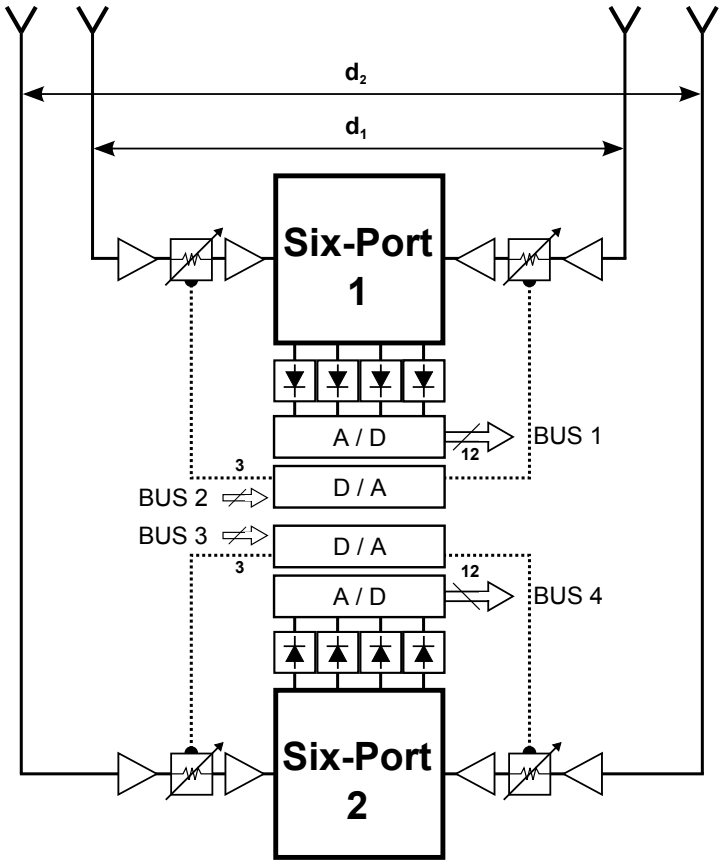

Figure 6.2: Dual Six-Port system overview [63].

machined brass metal enclosure on the front serves as an RF shield to avoid undesired coupling of the incoming signals to the microstrip circuit structures. The only non-shielded elements are the four patch antennas. The box cavities are filled with graphite foam absorber material to avoid cavity resonances. The second layer serves as an RF ground for the microstrip structures. A third layer routes the analog signals coming from the baseband amplifiers to a header connector. RF substrate used between the RF layer and ground is a 0.2 mm thick Rogers 4003C hydrocarbon ceramic, with a dielectric constant $\epsilon_r = 3.38$.

On a second board the baseband signal processing and the digital circuitry, bus connections and power supplies have been integrated.

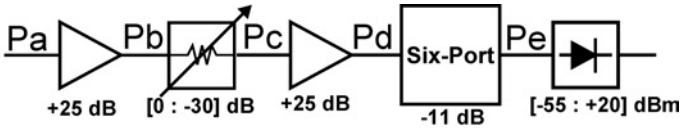

	Pa	Pb	Pc	Pd	Pe
MAX	-5 dBm	+20 dBm	-5 dBm	+20 dBm	+9 dBm
min	-94 dBm	-69 dBm	-69 dBm	-44 dBm	-55dBm
Opt	-39 dBm	-14 dBm	-14 dBm	+11 dBm	0 dBm

Figure 6.3: Link budget of the dual Six-Port DOA detector [64].

6.1.1 Digital Signal Processing and Initial Calibration

Some considerations about the representation accuracy within the digital domain have to be made. The eight output channels from the two Six-Port receivers are digitized in a 12 bit format on a 5 V scale. Thus, a resolution of 1.22 mV on the Least Significant Bit (LSB) can be reached. The ideal representation for the detected DOA angle values within the digital signal processing unit is a fixed-point 20 bit format, with 9 bit signed integer and 11 bit decimal parts. This gives a maximum angle value of 256 DEG including one bit for the sign for the integer part and a minimum representable value of $0.5\,\text{DEG} \cdot 10^{-3}$.

The initial calibration procedure works as follows: an automated setup, formed by the DOA angle detector device and a dummy radiating source, rotates the DOA detector around its axis while a reference signal is emitted from the dummy source. In this way a full DOA angle sweep is given as an input to the system which detects the incoming signal and records the measured values of θ_2 as well as the difference function $\Delta\theta$ as system-specific calibration curves.

For this purpose two techniques have been implemented: Polynomial Function Approximation (PFA) and Direct Digital Sampling (DDS). The first technique acquires the whole θ_2 angle sweep and evaluates for each section, described by a different value of $\Delta\theta$, the function with a polynomial approximation technique. Hence, 13 functions are fitted with polynomial coefficients with a 5^{th} order approximation (6.7).

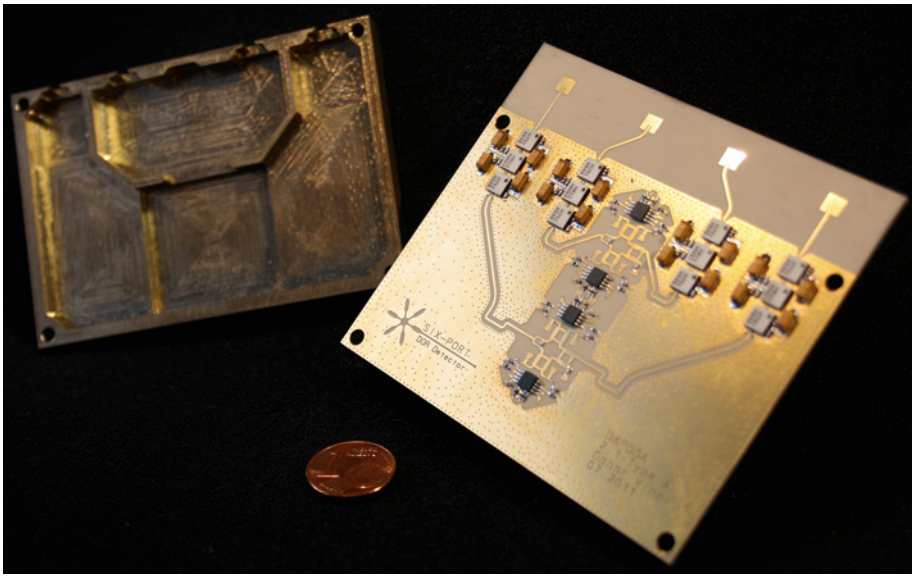

Figure 6.4: Photo of the dual Six-Port front-end demonstrator at 24 GHz [64]. (Copyright 2012, IEEE)

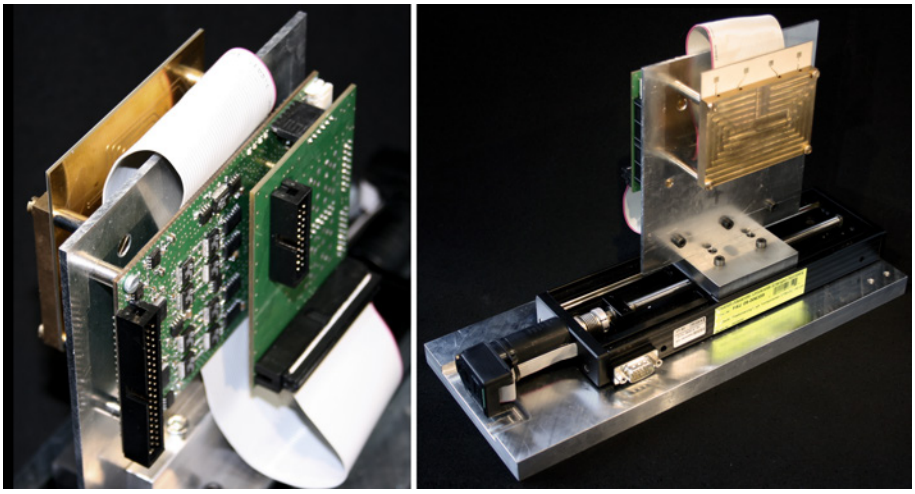

Figure 6.5: Photo of the complete system mounted on a high-precision positioning stage [64]. (Copyright 2012, IEEE)

$$\theta_{detect_i} = \sum_{m=0}^{5} c[m]_i \, \theta_{2_i}^m \quad \text{with } i=\{1,...,13\} \tag{6.7}$$

After the fitting process only 6 polynomial coefficients $c[0, ..., 5]$ per curve and $\Delta\theta$ step values need to be stored as a calibration result. This technique is very efficient in terms of low memory requirements, but needs higher effort in the reconstruction technique during operation, since for each measurement sample a 5^{th} order polynomial fitting has to be executed. An even bigger problem arises when storing the extracted coefficients in a digital memory system. By quantizing the coefficients with 9 bits integer and 11 bits decimal, a non-neglectable error is introduced in the reconstruction process since all coefficients smaller than the allowed resolution are approximated to zero. The reconstruction error is therefore as plotted in Fig. 6.6.

The second data processing strategy (DDS) requires the system to store the acquired curves of θ_2 and $\Delta\theta$ sample per sample into memory. In this case, no polynomial evaluation is done. The angle functions are store as they are into memory. This implies the system to sample the curves at least at the same angle resolution as the one representable by the digital format chosen ($0.5\,\text{DEG} \cdot 10^{-3}$). For a calibration of a desired observation range from -80 DEG to +80 DEG it is therefore necessary to store 320000 samples with a depth of 20 bit each, resulting in a calibration matrix of 6.4 Mbit.

This solution requires much more memory for the calibration matrix if compared to the first solution proposed. On the other hand, it delivers a much smaller detection error that is three orders of magnitude lower compared to that of the PFA method (Fig. 6.6) with the same bit-depth representation. Furthermore, the memory requirement for this strategy is not a problem for modern low-cost digital systems (less than one megabyte is required to store the calibration data). The DDS strategy is therefore preferred due to better results and lower complexity.

6.1.2 Measurement Results

After a calibration routine, a measurement of the DOA angle on the entire observation range has been done (from -80 to 80 DEG). A reference Voltage Controlled Oscillator (VCO) with a CW 24 GHz, +9 dBm output connected to a standard 10 dBi gain horn antenna has been used as a radiating source. Due to lower signal-to-noise ratio and different system nonidealities the detected angles θ_1 and θ_2 present nonlinearities and superimposed noise.

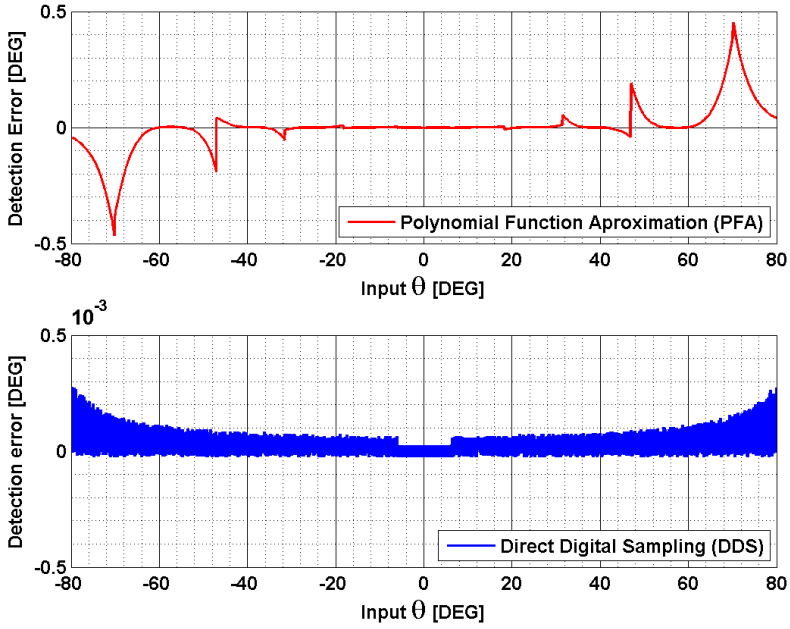

Figure 6.6: Angle detection error in the Polynomial Function Approximation technique and in the Direct Digital Sampling technique [63]. (Copyright 2011, IEEE)

Nevertheless, these measurement results show that the difference function still delivers easily detectable and non-ambiguous step values that can be used to eliminate the ambiguity problem. A direct comparison with the simulation results in Fig. 6.1 demonstrates the correctness of the theory and the capability of the proposed system.

6.2 77 GHz Dual Six-Port DOA Detector

As mentioned before at the beginning of this chapter also a dual Six-Port DOA detector demonstrator at 77 GHz has been build and is hereby presented. For this system, two integrated Six-Port receivers as the ones described in chapter 5 section 5.6 are implemented in one system with two antenna pairs having different relative distances d_1 and d_2 such that $d_2 = q \cdot d_1$ (as can be seen in Fig. 6.8).

The two Six-Port receivers deliver the detected DOA angles θ_1 and θ_2, re-

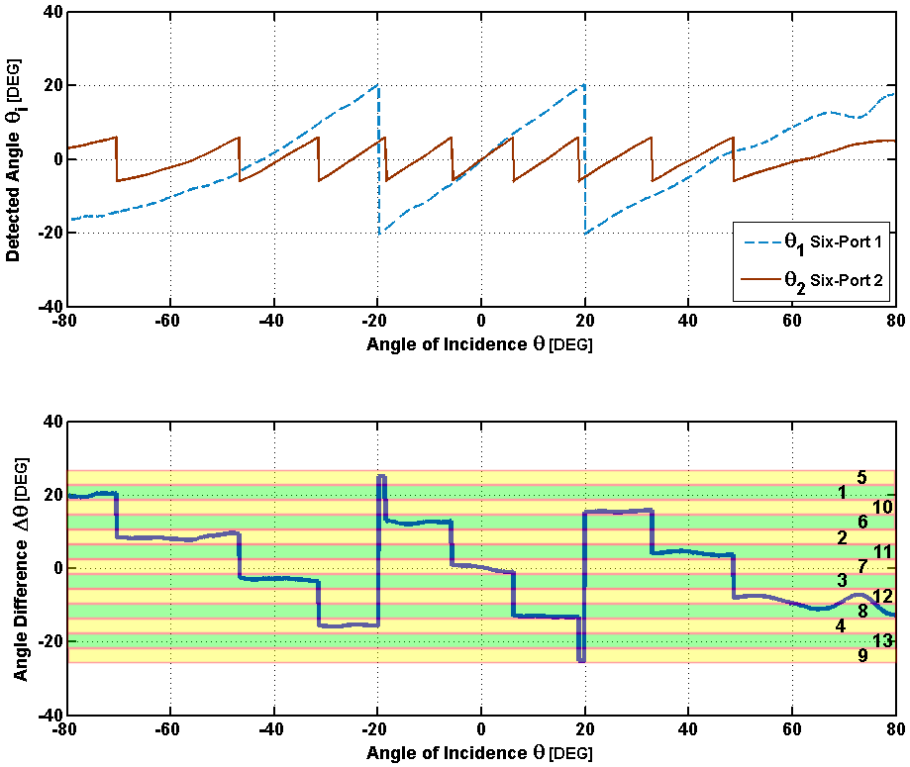

Figure 6.7: Measurement results for the dual Six-Port receiver at 24 GHz [64]. (Copyright 2012, IEEE)

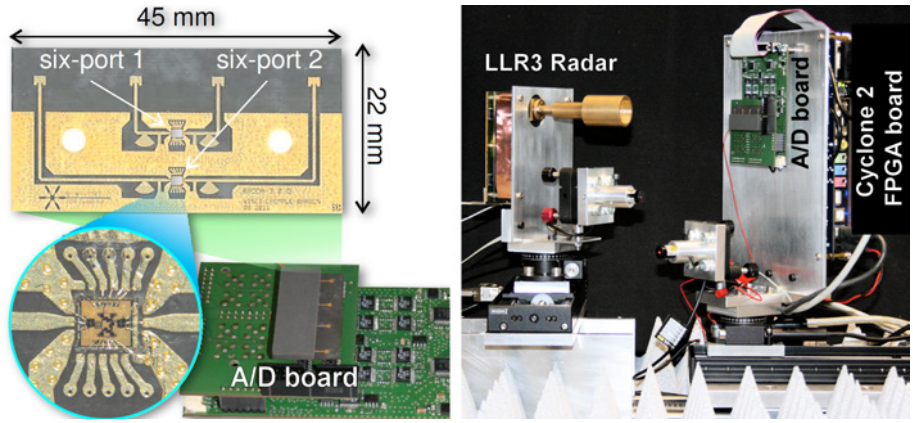

Figure 6.8: Complete hardware setup of the dual Six-Port at 77 GHz with PCB stack assembly [65]. (Copyright 2012, IEEE)

spectively. Having a distance d_1 = 11.2 mm between the first receiving antenna pair and q = 3.33 leads to d_2 = 37.2 mm between the second receiving antenna pair. Following eq. (6.4) the non-ambiguous observation ranges can be calculated:

$$\theta_{obs1} = \frac{3.89\,\text{mm}\ 360\,\text{DEG}}{2\pi\ 11.2\,\text{mm}} \approx 20\,\text{DEG} \quad -10 < \theta_1 < +10, \tag{6.8}$$

$$\theta_{obs2} = \frac{3.89\,\text{mm}\ 360\,\text{DEG}}{2\pi\ 37.2\,\text{mm}} \approx 6\,\text{DEG} \quad -3 < \theta_2 < +3. \tag{6.9}$$

The difference function between the two detected angles is then $\Delta\theta = \theta_2 - \theta_1$. If the ratio q is chosen as a non-integer number (here $q = 3.33$), the resulting ambiguity free range of the difference function will be larger than the ambiguity free observation ranges of the single Six-Port receivers. $\Delta\theta$ can therefore be used to uniquely identify the DOA angle within a wide observation range, thus leading to the cancellation of the ambiguity in phase. In Fig. 6.9 $\Delta\theta$ is plotted defining non-ambiguous step-like sections within the observation range. For each section, a static offset is defined and added to θ_2 (or θ_1) to derive the final angle of arrival.

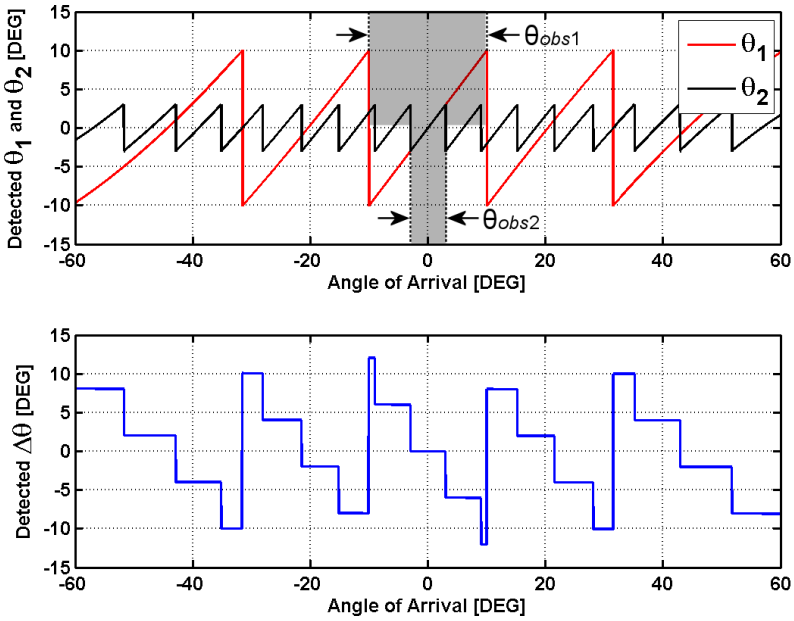

Figure 6.9: Simulated dual Six-Port angle detection at 77 GHz [65].

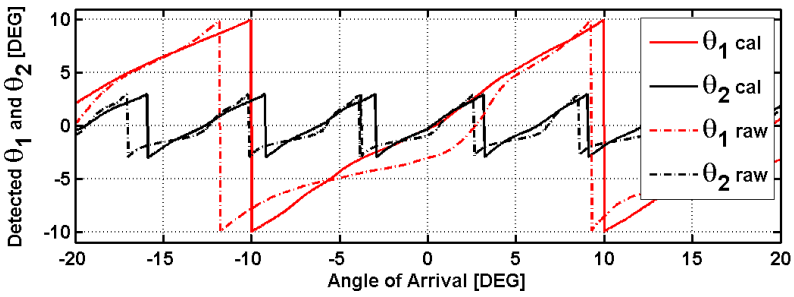

Figure 6.10: Linearization effect on the detected angle for the demonstrator at 77 GHz [65]. (Copyright 2012, IEEE)

The system consists of a stacked PCB assembly (Fig. 6.8). Each board represents a subsystem unit to detect, convert, acquire and process the signals. Starting from the millimeter-wave receiver antennas, RF front-end and analog baseband, the system processes the signals through a dedicated ADC board (section 5.5.3). Finally, the digital signal processing is implemented in an Altera Cyclone 2 FPGA. The data is then streamed to a computer.

The integrated receivers are presented in section 5.6.1, fabricated in SiGe bipolar technology and include two input LNAs, a broadband passive Six-Port network and four high-responsiveness power detectors. As mentioned in section 5.6.1, since the Six-Port receivers are based on the additive self-mixing effect of the two input signals, the chips do not include an oscillator.

An RF board hosts the two SiGe Six-Port receiver chips as well as the antennas and matching networks. The Six-Port receivers are mounted in chip cavities fabricated on a 127 µm thick Rogers RT Duroid 5880 glass microfiber reinforced PTFE laminate ($\epsilon_r = 2.2$, $\tan\delta = 0.0009$). Microstrip lines connect the patch antennas fabricated on the same substrate. Matching structures have been implemented, as described in section 5.6. A CNC-machined metal shielding covers the chips to prevent unwanted coupling. The shield is coated with an Eccosorb BSR-U magnetically loaded silicone rubber film to prevent cavity resonances.

The calibration of the system is essential to obtain feasible results. The Six-Port receivers present phase measurement errors due to length difference of the bond wires connecting the chips and non-idealities of the quadrature hybrid couplers and microstrips in the SiGe chip interferometric structures. Furthermore, the detectors present different responses to the same input power, although they are integrated on the same chip die. All these effects contribute to errors in the detected DOA angle. A calibration software code

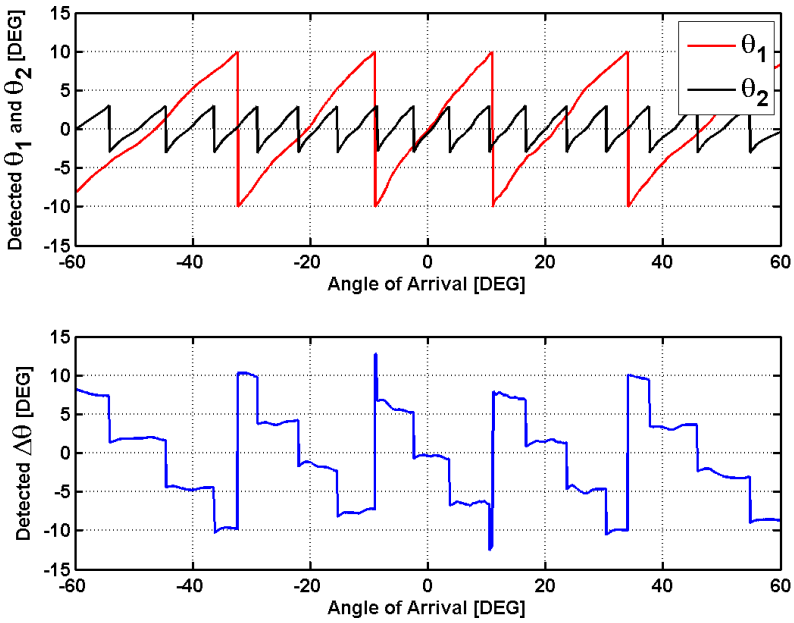

Figure 6.11: Measured dual Six-Port DOA detection with the demonstrator at 77 GHz [65]. (Copyright 2012, IEEE)

has been implemented to initialize a calibration procedure by rotating the detector setup with a high-precision rotary stage and extract the linear calibration parameters. The eight voltage signals from the dual Six-Port front-end have then been corrected. The result of the calibration is plotted in Fig. 6.10.

6.2.1 Measurement Results

After a calibration routine, a measurement of the DOA angle on the entire observation range has been performed (from -60 to 60 DEG). An *LRR3* Automotive Radar from Bosch GmbH has been used as a radiating source, featuring an *ATLAS* Radar chip from Infineon AG (Fig. 6.8). The results are plotted in Fig. 6.11. Due to lower signal-to-noise ratio and different system non-idealities the detected angles θ_1 and θ_2 present nonlinearities and superimposed noise. Nevertheless, these measurement results show that the difference function still delivers easily detectable and non ambiguous step values that can be used to eliminate the ambiguity problem.

A direct comparison with the simulation results in Fig. 6.9 demonstrates

the correctness of the theory and the capability of the proposed system. The overall setup is formed by a stack of subsystem boards offering a compact form-factor and an easily controllable prototype suitable for high-resolution misalignment angle detection.

6.3 Frequency Dependency on the DOA Detection

The dual Six-Port concept allows an ambiguity free DOA detection within a wide observation range that is of great advantage for certain applications. Nevertheless, results presented so far refer to a DOA detection of a signal source radiating a CW signal at a single frequency. For several application scenarios this condition cannot always be satisfied. Detection and tracking of sources with variable signal frequency is of great interest. For instance, detection and calibration of misalignment angle of automotive radars can be performed by evaluating the FMCW signal without forcing the radar device to transmit a single frequency CW signal for calibration purposes only. Another application scenario involves the detection and tracking of non-cooperative targets, for instance hostile radar detection with unknown frequency of operation (at least within the frequency range of the Six-Port based DOA detector). In the following, an overview of the dual Six-Port DOA detector is given emphasizing the effect of the received signal frequency on the DOA detection accuracy.

The detected DOA angles θ_1 and θ_2 are dependent on the frequency of the incoming signal. The dependency is directly expressed by the normalizing coefficients ρ_1 and ρ_2 as evidenced in eq. (6.2). Furthermore, for a constant DOA angle even the detected phase differences $\Delta\phi_1$ and $\Delta\phi_2$ change as the frequency of the detected signal changes. In other words, $\Delta\phi_i \propto f$ while $\rho_i \propto 1/f$ for $i \in \{1, 2\}$. By knowing the detected signal frequency, the DOA angles θ_1 and θ_2 can always be exactly calculated and would be therefore independent from f. Assuming that the frequency of the detected signal varies and is not known to the DOA detector, a variation of the detected DOA angles θ_1 and θ_2 will take place. The frequency variation will be hereby defined as

$$\Delta f = f_{rx} - f, \tag{6.10}$$

with f_{rx} as the actual frequency of the detected signal that deviates from the expected system frequency f for which the detector has been calibrated. In eq. (6.1) the normalizing coefficients ρ_1 and ρ_2 are therefore constant and the variation of the DOA angles θ_1 and θ_2 is due to the change in the phase

differences $\Delta\phi_1$ and $\Delta\phi_2$. This variation can be expressed relatively to the frequency shift and leads to the calculation of the detected DOA angle errors γ_1 and γ_2 as follows:

$$\frac{\Delta f}{f} = \frac{\Delta\phi_{irx} - \Delta\phi_i}{\Delta\phi_i} = \delta_i, \tag{6.11}$$

$$\gamma_i = \sin^{-1}(\rho_i\,\delta_i) \quad \text{with } i \in \{1, 2\}, \tag{6.12}$$

where $\Delta\phi_{irx}$ is the detected phase difference at the antenna pair for an incoming signal at the frequency f_{rx}. The detected DOA angle errors γ_1 and γ_2 are not only dependent on the relative frequency variation but also on the normalization factors ρ_1 and ρ_2. Since $\rho_i \propto 1/d_i$ for a large distance d between the receiving antenna pair the detected DOA angle error γ will be small, whereas for a short distance d, γ will be large. This drawback of a short distance d between the receiving antennas is in contrast to the benefit offered by a larger ambiguity free range. This explains why a shorter distance d between the receiving antennas is not necessarily an advantage for a Six-Port based DOA detector. Therefore, the dual Six-Port concept offers not only a solution to the ambiguity problem but also a robust detection of signal sources with variable signal frequency. These conclusions are hereby validated by measurement results (Fig. 6.13 and Fig. 6.14).

6.4 Dual Six-Port Calibration

To perform an accurate DOA detection, the system described above has to be calibrated. The calibration procedure consists of three steps [66].

6.4.1 DOA Angle Sweep

First of all, given a reference CW signal with a stable single frequency of operation and a stable output power, a reference DOA angle sweep is performed with the dual Six-Port receiver. The setup is rotated with a high-precision rotary stage while being illuminated by a radiating antenna. During this procedure, the baseband signals from the Six-Port receivers are normalized and eventual DC offsets are removed. Furthermore, the detected phase values $\Delta\phi_1$ and $\Delta\phi_2$ are calculated and recorded.

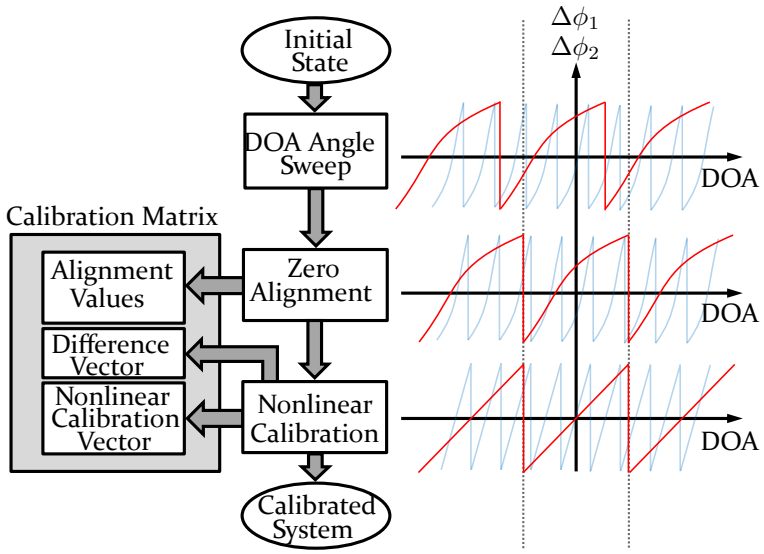

Figure 6.12: Complete calibration routine for the dual Six-Port DOA detector [66]. (Copyright 2013, IEEE)

6.4.2 Reference Zero Alignment

An inherent phase shift between the two Six-Port modules due to non-idealities in the manufacturing process brings a shift in the measured phase differences $\Delta\phi_1$ and $\Delta\phi_2$ between the two systems. Therefore, the two Six-Port receivers must be both aligned to a reference direction. This is done by searching the symmetrical distance of the phase wraps from the reference zero position (automatic phase wrap search algorithm). During this procedure the alignment values are stored.

6.4.3 Nonlinear Calibration

Furthermore, nonlinearities within the Six-Port receivers must be compensated. An ideal phase function (perfectly linear sawtooth function) is subtracted from the measured phase values generating a nonlinear calibration vector which is saved together with the alignment values in a calibration matrix (Fig. 6.12). The calibrated phase values are now used to calculate the DOA angles θ_1 and θ_2 which are used to generate the difference vector $\Delta\theta = \theta_2 - \theta_1$. This vector enables the ambiguity free detection of the dual Six-Port DOA receiver.

6.4.4 Evaluation of the DOA Detection Error

To demonstrate the conclusions stated above, the detection of an FMCW radiating source in the Industrial-Scientific-Medical (ISM) band at 24 GHz is hereby presented. As a test object emulating an FMCW radar an Agilent PSG E8267D vector signal generator has been used connected to a 20 dBi gain horn antenna.

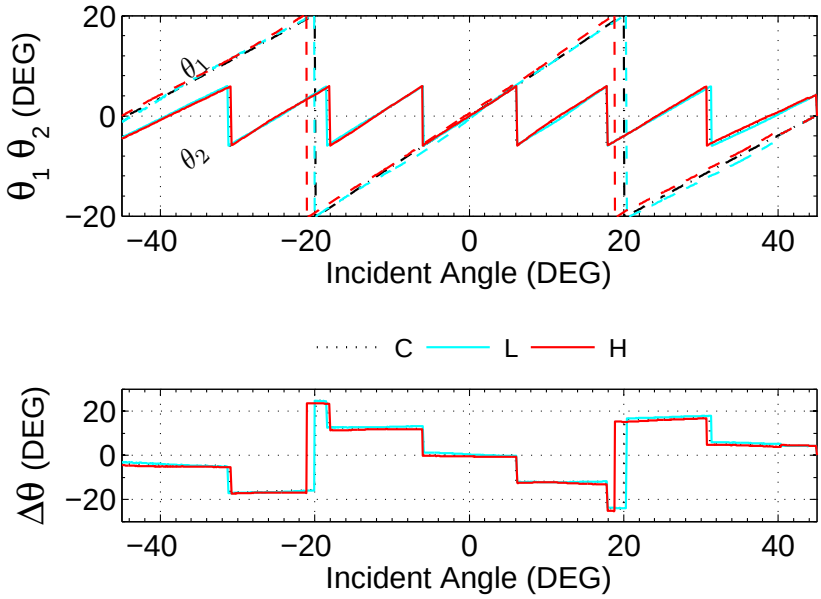

Figure 6.13: Detected DOA angles θ_1 and θ_2 and angle difference $\Delta\theta$ at lower (L = 24.000 GHz), center (C = 24.125 GHz) and higher (H = 24.250 GHz) frequency of the ISM band [66].

The band has a center frequency of 24.125 GHz and a width of 250 MHz. The output RF power has been set to -30 dBm and the radiating antenna has been placed at 2 m from the dual Six-Port DOA detector. The DOA angle has been mechanically swept from -45 to +45 DEG.

The dual Six-Port DOA detector has been calibrated at the center frequency. DOA angle detection has then been performed by letting the source sweep the complete 250 MHz band with an up-ramp time of 10 ms. The results (θ_1, θ_2 and $\Delta\theta$) are plotted in Fig. 6.13. The step values of $\Delta\theta$ present no

major changes due to the frequency sweep and can be still used to solve the ambiguity issue. As for θ_1 and θ_2, the minor DOA angle variations resulting from the frequency sweep are barely noticeable in Fig. 6.13.

Therefore, an error plot illustrating the detection errors γ_1 and γ_2 is also presented. From Fig. 6.14 it can be noticed that the detection error γ_1 is larger than γ_2 over the detection range, as described in eq. (6.12), thus confirming the theory stated above. Despite the large bandwidth of 250 MHz the angle detection error γ_2 is smaller than ± 0.5 DEG.

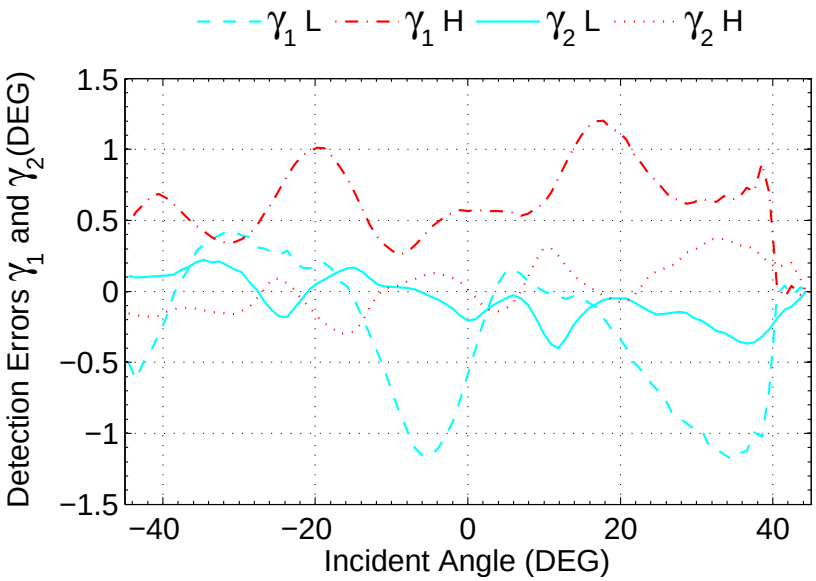

Figure 6.14: Detection errors γ_1 and γ_2 at lower band (L = 24.000 GHz) and higher band (H = 24.250 GHz) frequencies [66].

7 Ranging Techniques

7.1 The Radar Principle

RADAR stands for "RAdio Detection And Ranging" and identifies a basic ranging technique making use of the scattering and propagation properties of electromagnetic waves. Its function has been expanded since its first introduction just before the Second World War to include several other information besides ranging (such as speed measurement).

For a generic radar system, a microwave transmitter sends out a signal which is reflected by a target and then detected by a receiver. The reflection on the target delivers the ranging information. The distance to the target is determined in several ways, depending what type of radar technique is used.

Radars are nowadays used for civilian, military and scientific applications of several kinds. Further information can be found in graduate level textbooks [11] as well as in dedicated literature on the topic [67].

The field of radar technology has expanded tremendously in the last decades. The information delivered in this chapter serves only as an overview for the reader in order to better understand the ranging techniques that involve the Six-Port receiver. There is an overwhelming amount of literature on radar and generally the content is extensively specialized depending on the particular radar technique treated. A general overview will be hereby given.

7.2 Monostatic and Bistatic Radar

Radars can be grouped in two basic systems: the monostatic and the bistatic radar. In the monostatic radar the same antenna is used for both transmitting the signal and receiving the back-scattered wave from the target, while the bistatic radar uses two separate antennas [11]. Beside this first differ-

ence, several techniques have been implemented to perform many different measurements. A short overview is presented in the following paragraphs.

7.3 Pulse Radar

Pulse radars emit a short microwave impulse signal that hits the target and gets reflected back to the transmitter. The received signal is delayed with respect to the transmitted one depending on the Round-trip Time of Flight (RToF) of the signal to the target and back to the sensor. By measuring the flight time of the signal the distance to the target can be derived. However, since the measurement principle is based on time detection, such a technique cannot be used for short range measurements or high-precision distance detection, due to the relatively low accuracy in very short time interval measurements [11].

7.4 Doppler Radar

A Doppler radar makes use of the Doppler effect to determine the speed of a monitored object. The target moves with a speed v causing a Doppler frequency shift f_d of the back-scattered signal frequency f_s depending on v as described in eq. 7.1 [11]:

$$f_d = \pm \frac{2 f_s v}{c} \, . \tag{7.1}$$

By measuring f_d it is possible to determine the speed of the target. This gives highly accurate measurements of the target's velocity along the line of sight (LOS) of the radar (radial velocity with respect to the radar).

For an approaching target $f_d > 0$ while for a target moving away $f_d < 0$. This kind of radar architecture is very simple since it makes use of a monotone continuous wave signal. Furthermore, a high of isolation is not necessary between transmitter and receiver paths relaxing the design requirements [11].

It is important to state that the back-scattered signal of a pulse radar from a moving target is also affected by the Doppler shift. By combining a RToF measurement with a Doppler frequency shift measurement it is therefore possible to determine both range and velocity of a target. Such radar is known as a pulse-Doppler radar [11].

7.5 FMCW Radar

FMCW radars feature at the output a continuous microwave signal that is frequency-modulated, typically with a triangle shaped signal [68]. This internal reference signal is then mixed with the signal reflected from a target resulting in a baseband signal called the beat signal. Different modulation signals such as sine or sawtooth can also be implemented. Nevertheless, the triangle modulation is preferred since both distance and velocity of the target can be measured, taking advantage of the Doppler frequency shift caused by the movement of the target itself. Due to the frequency modulation, the time delay can be measured as a frequency difference between the reference and the received frequency ramp [69]. Additionally, the speed of the moving target causes a shift in frequency of the received signal due to the Doppler effect. The baseband down-converted signal provides this information that can be analyzed with the use of signal processing.

In order to reach a high spatial resolution on short distances, very steep frequency ramps are generated [70] from the VCO source of the radar device. This allows the system to generate a larger frequency shift between the reference signal and the reflected signal, even for very small distance detection. That is why the sweep bandwidth determines the spatial resolution of FMCW radars [71].

Nevertheless, VCOs are either optimized for a CW output at a stable resonant frequency with a long time constant of the resonating circuit (so to guarantee a precise carrier frequency generation), or for fast tuning through the control voltage. For a very precise distance measurement with FMCW radars a trade-off between these two design strategies has to be reached [72] leading therefore to a non-stable output frequency and evidencing the output nonlinearity of the oscillator source. A static calibration of the VCO nonlinearity can be performed to compensate these effects [73], but this method cannot correct dynamic nonlinearities of the VCO (for instance, phase noise) [74, 75]. These dynamic processes can influence the performance of FMCW radar dramatically.

An additional phase evaluation has been proposed as an additional measurement technique for FMCW radars in order to increase the measurement accuracy. Being able to detect a phase shift of the back-scattered signal with respect to an internal reference can increase the spatial resolution of the radar device. A coarse evaluation is performed with the standard FMCW technique by means of a frequency shift measurement and consequently, through the frequency ramp steepness. A phase shift evaluation al-

lows a higher resolution measurement within the period of the wavelength used for the phase shift measurement. Alternatively to the phase evaluation, the centroid of the target peak in frequency domain can also enhance the FMCW radar's resolution to sub-wavelength accuracy.

7.6 The Six-Port Receiver as a Radar

Beside the just introduced radar techniques usually employed with multiplicative mixer based receivers, the Six-Port receiver can be used as an alternative. The peculiarities of the Six-Port can be an advantage for certain applications. Especially the excellent phase discrimination offered by this alternative microwave receiver can lead to high accuracy distance measurements [72]. In the next chapter, the Six-Port receiver is introduced for high resolution radar applications.

8 Ranging with the Six-Port Receiver

In this chapter a Six-Port receiver based technique for a high resolution radar applications is presented. This idea has been already used for similar purposes [76–92] although, a significantly different approach is hereby proposed. The technique presented is based on a phase measurement in the radio frequency domain with the additive homodyne receiver principle of the Six-Port receiver (the reader is addressed to sections 3.2 and 3.3 as well as chapter 4).

For common FMCW radar devices (as expressed in section 7.5) a sub-wavelength resolution is realized by phase measurements in the baseband (at low frequencies) leading to tolerances stimulated by noise, nonlinear effects of the mixing components and digitizing errors, like the quantization error. Furthermore, the resolution of such radars is correlated with the used bandwidth being limited by the standardization of the frequency spectrum.

The Six-Port receiver based technique presented in this work reduces these tolerances by a phase analysis in the radio frequency domain and offers high resolution for narrow-band signals. Normally this leads to ambiguities if distances of more than half a wavelength are measured (same effect as the ambiguity issue for DOA applications, presented in section 5.2). Further on in this chapter a solution to this problem will be presented making use of two or more signals with non-integer multiples of their carrier frequencies and comparing the observed phase differences of these signals to each other (section 8.2). This allows to measure distances of several wavelengths with sub-wavelength accuracy and ultra-low tolerances.

As mentioned above, in literature about high-resolution ranging, several valid techniques have been proposed. In [93–95] high-precision local positioning sensors and ranging methods are presented and in [96, 97] a high-resolution ranging method by means of a Six-Port interferometer is described to achieve sub-millimeter accuracy though leaving the ambiguity problem (see section 5.2 and 8.2) unsolved. Furthermore, [84] refers to a distance

measurement sensor technique that uses a Six-Port interferometer. Nevertheless, the mentioned technique in [84] works with one fixed-frequency reference signal whilst the hereby proposed solution works with CW signals as well as FMCW signals or Stepped Frequency Continuous Wave (SFCW).

In the proposed Six-Port based distance measurement radar a reference signal generated from a source is sent to an antenna pointing towards a target. An electromagnetic wave propagates to the target and is then backscattered. The reflected wave is therefore received by the system and sent to the Six-Port receiver that compares the relative phase difference between the transmit signal generated by the source and the signal reflected by the target. When the distance between the radar and the target does not vary, the relative phase difference will also not change. As soon as the distance changes a variation in the relative phase difference can by measured with the Six-Port receiver. The concept works at arbitrary frequencies with different modulation schemes generated by the source since a CW signal can be used as well as FMCW or SFCW.

8.1 The Six-Port Radar System

To perform distance measurements and ranging a CW monostatic radar with interferometric evaluation is hereby introduced. The radar is based on the Six-Port receiver network introduced in chapter 4 (homodyne receiver with additive mixing). The Six-Port performs a relative phase measurement between the received signal from the antenna and a reference signal derived through a directional coupler from a VCO source generating a 24 GHz CW signal. The RX and TX paths are separated through a circulator or a coupler installed directly behind the antenna. In the demonstrator hereby presented, a 20 dBi gain rectangular horn antenna has been used. The received signal is amplified by an LNA and a variable attenuator chain to guarantee that the amplitude of the input signal $\underline{P_2}$ at the second port of the Six-Port receiver is comparable to the amplitude of the reference signal $\underline{P_1}$ at the first input port. This will ensure maximum phase resolution. In the demonstrator an HMC751LC4 LNA and a HMC812LC4 attenuator by Hittite have been used.

In the proposed radar system, the four microwave output signals $\underline{P_3}$, $\underline{P_4}$, $\underline{P_5}$ and $\underline{P_6}$ of the Six-Port interferometer structure are converted into baseband voltages by diode-based power detectors, as described in chapter 4. The detector structure is based on an input matching network, a Gallium-

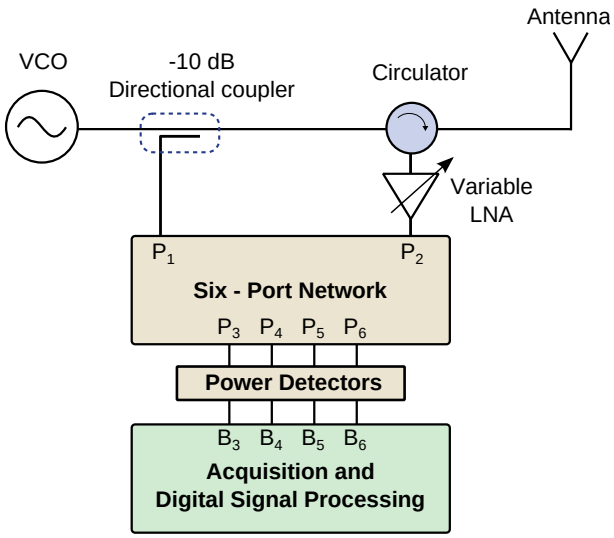

Figure 8.1: Schematic of the proposed Six-Port based monostatic radar [98]. (Copyright 2012, IEEE)

Arsenide zero bias Schottky diode (Aeroflex Metelics MZBD-9161) and an output low-pass filter, as described in section 4.2.4. The detector output signals in baseband B_3, B_4, B_5 and B_6 are subsequently amplified by precision low-noise operational amplifiers (LMP7718 from Texas Instruments) with variable gain configuration for signal conditioning purposes.

Dynamic range measurements (section 4.2.4) show that the proposed detector structure works for input signals from -50 dBm (tangential signal sensitivity) up to +10 dBm and features a voltage sensitivity of 2000 mV/mW at -40 dBm at 24 GHz [99].

The four baseband signals B_3, B_4, B_5 and B_6 are sent to an anti-aliasing filter and then to an ADC (*Maxim* MAX1305ECM). The acquisition system has been designed to acquire signals with an analog bandwidth up to 50 kHz featuring 8^{th} order Butterworth low-pass filter to avoid aliasing [100]. The signals are then sampled with 12 bit resolution at 640 Ksps. A digital signal processing board (*Altera DE2*) based on the *Altera Cyclone2* FPGA has been used to control the signal acquisition and the signal conditioning as well as to stream the acquired raw data via Ethernet to a computer. The transmitted data is received with a dedicated software socket and then processed via Matlab.

The control algorithm (see Fig. 8.2) monitors the four baseband signals (B_3,

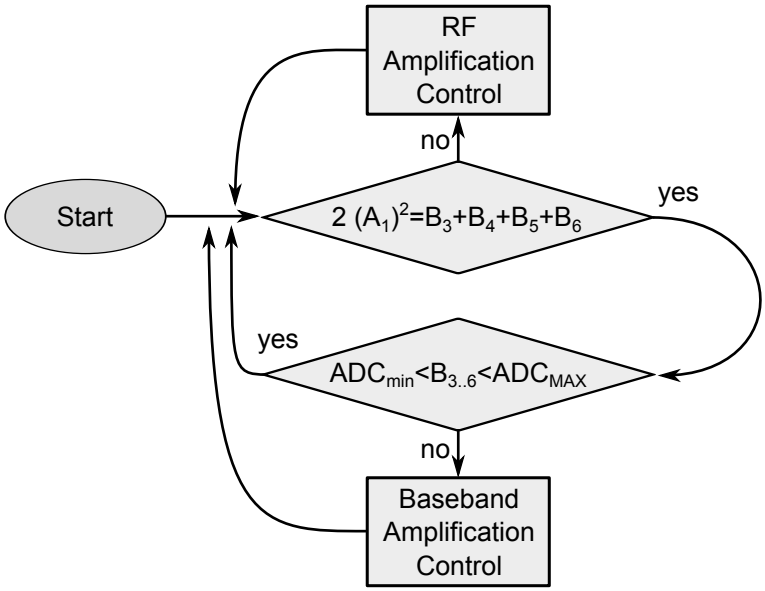

Figure 8.2: Flow chart of the signal conditioning algorithm according to [101]. (Copyright 2012, IEEE)

B_4, B_5, B_6) acquired by the ADCs. The first condition is to guarantee the same amplitude of the two Six-Port input signals. This is done by changing the RF amplification of the $\underline{P_2}$ signal. The amplitude of the reference signal (A_1) can be computed by measuring the four output voltages when the second input branch ($\underline{P_2}$) is isolated (no received signal, $A_2 = 0$) with the following:

$$A_1 = \sqrt{B_3 + B_4 + B_5 + B_6}|_{A_2=0}. \tag{8.1}$$

When this first condition is satisfied, a second conditioning step based on the control of the baseband amplifiers will be executed. Independent amplifiers are used to fit the baseband signals (B_3, B_4, B_5 and B_6) to the ADCs input dynamic range. The conditioning algorithm works in real-time in order to avoid any possible signal saturation and to guarantee the best acquisition condition.

8.2 Ambiguity Issue for Distance Measurements

The presented Six-Port receiver based ranging technique increases the measurement accuracy by a phase analysis in the microwave frequency domain

and offers high resolution for narrow-band signals. The basic Six-Port receiver phase evaluation for distance measurement exhibits some disadvantages that have been already presented in different publications [3,59,84,96, 97,102]. The total dynamic range of the output signal is mapped to the relative phase relations of the two input signals at the Six-Port receiver within half a wavelength. Since distance measurements with the Six-Port receiver are based on a phase-difference evaluation, an ambiguity issue occurs if the measured distance is larger than half a wavelength, in a way similar to the issue described in section 5.2 for DOA detection. Since the system relies on a normal phase measurement technique as soon as the phase difference slips over 2π RAD the system is not able to distinguish between periodical phase repetitions.

In other words, the distance to the target can only be measured with no ambiguity when the target moves within a range of half a wavelength ($\lambda/2$) of the signal used to perform the measurement ($\lambda/2$ is the maximum allowable range with no ambiguity problems). Therefore, making use of a single receiver and/or a single signal frequency does not allow an absolute measure of the target distance but only a relative measurement within a limited range of $\lambda/2$.

8.2.1 Phase Unwrap Solution

Nevertheless, there are possibilities to perform a distance measurement within a wide range. The simplest approach is to count the discontinuities in phase wraps between the periods and add an appropriate offset to the measured value. This approach is similar to the phase-unwrap function known from electronic measurement instruments like vector network analyzers. Unfortunately, this approach has some limitations. First, an initial position has to be known as reference from where the periods can be counted. Furthermore, the movements of the target in the measurement system have to be slow and continuous.

8.2.2 Frequency Offset Solution

Another approach is to use not only a single frequency, but at least two different frequencies with a spacing of f_{sp} between them [103]. The measurement is then done by calculating the phase difference between the reference signal and the back-scattered signal at both frequencies. Because of the different wavelengths this leads to two different phases with a similar

ambiguity. By subtracting these two phase-values the phase of the beat frequency can be calculated. This beat frequency is the same as f_{sp} and can be in the range of a few MHz up to the bandwidth of the Six-Port receiver at approximately a few GHz. A distance calculation can be also performed with this phase difference and therefore based on the beat frequency [103].

The phase from 0 to 2π RAD is mapped to the wavelength of the beat frequency leading to an unambiguous region of $c/(2\ f_{sp})$ being c the speed of light. Nevertheless, this procedure does not influence the sub-wavelength accuracy of the system, since the phase difference detection is still done at the microwave frequency. In other words: sub-millimeter accuracy can be reached over a measurement range of a few meters.

However, it has to be mentioned, that this method has a problem with fast moving targets, because the oscillator generating the two frequencies needs a settling time between the two measurements and in the meanwhile the observed object should not move. Furthermore, for very long range measurements, the calibration of the power detectors is essential since the received back-scattered signal power may change heavily over the measurement range. This has to be taken into account and the power detectors have to be characterized over a wide dynamic range as well as over at least two frequencies.

8.2.3 Difference Function Solution

A further solution hereby proposed makes use of two or more Six-Port receivers (Fig. 8.3). Assuming that the sources emit CW signals at different frequencies, these are then combined and emitted simultaneously. The signals propagate up to the target and get reflected, thus received after the round trip to the target. The signals are then splitted by a direction selective structure like a diplexer architecture (or by band-pass filters tuned to each emitted frequency followed by circulators) and sent to the related Six-Port receiver where the phase condition is then verified for each single frequency with each reference signal from the respective source.

As soon as the distance between the target and the DUT changes the phase condition at the various Six-Port receivers will change with a degree depending on the wavelength of the signal. A higher frequency signal will have a larger change in phase if compared to a lower frequency signal by means of the same shift of the target in reference to the radar.

It is therefore possible to have different periodical phase shifts for each

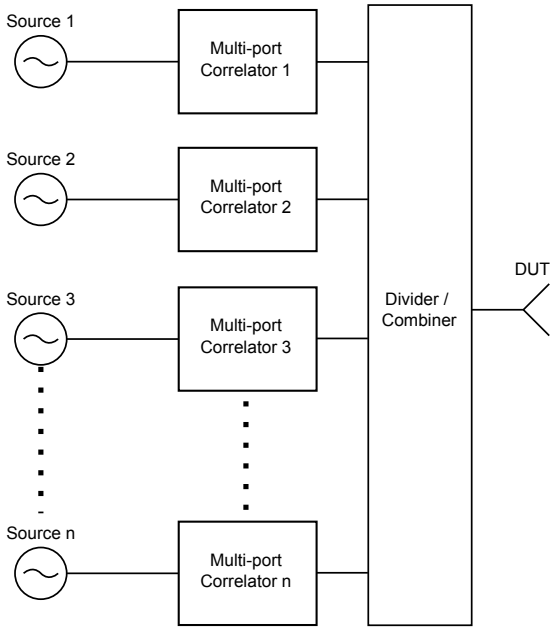

Figure 8.3: General concept schematic for an ambiguity-free Six-Port receiver based radar system.

single sub-system consisting of a VCO source and a Six-Port receiver (or one single Six-Port receiver with multiple VCO sources or even one receiver and a variable VCO source sequentially switching between different signals/frequencies as in the FSCW technique) when the distance to the target changes. By combining the phase shift information from two or more Six-Port receivers (also called correlators) it is possible to determine without ambiguity the distance of the radar from the target even if for each single sub-system several ambiguous periodical repetitions in the phase difference occur.

There are different ways to combine the phase information from the single receivers. By considering a dual Six-Port receiver system the two phase shifts dependent on the mentioned distance from the target can be for example subtracted, as explained in chapter 6. In this way a difference function is generated which has a periodicity that depends on the ratio between the periods of two phase shift functions.

If the frequency ratio between the two subsystems is chosen as a non-integer number, the resulting period of the difference function will be larger than

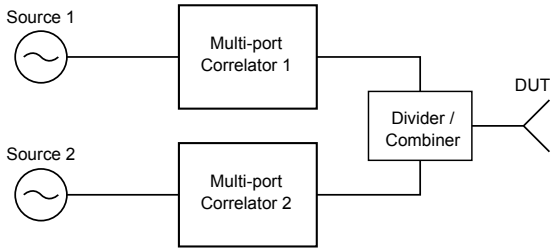

Figure 8.4: Concept schematic with two correlators

the periods of the phase shifts. Since the difference function is a step function with well defined steps within which a constant value can be found, it can be used to directly identify the period superposition of interest within a broad distance range and then consequently use the information provided by one of the Six-Port receivers to determine the exact distance (Fig. 8.5).

In other words, by analyzing the difference function the actual period can be determined leading to the cancellation of the ambiguity in phase by an offset correction conditioning the results. The offset correction factor can be mapped in the system during an initial calibration. For instance, each section defines a static offset which is added to the phase information from one Six-Port receiver (preferably the most accurate one with the highest operating frequency).

By taking as an example a system based on two different frequency sources with two corresponding Six-Port receivers, the periods of the standalone modules 1 and 2 are the wavelengths λ_1 and λ_2 respectively. These quantities, expressed as integer numbers can be mathematically expressed as the product of prime numbers as follows:

$$\lambda_i = \prod_p p^{\lambda_{i_p}}; \quad \text{with } i = 1;2 \quad \text{for } p = \{1, ..., \infty\} \tag{8.2}$$

where the exponents λ_{i_p} are non-negative integers that form a unique representation for each period quantity λ_1 and λ_2. The ambiguity free region derived from the difference of the values from the two subsystems can be therefore calculated as:

$$P[\text{diff}] = lcm(\lambda_1, \lambda_2) = \prod_p p^{max(\lambda_{1_p}, \lambda_{2_p})} \tag{8.3}$$

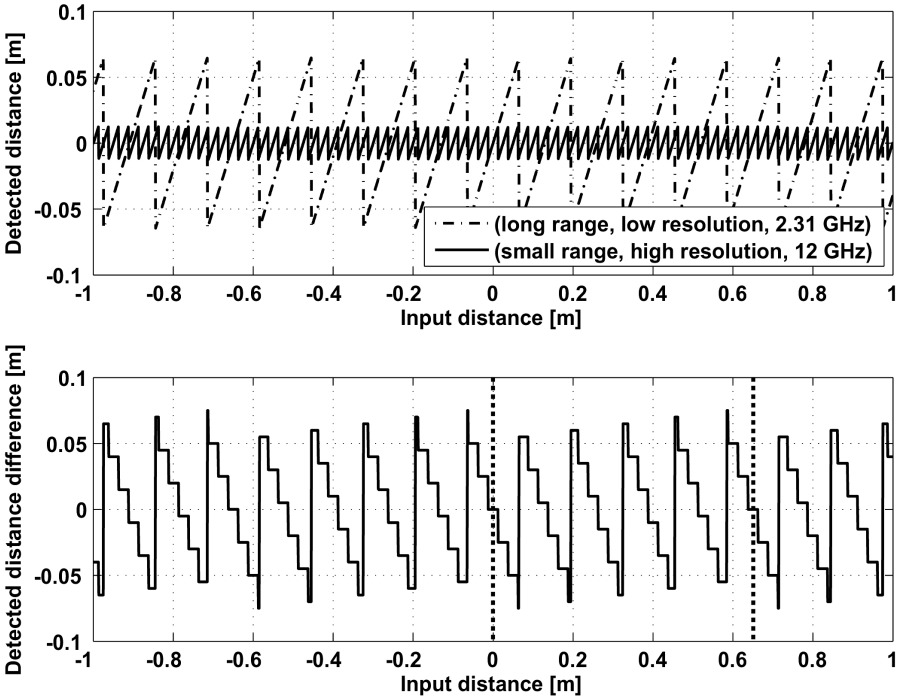

Figure 8.5: Phase shift and difference function of a dual Six-Port receiver with frequency ratio $n = 5.2$

where "lcm" is the Least Common Multiple of the two values λ_1 and λ_2. Fig. 8.5 depicts a possible scenario with a reasonable non-integer ratio of 5.2 between the two system frequencies (12 GHz and 2.31 GHz). The difference function is shown in the lower part of Fig. 8.5. In this case the difference function defines 31 steps within the ambiguity free range which can be used to uniquely identify the region of interest. The larger the ambiguity-free region with respect to the smallest wavelength of the system, the more steps will the difference function present.

The concept works also with one variable signal source and one Six-Port receiver by changing the frequency or the signal generated by the source and repeating the measurement sequentially instead of implementing a parallel architecture.

To achieve a large measurement range with no ambiguities a proper frequency ratio between the subsystems has to be chosen. Having as an example a dual Six-Port receiver system as depicted in Fig. 8.4 the two signal sources should be setup so that the ratio between their frequencies should

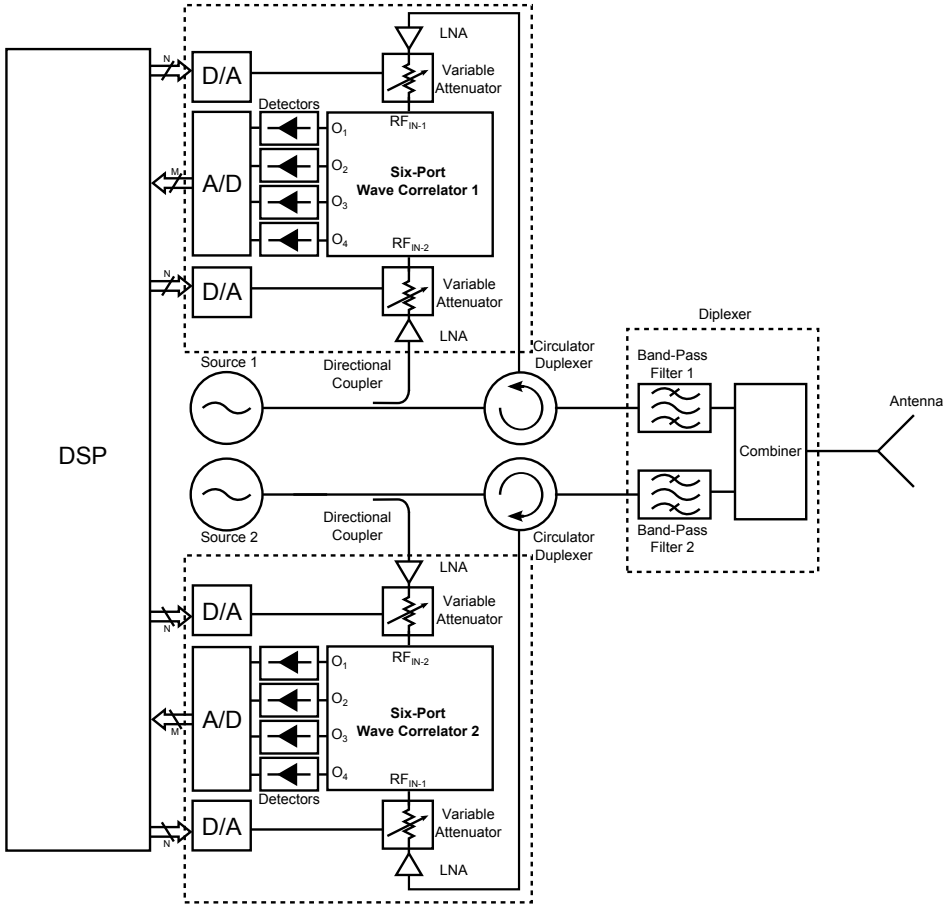

Figure 8.6: Detailed hardware schematic of a dual Six-Port receiver based radar.

be a non-integer irrational number, or a truncation of an irrational decimal sequence. In other words, the ratio between the two signal frequencies should have a non-periodic decimal sequence to guarantee a large period of the difference function used to solve the ambiguity problem. The ratio between the frequencies does not have to be necessarily large. The right choice of the frequency ratio can be done by analyzing the non-ambiguous range while changing the ratio between the two or more system frequencies.

As introduced in the paragraphs above, the proposed technique can be implemented with several techniques and different hardware architectures. A possible solution could be the one displayed in Fig. 8.6 where the system

is based on two Six-Port receivers with two parallel sources working at two different frequencies. The two sub-modules are connected to the same antenna through a network that combines the signals from the source to be delivered to the antenna and separates the received signals with band-pass filtering.

8.3 Measurement Results

To verify the ranging technique with the Six-Port receiver, a measurement setup has been prepared. A linear sweep of a metallic plate as a target has been performed by means of a high-precision computer controlled linear stage, the VT-80 with sub-micrometer resolution and optical encoder for a positioning feedback (manufactured by PI-miCos GmbH).

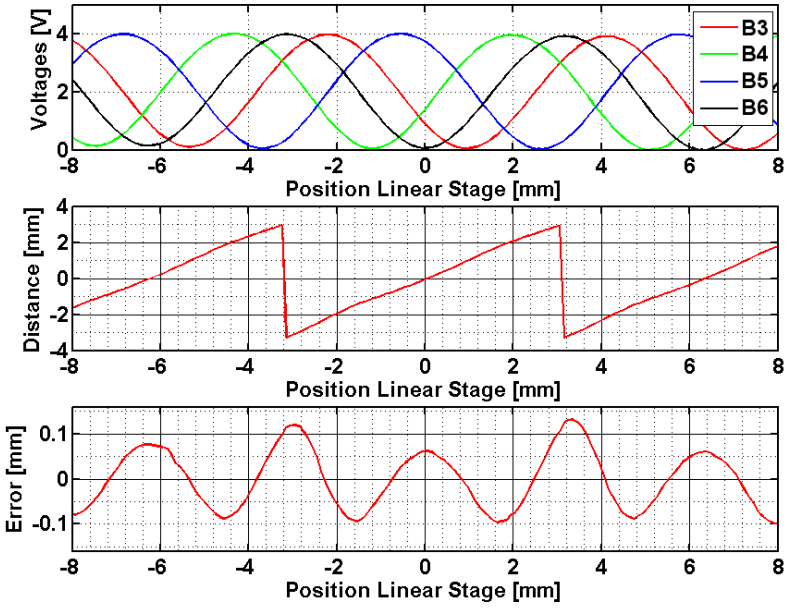

Figure 8.7: Linear movement detection and measurement error [98].
(Copyright 2012, IEEE)

Non-metallic shields and diverse dielectric slabs (polyurethane plastic foam sheets and wooden panels) have also been inserted between the radar and the target. A system response is plotted in Fig. 8.7. The system has intentionally been hereby adjusted with a simple linear calibration step. It is therefore possible to observe the nonlinear measurement error plotted at

the bottom of Fig. 8.7. The error is sinusoidal, deterministic and it is possible to compensate it as a system specific calibration curve. Once this curve is flattened in the system a fully calibrated measurement can be done. The response is now nearly linear, even for setup scenarios different from the one in which the nonlinear calibration has been performed. A measurement result for micrometer range distances is plotted in Fig. 8.8. The plot presents a measurement within the range of 10 µm with a detection error below 0.5 µm.

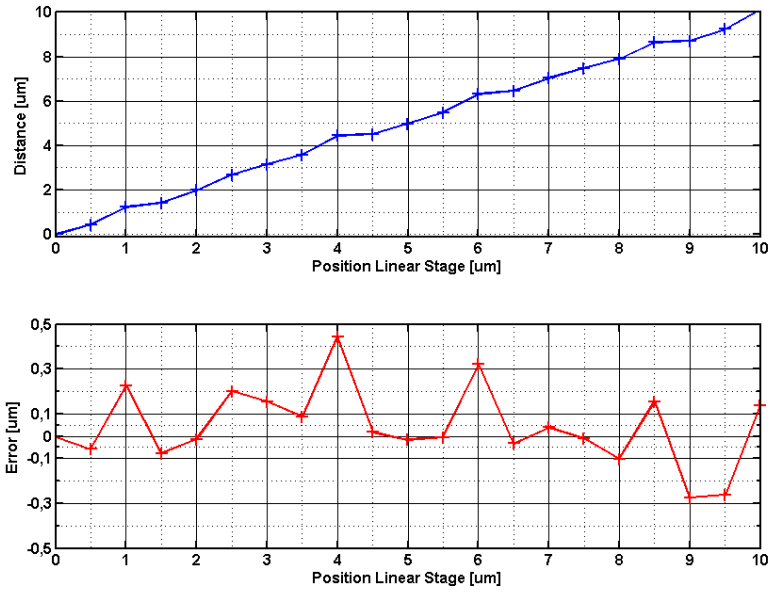

Figure 8.8: High precision linear measurement and relative error [98].

9 Displacement and Vibration Measurement

9.1 System Overview and Test Setup

Vibration measurement and detection is of great interest for many sensor applications and stress diagnosis in diverse industrial environments. An innovative mechanical vibration analysis based on the Six-Port receiver as a microwave interferometer radar is hereby proposed [104]. Due to the excellent phase discrimination properties of the Six-Port receiver a very high accuracy in the vibration detection can be reached. Due to its peculiar characteristics, the Six-Port receiver finds interesting applications in distance and displacement measurements [98]. In particular, vibration detection is an important task for automation and diagnosis in diverse industrial environments. An accurate vibration analysis allows to detect mechanical stress in complex industrial machinery.

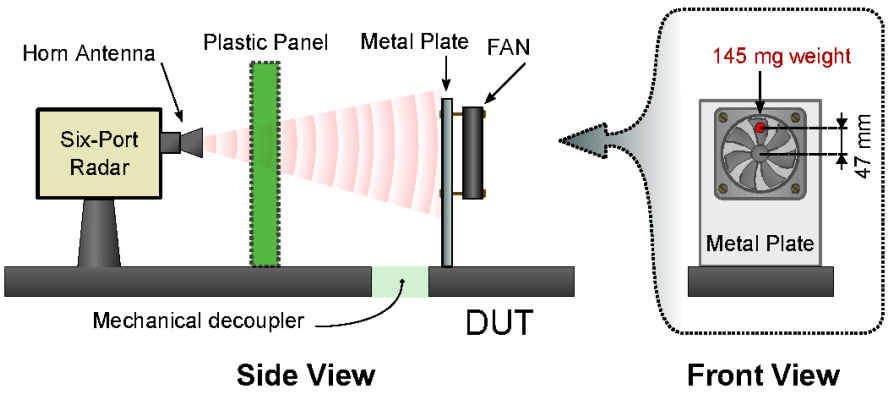

Figure 9.1: Test setup for the six-port interferometer radar with LOS and NLOS according to [104]. (Copyright 2013, IEEE)

The most commonly used technique is laser interferometry [105]. Main advantages of this method are contact-less sensing, high resolution and ex-

cellent frequency response. However, this optical based technique is not suitable in harsh environments, for instance, with the presence of dust or fog. The optical diffusion in a non-clear propagation media is the main disadvantage of this technique and introduces measurement errors since with increasing suspended particle density, dampening and scattering effects increase. The hereby presented Six-Port microwave interferometer radar does not suffer from the above mentioned problems since the proposed technique works also when a direct optical line of sight to the object under investigation is not present. Even optically non transparent dielectric slabs or non-metallic shields can be penetrated by the radar signal.

Other radar techniques such as pulse and FMCW radars are already in use since decades for almost all possible industrial sensing applications where optical systems cannot be used. Such techniques, being based either on a time difference or frequency offset evaluation in baseband, suffer from undesired effects. For instance, in the FMCW technique, in order to reach a high spacial resolution on short distance measurements (short-rage radar for small displacement detection or vibration analysis), very steep frequency ramps are generated. This leads to a nonlinear output frequency ramp from the VCO of the FMCW radar device [106]. The dynamic nonlinearities caused by the steep ramps of the VCOs can influence the performance of an FMCW radar. Phase evaluation has already been proposed as an additional measurement technique for FMCW radars in order to increase the measurement accuracy [107–109]. Nevertheless, up to now, the phase evaluation has been performed either directly in baseband or at the IF giving relatively low phase resolution [110]. In contrast, the Six-Port receiver can easily discriminate a phase difference directly at the microwave frequency.

The investigations and results hereby shown are based on the hardware prototype presented in the previous chapters (section 5.5) which operates at a frequency of 24 GHz. It has to be mentioned that the scope of the presented technique is to detect mechanical vibrations, or in other words, relative distance variations of a target that are comparable to the wavelength of the microwave signal. Therefore, the applications hereby addressed are not influenced by the ambiguity issue of the Six-Port receiver [63] as described in section 8.2.

9.2 Doppler Shift Effect

The Doppler effect has to be considered as a possible source of measurement error [104]. The target under investigation vibrates typically within a small range ($\leq \lambda/2$) and with a mechanical vibration frequency f_v. With these premises, having a vibration amplitude A_{max} the maximum speed of the vibrating target is [11]:

$$v_{max} = A_{max}\, 2\pi\, f_v\ . \tag{9.1}$$

The observed target moves, thus causing a Doppler frequency shift of the received frequency as described in eq. 7.1. In this case the maximum Doppler frequency shift can be described as [104]:

$$f_d = \pm\frac{2 f_s v_{max}}{c}\ . \tag{9.2}$$

Due to this Doppler shift the wavelength of the reference signal λ_r and the back-scattered signal wavelength λ_b are therefore different [104]. This results in a wavelength difference of [104]:

$$\Delta\lambda = \lambda_r - \lambda_b = \frac{c}{f_s} - \frac{c}{f_s \pm f_d}\ , \tag{9.3}$$

where c is the propagation speed of the microwave signal, and f_s is the CW radar signal frequency. Since the Six-Port receiver performs the distance evaluation only with a phase difference measurement, $\Delta\lambda$ is also the error in the overall distance measurement ($\Delta\lambda = \Delta d$). The distance evaluation error Δd is calculated directly from the speed of the target that is the time derivative of the target's displacement $x(t)$ described as a sinusoidal function of time [104]:

$$\Delta d = \lambda\, \frac{2v}{(c+2v)} = \lambda\, \frac{2\frac{\partial}{\partial t}x}{\left(c+2\,\frac{\partial}{\partial t}x\right)}\ , \tag{9.4}$$

$$x(t) = A_{max}\, sin(\omega t + \phi)\ , \tag{9.5}$$

where $\omega = 2\pi f_v$ and $\lambda = c/f_s$. Without loss of generality, it is hereby assumed that the phase ϕ of the mechanical vibration $x(t)$ is constant. This leads to [104]:

$$\Delta d = \lambda \, \frac{2\omega \; A_{max} \; cos(\omega t + \phi)}{c + 2\omega \; A_{max} \; cos(\omega t + \phi)} \; . \tag{9.6}$$

Since the speed v of the vibrating target is very low compared to the propagation speed of the microwave signal c, the above formula can be simplified to [104]:

$$\Delta d \approx 4\pi \, \frac{f_v}{f_s} \; A_{max} \; cos(\omega t + \phi) \; . \tag{9.7}$$

The distance evaluation error Δd is therefore a sinusoidal function with a $\pi/2$ RAD phase shift in comparison to x. The final detected vibration is therefore [104]:

$$d = A_{max} \left[sin(\omega t + \phi) + 4\pi \, \frac{f_v}{f_s} \; cos(\omega t + \phi) \right] \; . \tag{9.8}$$

Eq. (9.7) evidences that since $f_v \ll f_s$, Δd presents an extremely small amplitude compared to x. If f_v becomes very high, an effect on d can be noticed as a relative phase shift compared to x. Therefore, this does not influence the detected vibration frequency. Theoretically, for extremely high vibration frequencies where the speed of the target reaches values above $c/10$, the detected vibration becomes highly nonlinear, presenting harmonics in the spectrum. The main vibration frequency component is though still present as a dominant component. Nevertheless, this effect is practically not noticeable in a measurement setup, since such target vibrations are physically impossible. It is therefore evident, that a Doppler shift on the microwave signal induced by the moving target does not influence the detected distance accuracy in the Six-Port interferometer [104].

9.3 Oscillator Phase Noise Effect

Another possible source of measurement errors is the phase noise of the VCO source used in a radar device [104]. Since the measurement concept of the proposed technique is based on the phase modulation of the backscattered signal due to the mechanical movement of the target under observation, phase noise of the reference carrier can introduce additional uncertainties in the evaluation. The significant value that has to be taken into account for this analysis is the Single-Side-Band (SSB) phase noise profile

$L(f)$ of the VCO (expressed in dBc/Hz) versus the offset frequency (offset frequency range defined from a lower frequency limit a to an upper frequency limit b). This value can be derived from the definition of the integrated phase noise A over a chosen frequency offset[1]:

$$A = 2 \int_a^b L(f)\, df \ . \tag{9.9}$$

Following the calculations described in [111] by integrating the phase noise profile $L(f)$ over the frequency offset range (from a to b) and multiplying with the square of the offset frequency (f^2 under the integral) it is possible to define the RMS frequency error (residual FM, Δf_{FM}) of the VCO[2]:

$$\Delta f_{FM} = \sqrt{2 \int_a^b L(f)\ f^2\, df} \ . \tag{9.10}$$

Typical VCO components on the market (for instance, the *HMC739LP4* VCO from Hittite) present a Δf_{FM} between 10 kHz and 20 kHz. Since the residual FM causes in the Six-Port receiver a similar effect as the Doppler frequency shift, by inserting Δf_{FM} in eq. (9.3) instead of f_d, it is possible to calculate the maximum distance evaluation error caused by the oscillator phase noise as:

$$\Delta\lambda = \Delta d = \frac{c}{f_s} - \frac{c}{f_s \pm \Delta f_{FM}} \ , \tag{9.11}$$

It has to be underlined that such effects are neglectable for most applications since a frequency deviation between the reference and the backscattered signal of a few kHz opposed to microwave carrier frequencies causes an evaluation error of only a few nanometers. This beneficial effect is directly related to the phase evaluation technique of the Six-Port with additive mixing in the microwave domain.

[1] The choice of the offset frequency limits required for the calculation of the integrated phase noise A is relevant. As described at page 112, chapter 15 in [111], the relevant value for the calculation of the integral is the lower limit a, since the phase noise $L(f)$ rolls off with frequency and the upper limit b only slightly increases the result of the integrated phase noise A.

[2] The definition of residual FM (Δf_{FM}, sometimes also noted as σ_f) is reported in [111] chapter 15, at page 122.

9.4 Vibration Measurement Results

As Device Under Test (DUT) a common 12 cm diameter cooler fan has been used. The fan has been attached to a metal plate that serves as a bracket for the fan and is placed at a distance of two meters from the Six-Port radar (Fig. 9.1). The fan is not directly visible for the radar since it is placed on the backside of the metal plate. This setup emulates a scenario where an arbitrary vibrating or moving machine needs to be monitored.

Under normal operation the fan rotates with a constant speed and induces light vibrations on the metal plate that depend on the rotation speed and on multiple resonant modes of the DUT's mechanical structure. As soon as a variation in the working condition of the DUT occurs (different rotation speed or a mechanical malfunction) the vibrations on the structure will change. These vibrations are recorded by the Six-Port radar.

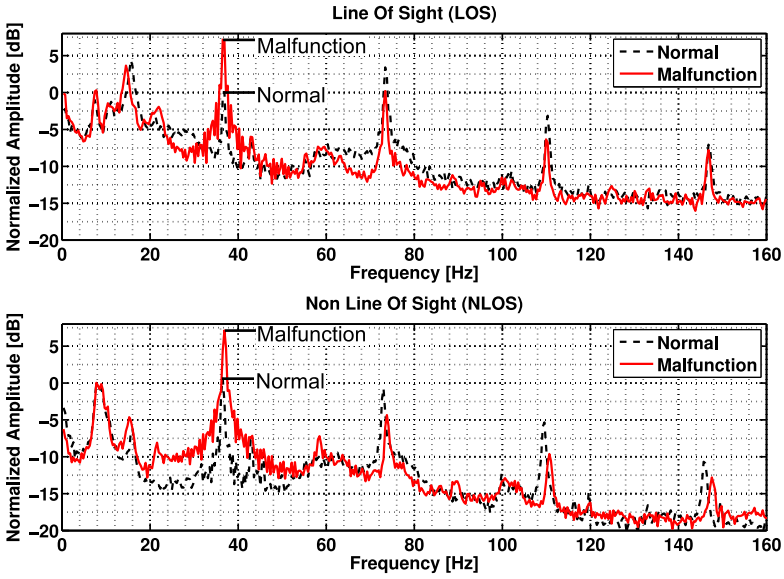

Figure 9.2: Vibration spectrum plot with DUT in LOS and NLOS under normal operating conditions and with a malfunction. The plot is normalized to the peak value in normal operation of the fundamental resonant frequency of 36 Hz (equivalent to the fan's rotation speed of 2160 RPM) [104]. (Copyright 2013, IEEE)

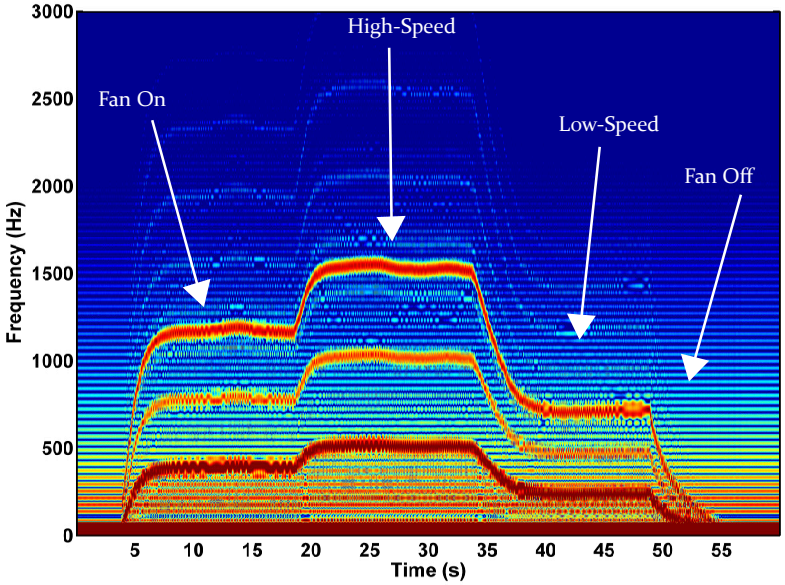

Figure 9.3: Spectrogram of the vibrations caused on a test setup by a rotating fan. The fan is first turned on, then the rotation speed is changed. Harmonics of the fundamental rotation speed can be noticed evidencing the different rotation speed levels [104].

The power of the CW microwave signal at 24 GHz emitted from the radar is -18.8 dBm radiated through a 20 dBi horn antenna. A malfunction of the rotating fan has been introduced by gluing a small plastic weight (145 mg) on one rotary blade at 47 mm distance from the rotation axis. This weight emulates a foreign object that causes a slight mass eccentricity in the rotating system, thus leading to different mechanical vibrations in the DUT that can be monitored with a Fast Fourier Transform (FFT) analysis. The measurement has been performed with the DUT in Line Of Sight (LOS) and in Non Line Of Sight (NLOS) by placing a plastic panel (Polypropylene) between the radar and the DUT (Fig. 9.1). The results are plotted in Fig. 9.2. The emulated malfunction introduces major differences in the spectrum. For instance, the peak amplitude of the fundamental mechanical resonance at 36 Hz increases in both LOS and NLOS scenarios.

Furthermore, another measurement has been done with the setup illustrated in Fig. 9.1. The vibration measurement has been performed for a

duration of 60 seconds while the fan has been turned on and the rotation speed was changed from normal mode, to high-speed and low-speed. Finally, the fan has been switched off again.

The different rotation speed levels of the fan cause variations in the vibrations of the setup. The results are hereby plotted with a spectrogram of these mechanical vibrations in a frequency range up to 3 kHz for the whole duration of the measurement (Fig. 9.3). These variations can be easily detected by the Six-Port radar. The high accuracy of the detection allows even to see the speed ramp up and ramp down of the fan when changing the rotation speed.

Six-Port technology is a promising new approach for vibration sensors. The main advantage is high accuracy, high speed distance detection with relatively low production costs. The complexity of the circuit is relaxed if compared to traditional radar based systems. An interferometer based contactless vibration measurement radar can be therefore implemented with the Six-Port technique. Unlike laser based optical interferometers the proposed hardware also works when a direct optical line of sight is not present.

10 Applications Overview

10.1 Automotive Radar Calibration

Radar technology is today a key feature for the automotive industry and is becoming of greater importance among most car-producers. Its applications range from cruise control, to pre-crash and parking aid systems, and radar units are already being mounted on several automobiles. In particular, long-range radars installed in front of today's vehicles to scan the path ahead and detect dangerous situations and obstacles have a major role in driving assistance systems. The benefits of this innovative technology are directed towards increasing the safety and enhancing the driving comfort, thus covering an important role in the driving experience. Great effort has been done to develop and build functional, accurate, compact, robust but still cost-effective automotive radars such that nowadays systems can be easily implemented in many vehicles. Despite all the important results achieved in the research, development and implementation of such devices, major problems still exist in the correct installation, calibration and especially in the alignment of automotive radars on the vehicles. It is important to remark that a correct installation and consequent calibration of these devices is essential for proper working conditions and exact interpretation of the information delivered from such sensors. Minor variations in the behavior of such devices could lead to false alarms or misleading data adding more dangerous situations while driving, especially when such systems automatically control the dynamics of the vehicle with brake assistance.

10.1.1 The Problem of Automotive Radar Misalignment

During the quality inspection at the end of an automotive production line radar systems are checked and calibrated so to align the narrow radar beam to the thrust vector of the vehicle. This procedure is essential to ensure that

the radar sight matches the actual environment setup in front of the vehicle. Typical long-range cruise control radar has a foresight of 150 m. Alignment problems during installation lead to a misalignment angle that brings to an incorrect scanning of the path in front of the vehicle. Currently, these systems are calibrated by using optical alignment techniques, employing a laser beam for a geometrical adjustment of the radar device housing with respect to the vehicle thrust vector. Such a technique is not taking into account the possible mismatch of the radar beam in respect to the device housing, since it is not relying on a measurement of the real radiation pattern, but on a mechanical reference. All these mismatches and tolerances result in misalignment angles that cannot be predicted and that lead to problems for the device during working conditions in the cruise control. The situation is illustrated in Fig. 10.1.

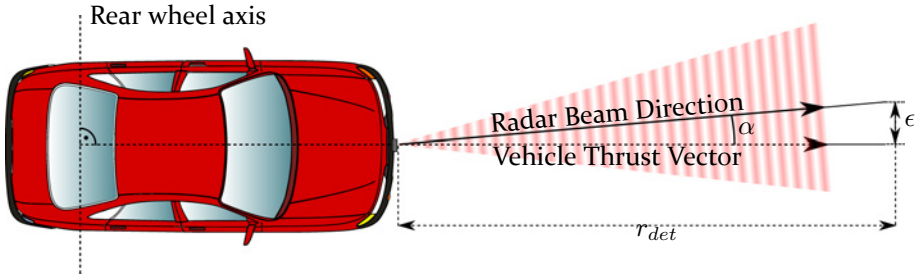

Figure 10.1: Schematic picture of automotive radar misalignment according to [112]. (Copyright 2009, IEEE)

Introducing an angle α between the radar beam direction and the thrust vector of the vehicle (usually orthogonal to the rear wheel axis of the car) having the radar device a detection range r_{det}, a linear misalignment error ϵ can be derived with the following formula:

$$\epsilon = r_{det} \tan(\alpha). \tag{10.1}$$

For a misalignment angle $\alpha = \pm 0.5$ deg tolerated by currently available mechanical alignment systems, at the limit of the scanning range of the radar (typically $r_{det} = 150$ m) the error will be of $\epsilon = \pm 1.30$ m. This brings to an uncertainty of 2.60 m, definitely critical for standard automotive applications. With such an error, the radar cruise system would sense vehicles coming in the opposite lane or rather obstacles present at the edge of the path instead of cars or objects present on the driving lane.

10.1.2 Misalignment Detection for Automotive Applications

Following the theory introduced in chapter 2, especially the misalignment angle detection explained in sections 2.3 and 2.4, it is possible to detect the misalignment of a highly focused radar antenna with respect to a reference geometrical axis (thrust vector of the vehicle) [112, 113]. Two phase measurement antennas are aligned on an axis orthogonal to the thrust vector of the vehicle. As introduced in section 2.4.3 the measured phase difference $\Delta\phi$ between the two antennas can be directly related to the radar beam direction. The relation between $\Delta\phi$ and the misalignment angle α (eq. (2.26)) is hereby reported again:

$$\alpha = \sin^{-1}\left(\Delta\phi\frac{\lambda}{2\pi L}\right), \tag{10.2}$$

where λ is the wavelength of the radar signal and L is the distance between the two antennas. A cost-effective, robust and compact solution is to use a Six-Port based receiver, introduced in chapter 4. By implementing the Six-Port receiver as described in chapter 5, it is possible to set up a misalignment angle detector for automotive radar calibration. Hardware implementations of the proposed technique for automotive radars working at 77 GHz [62] as well as measurement results are explained in detail in chapter 5, section 5.6 and chapter 6 section 6.2. L can be optimized for a specific automotive radar alignment measurement following eq. (2.27) and (2.28) presented in section 2.4.3 [60].

10.1.3 Relevance in the Industry

The proposed technique can be successfully used to perform an accurate calibration of automotive radars at the end of the production line in automotive industry. The Six-Port receiver ensures precision and measurement repeatability with a robust and low cost solution. Furthermore, by being so compact and by requiring only a few hardware components, the system can be also used in service centers, where a low-cost and non-complex calibration and adjustment technique of the automotive radar is necessary. The technique hereby described has been patented by the author together with Dr.-Ing. A. Koelpin through Daimler AG [114].

10.2 Industrial Positioning

Industrial automation is nowadays an essential technology underlying our modern society. Advanced positioning and sensor feedback tasks in automation processes often require distance and displacement detection, for example, to measure and track the movement of robots. Furthermore, the detection of mechanical stress in complex industrial machinery through an accurate vibration analysis is often a task of major interest.

Therefore, high-resolution distance measurements with short and long range positioning are important for a large number of sensing applications and can also be used as a precondition for vibrometer applications. Several automation technologies rely on high precision positioning sensors to track linear as well as rotational movements of various machinery. The tracked positioning information provided by the sensor interface determines the accuracy of the positioning system, thus the quality of the overall industrial automation process.

Moreover, the positioning sensor serves the control systems and algorithms as an interface to the physical world, being therefore directly involved in the physical properties of the environment and of the observed target. Several approaches have been implemented up to now, making use of different physical principles such as optical techniques as well as radar technology showing different advantages and disadvantages. Nevertheless, the requirements imposed by industrial environments often cause big challenges to traditional positioning sensors.

Laser interferometry and laser pulse time-difference measurements are the most common optical high-resolution, contact-less distance measurement techniques. Laser techniques feature high accuracy, high resolution as well as a wide dynamic range and excellent frequency response. Concerning these parameters optical systems are superior compared to all other common techniques.

The downturn of optical techniques is the difficulty to penetrate dust and fog with the laser in harsh environments. These inconveniences of laser based systems are the cause of an increasing interest in alternative non-optical measurement techniques that are robust against such industrial environment conditions. One of the main non contact-based alternatives to laser is the radar technique.

The main advantage of radar versus optical based systems is that the measurement concept is based on the propagation of microwave signals that in-

teract in a different way with the environment. Radar based measurement techniques work also when a direct optical line of sight to the object under investigation is not guaranteed since radar waves can propagate much better through foggy or dusty air. Furthermore, even bulky and optically non transparent dielectric slabs or non-metallic shields can be penetrated by the radar signal.

Another advantage of radar based systems is that due to the technical advances in RF printed circuit board and Monolithic Microwave Integrated Circuits (MMIC) production, the manufacturing costs of microwave circuits dropped relevantly in the last decade. Therefore, nowadays radar is cheaper than an equivalent optical measurement system. Many radar techniques such as pulse and FMCW radars are already in use since decades for almost all possible industrial sensing applications where optical systems cannot be used. The measurement technique based on the Six-Port interferometer radar principle provides excellent measurement properties, proving to be immune to several undesired effects influencing common distance and rotation measurements.

10.2.1 Angle Measurements

Six-Port based DOA detectors can be used to track the relative position of radio frequency sources, regardless if continuous wave, FMCW or pulse modulation is used. For instance, an active radar beacon positioned on a target can be tracked to monitor the targets position [59]. Furthermore, even reflected signals can be analyzed with such a DOA detector.

For instance, the accurate angular orientation of a machine surface can be monitored through a secondary radar concept. A continuous wave microwave signal is emitted from an antenna towards the target's surface. The reflected signal is then received by the DOA detector that performs an incoming angle detection of the reflected signal. The change in the orientation of the reflecting surface leads to a different angle of incidence of the signal at the DOA detector. By using the techniques explained in section 2.4 a measurement of the incident angle can be done. In this way it is easily possible to monitor the rotation of industrial mechanical constructions, such as planar moving platforms or any mechanical reference plane position.

The main issues of Six-Port based DOA detection concerns the detection of sources (DOA detection) in multi-path scenarios as well as multi-target

detection, which at present generates ambiguities in the detection results. These problems have been tackled recently and possible solutions that can discriminate multiple targets as well as cancel multi-path interference are being investigated.

10.2.2 Vibration Measurement and Modal Analysis

Particularly interesting is the analysis of small displacements of an observed target, for instance vibration monitoring. Since the Six-Port based distance measurement provides very high accuracy distance detection, even the smallest vibrations (i.e. distance variations of the target surface with respect to the sensor) can be accurately detected [115]. Performing a frequency domain analysis (for instance with a Fast Fourier Transform) a spectrogram of the mechanical vibrations of the observed target can be obtained. This leads to useful information about the working conditions of diverse industrial machinery. Six-Port based DOA detectors can be used for modal analysis in order to measure the dynamic response of mechanical structures and the different vibration modes.

By observing for instance a rotating turbine, thus illuminating the complete machine with the Six-Port distance measurement radar sensor, the main mechanical resonances can be recorded and monitored. In case of a mechanical malfunction or degradation, for instance a wearing of the axis bearings, minor changes in the mechanical resonances will occur [115]. Such effects can be therefore monitored without even applying sensors directly to the surface of the machine. In other words, a contact-less vibration analysis for diverse industrial machines can be easily performed by Six-Port technology based sensors. As the reconstruction algorithms feature low complexity and can be calculated very fast, the maximum detectable vibration frequency is only limited by the sampling frequency of the system [115].

10.3 Medical Applications

Heartbeat and breath rate monitoring is of primary interest for several medical applications that range from simple vital sign detection to accurate monitoring of a patient's health status. Several different diagnosis procedures benefit from these vital sign monitoring techniques. For instance, the ability to observe the breath and heart beat of a patient over night allows to detect sleep disorders or anomalies.

A wide diffusion of Electro-Cardio-Graph (ECG) or Cardiopulmonary Diagnostic Devices (CPD) is taking place not only in hospitals and medical care centers but also in domestic environments for home-care and telemedicine. For these kind of scenarios contact-less ECG and CPD techniques are strongly preferred and have therefore been lately of great interest in the medical and scientific community. The workaday life in clinical environments could benefit from such a system, since a patient will not have to be connected by wires in order to be monitored.

10.3.1 State of the Art in Contactless Vital-Sign Monitoring

Several different concepts based on different physical principles have been proposed, although most of the introduced contact-less concepts are based on the detection of minor geometrical changes of the patients torso due to heartbeat and breathing. In order to detect such minor variations several solutions based on the radar principle with traditional heterodyne transceivers were introduced in the past [116]. First Doppler radar experiments were conducted in the early 1970s. Nevertheless, poor performance of the proposed approaches led to the introduction of alternative systems [117]. Those are based on pneumatic mattress sensors or carbon dioxide detectors for breath monitoring, however, these techniques can only be considered as semi-contact-less [118, 119]. Thus, radar techniques are preferred due to several advantages with respect to other solutions.

An improvement in performance of various radar techniques in the last decade boosted the research oriented towards this particular application scenario. Several approaches based on FMCW radar techniques attracted the attention of the scientific community. However, only a few radar systems that have been presented reach the required accuracy. Most of FMCW radars require an extremely wide frequency band of operation to reach the required accuracy level. Some advanced FMCW systems perform measurements with an accuracy in the micrometer range [120]. Though the performance of such systems is strongly related to the linearity of the generated frequency ramps. Non-idealities in the frequency sweep from the VCO of the FMCW radar device introduce measurement errors.

Furthermore, another relevant aspect for the right choice of the frequency of operation is the spectrum allocation with different bands and licensing schemes. For the target applications, it is necessary that a radar based sensor works within specified ISM bands. Therefore, such devices always need to satisfy a trade-off between bandwidth, compliance within ISM bands and

center frequency of operation. Other alternative radar techniques that satisfy these criteria have also been introduced. CW radar technology has been implemented showing excellent results [121]. Nevertheless, most accurate measurements of minor distance variations can be performed by interferometric methods.

10.3.2 Six-Port Based Heartbeat and Breath Rate Monitoring

Microwave interferometry offers the advantages of microwave propagation and material interaction with high resolution and low complexity of the radar device. The Six-Port interferometer can easily discriminate a minor phase difference directly at the microwave frequency presenting therefore excellent spatial detection accuracy. The heartbeat and breathing activities affect the phase of the reflected signal which is compared with the reference signal source in the radar device, as described in chapter 8. A CW radar signal is sent towards the patient under test to observe minor mechanical movements of the patients body. These movements are caused by the respiration as well as heartbeat and can be tracked by analyzing the phase modulation of the back-scattered signal.

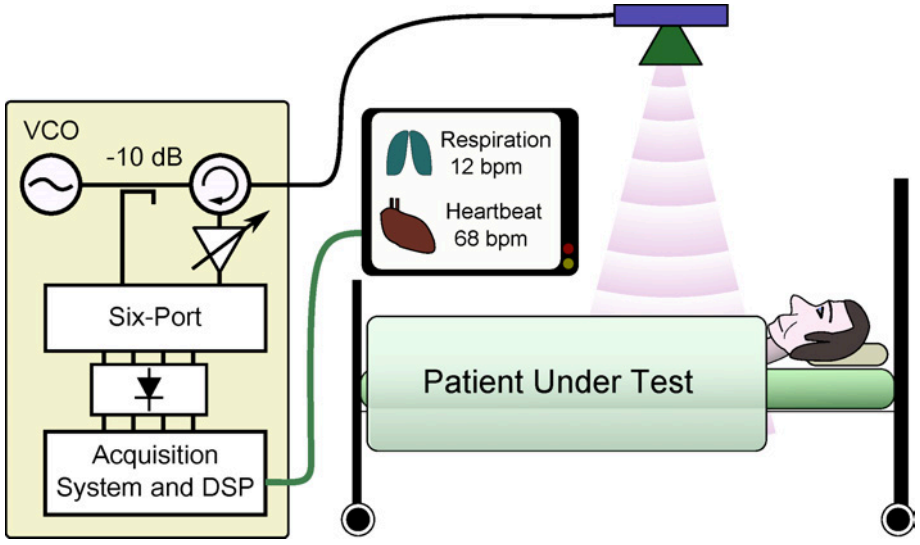

Figure 10.2: System concept of the proposed sensor device according to [101]. (Copyright 2012, IEEE)

The penetration depth of the signal in the patients' body is approximately 1.52 mm for a 24 GHz microwave signal. Furthermore, the maximum reflec-

tivity of the patients' skin is of approximately 39 %. Therefore, the radiated signal will mainly be reflected at the patients upper skin layer. The patients respiration will result in a significant and periodic extension of the torso, which is in the range of several millimeters. Additionally, the heartbeat will be superimposed to this movement, which is assumed to be in the sub-millimeter range. The cardiac electrical impulse is followed by a contraction of the heart muscle. Subsequently, a variation of the ventricle volume occurs. The mechanical pressure wave propagates through the thorax and leads, together with the extension of the blood vessels due to the heart expansion, to minor skin movements in the sub-millimeter range. This periodic movements and vibrations can subsequently be detected by extensive signal post-processing.

The vital parameter monitoring is based on a continuous measurement of the distance between the radar module and the person under test. It is obvious, that this measurement leads to ambiguities if the target moves more than half a wavelength. But because of the continuous monitoring the appearing phase wraps can easily be detected and corrected by commonly known phase unwrap algorithms.

10.3.3 Demonstrator Description and Measurement Results

A standard measurement has been performed with the Patient Under Test (PUT) lying on his back while the Six-Port based radar sensor was observing the chest of the person at a distance of approximately 1 m.

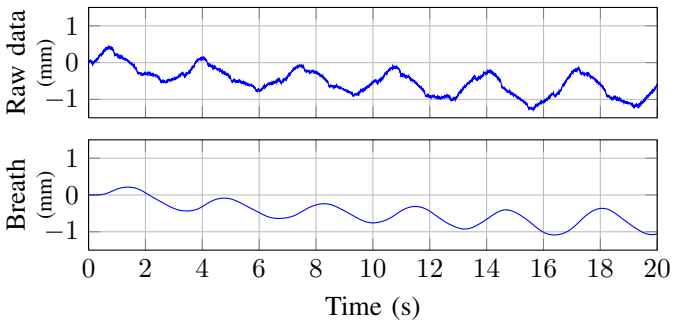

Figure 10.3: Time domain signal of the measured raw data and low-pass filtered breathing signal extraction [101].

The results are plotted in Fig. 10.3. In the raw time domain data of the

modulated distance it is possible to recognize the breathing as well as minor heart activity. By properly filtering the raw signal a clear time domain respiration monitoring can be performed. By subtracting the calculated respiration signal from the raw data, it is possible to extract the heart beat signal which is plotted in Fig. 10.4. For a direct comparison, the detected heart beat signal is compared to a reference Electro-Cardio-Graph (ECG) from a dedicated ECG measurement belt. The Six-Port measurement matches exactly the reference ECG signal.

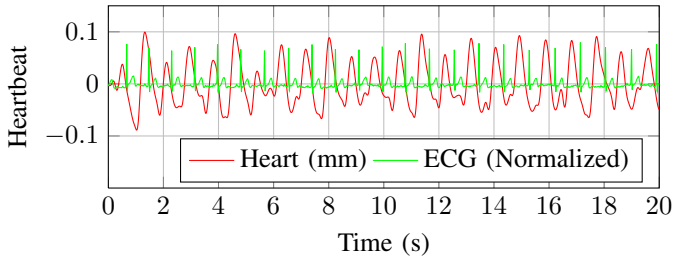

Figure 10.4: Measured heart beat signal in time domain compared to a reference Electro-Cardio-Graph (ECG) [101].

Furthermore, a frequency domain analysis has been performed. The Power Spectral Density (PSD) of the signal has been calculated with an FFT leading to the results plotted in Fig. 10.5. A peak for the respiration rate is evident and the detected heart beat rate matches exactly the rate from the reference ECG.

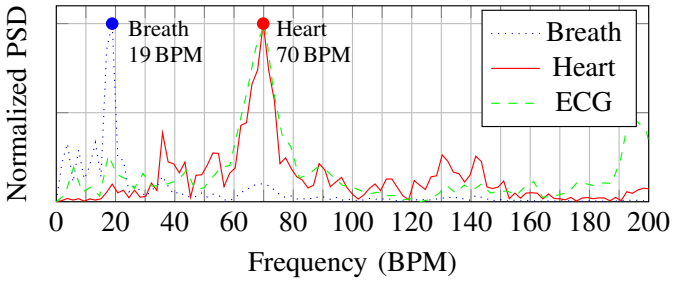

Figure 10.5: Normalized Power Spectral Density (PSD) of the measured breath and heart rate signals compared to the PSD of a reference Electro-Cardio-Graph (ECG) [101].

To test the system under real conditions, the shown measurements have

been also conducted under several different scenarios of patient under test and radar positions. Two setups feature the patient in an upright sitting position, measuring the vital signs from the front and the back of the patient. The other two scenarios have been acquired, while the patient was lying on the back and in abdominal position, respectively. In this scenario the radar sensor is positioned on a table over the patient at a distance of approximately 1 m. The transmitted power is -30 dBm at 24 GHz. These setups are illustrated in Fig. 10.6.

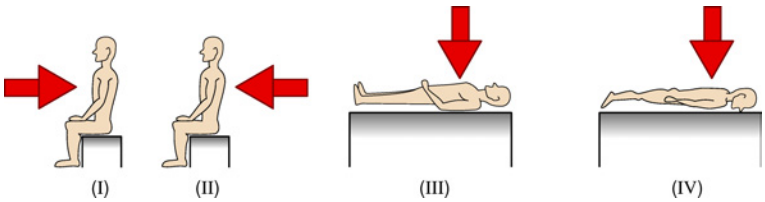

Figure 10.6: Measurement positions of the patient under test with direction of observation and position of the radar sensor marked as a red arrow [101]. (Copyright 2012, IEEE)

As can be seen in Fig.10.7 and in Fig.10.8 the results show excellent performance and detection accuracy in all test cases. Nevertheless, the heat beat detection is more challenging when the PUT is in position IV since the superimposed heartbeat signal is nearly neglectable if compared to the amplitude of the respiration signal. Also the time dependent scaling of the amplitude is a result of the breathing influence and filtering. Nevertheless, the periodicity and the principle characteristics states accurate heart beat detection. Excellent heart beat detection can be performed when the PUT is monitored as in position II (PUT in seated position and is observed from the back). These results lead to interesting conclusions for several monitoring applications where the PUT is not necessarily monitorable in a standard position.

This technique features several advantages with respect to classical radar concepts. High accuracy in the micrometer scale as well as low system complexity are some of the benefits of the Six-Port receiver. Simple digital signal processing algorythms allow a clear detection of the patients respiration rate as well as heartbeat from the raw radar signal reflected from the person's torso.

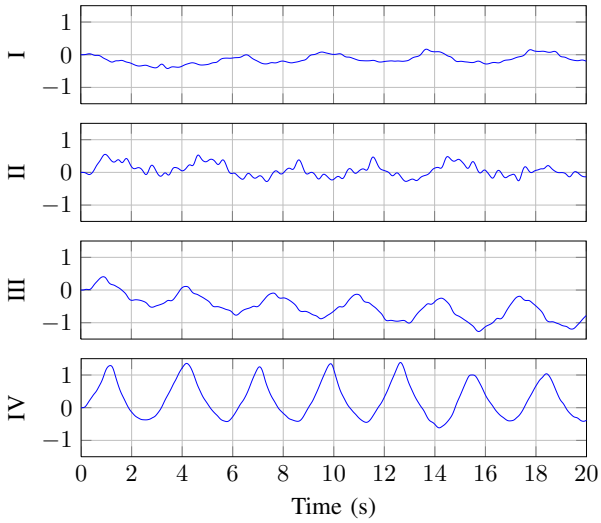

Figure 10.7: Time domain signals featuring the breathing process of low-pass filtered raw data for different measurement scenarios according to Fig. 10.6. Vertical Scaling is in (mm) [101].

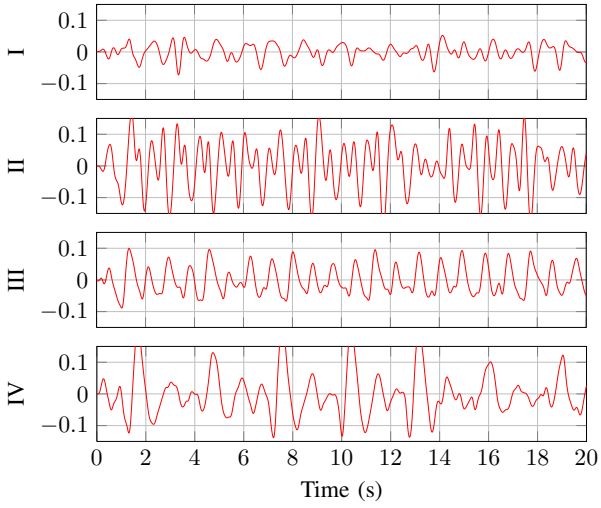

Figure 10.8: Time domain signals of band pass filtered heart beat signal for different measurement scenarios according to Fig. 10.6. Vertical Scaling is in (mm) [101].

11 Conclusions and Outlook

The Six-Port receiver proves to be a promising technology for diverse industrial positioning sensors, for both ranging or angle measurements. Several applications can benefit from the positive aspects of the Six-Port DOA and ranging concepts. Microwave circuit integration such as Monolithic Microwave Integrated Circuit (MMIC) technology can also contribute to a larger scale distribution and to a shift of this technology to higher frequencies. This can lead to even cheaper, more accurate and more compact sensor systems for diverse industrial as well as consumer implementations throughout different application scenarios. First steps that can lead to the integration in MMIC technology have been presented in chapter 5, section 5.6.

However, it must be noted that there are limitations of the Six-Port DOA and ranging technique. Multi-path propagation can interfere with both distance as well as angle measurements. Most noticeable effect of strong multi-path interference (due to undesired reflections on surfaces other than the target itself) is a measurement inaccuracy. To avoid this undesired effect, a highly focused beam for the radiating antenna has to be used, in order to force the system to only illuminate the target and observe only the object of interest ignoring influences coming from the environment.

Another limitation of this technology is the relatively low dynamic range offered by the Six-Port receiver. The poor performance of the passive diode-based power detectors in the Six-Port structure as well as the nonlinear power-voltage transfer characteristic of the Schottky diode detectors introduce limitations for the detection performance. For most of the industrial sensing applications, this is not an issue, but for some low-power applications this could be an important limitation. For instance, a long distance measurement of a monitored target (for vibration or position detection) could be critical due to attenuation in the propagation channel when the power level of the reflected signal is lower than the noise floor of the power detectors used in the Six-Port receiver.

However, the Six-Port technology is a promising new approach for positioning sensors. The main advantage is high accuracy detection with relatively low production costs. There is no need for a local oscillator to perform DOA detection. This is a major advantage for detection systems that need to be untraceable. Furthermore, an accuracy in the micrometer range can be achieved at relatively low microwave frequencies. The complexity of the circuit is relaxed if compared to traditional radar systems. The mixer structure is easy to implement (mainly passive microstrip structures on a RF substrate). Moreover, the numerical effort for DOA angle calculation as well as ranging is very low. The baseband signal processing is therefore relaxed and can be performed at high speed with low power digital hardware such as small micro-controllers.

In this work, several milestones in Six-Port based direction finding and ranging techniques have been reached. The theory, system concept and detection performance of DOA detectors and distance measurement radars based on the Six-Port technology have been investigated and verified by hardware measurements. Furthermore, demonstrator systems have been developed and built taking into account a complete system concept, from the microwave antennas and receivers up to digital signal processing and software. For the first time, it has been shown that Six-Port based DOA detection is capable of detecting DOA angles of a few milli-degrees with relatively low effort in hardware and software design. Furthermore, as a unique feature in this work, the dual Six-Port concept has been introduced for the first time ever as a solution to the ambiguity issue. As a highlight result of this research, a patent on the Six-Port based DOA and misalignment detection of automotive radars has been registered in cooperation with Daimler AG [114].

The Six-Port based ranging technique has been investigated and developed with respective hardware demonstrators taking into account several application scenarios. Outstanding results have been reached in the fields of vibration and displacement analysis for industrial and medical applications underlying the benefits of the Six-Port radar technique.

The research results presented by the author in this work recently raised the interest of the radar industry. As a result, in a joint project involving the University of Erlangen-Nuremberg and InnoSenT GmbH (Innovative Sensor Technology), further research on the Six-Port radar technique has been conducted. The first commercially available Six-Port radar sensor has been developed [115]. This device works in the ISM band at 24 GHz, integrates antenna structure, Six-Port receiver front-end and digital signal processing

in a compact form factor and robust enclosure. It can be used in one-target scenarios for distance and vibration measurements. Therefore, this work led to foundations of Six-Port radar technology for the first successful industrial implementation of this technique.

Currently, a lot of research is being conducted on this topic with further cooperation between the University of Erlangen-Nuremberg and industry. As next steps, absolute distance measurement, stability over a wide operation temperature range, multi-target tracking as well as immunity to multi-path interference are being addressed. These can be reached with the help of special modulation schemes and particular calibration routines currently under investigation. The fusion of continuous wave microwave interferometry and modulation scheme based radar techniques can lead to several benefits and is currently being implemented in the first industrial Six-Port radar module. Early results have been reached at the time of writing and show great potential for this hybrid technology based on the Six-Port receiver. As a result, special measurement applications have already found for the Six-Port positioning technology to be the proper solution to reach the desired performance specifications.

Note of Thanks

I have developed this work during five years of research activities involved in the preparation for my PhD at the Institute for Electronics Engineering, Friedrich-Alexander University of Erlangen-Nuremberg. The flourishing research environment at the institute, the availability of high-end equipment as well as appropriate funding and well organized work-flow made this research results possible.

First of all, I would like to thank my doctoral adviser and chair of the institute, Prof. Robert Weigel. With his charismatic lead he created this amazing academic constellation of research topics, appropriate funding partners and a homelike working atmosphere. The close personal relationship and the reciprocal trust and responsibility laid a solid motivational basement to my work, giving me valuable support during these years. I can hardly express my gratitude for the countless personal development possibilities, and professional benefits for my academic career offered me. Next I would like to thank Prof. Reinhard Knöchel for being the second supervisor and Prof. Georg Fischer for his academic assistance.

I am grateful to my colleague, team-leader and friend Dr.-Ing. Alexander Kölpin, the creative spark of ideas that guided me in this work. No matter how busy the schedule was, he always found time to discuss problems and ideas related to my research topic. With his outstanding know-how and experience in Six-Port technology as well as active academic presence he played a significant role in my PhD career.

Furthermore, I would like to thank all my colleagues at the Institute for Electronics Engineering that supported me. From the early times when I started working at the institute, I would like to thank among many others hereby not listed, my friends and colleagues Stefan Zorn, Benjamin Waldmann, Benjamin Lömmle, Christoph Kandziora, Jochen Rascher, Dietmar Kissinger, Benjamin Sewiolo and Jochen Essel for their cooperation and friendliness.

Later on during my research activities I could always count on the help of further new colleagues and friends. Many thanks to Armin Talai, Markus Gardill, Roman Agethen, Maximilian Hofmann, Florian Oesterle, Giovanni Donati and Giuseppe Gottardo for all their support, creative discussions and motivation during the composition of the thesis. I would like to thank especially my Six-Port team colleagues Francesco Barbon, Stefan Lindner and

Sebastian Mann. Without their commitment, motivation and willingness to cooperate in all situations, no matter what, when or how, this work would have not been possible. The synergy of this unique team lead to outstanding research results documented in numerous scientific publications. Furthermore, I would like to thank Adrian Voinea who supported my experiments and realized the demonstrators with his outstanding technical competence and expertise.

I want to express my cordial thanks to my parents, Zord Agnes and Ivano Vinci as well as to my brother and sister Carlo and Virag Vinci for their support and encouragement during all these years. Finally, I would like to thank Sarah Linz for fruitful discussions and her valuable assistance at my side all times.

Author Bibliography

- S. Iliev, G. Vinci and J.F. Luy, "RFID System Read Range in Automobile Assembly Lines," in *CST 3rd European User Group Meeting*, 2007.

- G. Vinci and A. Sona, "Electromagnetic Analysis and CAD Modelling of an RF-ID System," in *16th IMEKO TC4 Symposium: Exploring New Frontiers of Instrumentation and Methods for Electrical and Electronic Measurements (IMEKO 2008)*, 2008.

- G. Vinci, A. Koelpin, and R. Weigel, "Employing Six-Port Technology for Phase-Measurement-Based Calibration of Automotive Radar," in *Microwave Conference Proceedings (APMC), 2009 Asia-Pacific*, pp. 329-332, 2009.

- A. Koelpin, G. Vinci, "Verfahren und Vorrichtung zur Ermittlung einer Ausrichtung von Sensoren eines Fahrzeugs - Method for determining orientation of e.g. pulsed radar sensor, of sensor system that is coupled with e.g. distance controller, of vehicle, involves emitting sensor signal, and determining orientation of sensor relative to reference axis," *DE Patent DE102009017369A1*, 14.04.2009, 2009.

- B. Sewiolo, G. Vinci, G. Fischer, and R. Weigel, "Mixed-Mode S-Parameter Design of Ultra-Wideband Coupled-Line Baluns," in *Electromagnetics in Advanced Applications, 2009. ICEAA 09. International Conference on*, pp. 55-58, 2009.

- G. Vinci and A. Sona, "Characterization of a 13.56 MHz RF-ID System Based on Scattering Parameters Approach," in *Radio and Wireless Symposium, 2009. RWS09. IEEE*, pp. 441-444, 2009.

- G. Vinci and R. Weigel, "Multiband Planar Vivaldi Antenna for Mobile Communication and Industrial Applications," in *Electromagnetics in Advanced Applications (ICEAA), 2010 International Conference on*, pp. 93-96, 2010.

- G. Vinci, A. Koelpin, F. Barbon, and R. Weigel, "Six-Port-Based Direction-

Of-Arrival Detection System," in Microwave Conference Proceedings, 2010 Asia-Pacific (APMC), pp. 1817-1820, 2010.

- A. Koelpin, G. Vinci, B. Laemmle, D. Kissinger, and R. Weigel, "The Six-Port in Modern Society," in *Microwave Magazine, IEEE, vol. 11, no. 7*, pp. 35-43, 2010.

- A. Koelpin, G. Vinci, B. Laemmle, and R. Weigel, "The Enhanced Six-Port Receiver: A New Concept for Simultaneous Data Reception and Direction-Of-Arrival Detection," in *Microwave Symposium Digest (MTT), 2011 IEEE MTT-S International*, pp. 1-4, 2011.

- B. Laemmle, G. Vinci, L. Maurer, R. Weigel, and A. Koelpin, "An Integrated 77-GHz Six-Port Receiver Front-End for Angle-Of-Arrival Detection," in *Bipolar/BiCMOS Circuits and Technology Meeting (BCTM), 2011 IEEE*, pp. 219-222, 2011.

- G. Vinci, B. Waldmann, R. Weigel, and A. Koelpin, "An Ultra-Wideband Antenna for FMCW-Radar Positioning Systems," in *Antennas and Propagation (EUCAP), Proceedings of the 5th European Conference on*, pp. 372-374, 2011.

- G. Vinci, F. Barbon, R. Weigel, and A. Koelpin, "A High Accuracy Direction-Of-Arrival and Misalignment Angle Detector," in *Microwave Conference (GeMIC), 2011 German*, pp. 1-3, 2011.

- G. Vinci, F. Barbon, R. Weigel, and A. Koelpin, "A Novel, Wide Angle, High Resolution Direction-Of-Arrival Detector," in *Radar Conference (EuRAD), 2011 European*, pp. 265-268, 2011.

- R. Weigel, G. Vinci, B. Laemmle and A. Koelpin, "A New Concept for Aligning Automotive Long-Range Radar Modules Based on Wireless Microwave Sensing," in *Sensor+Test Conferences*, pp. 366-369, 2011.

- F. Barbon, G. Vinci, S. Lindner, R. Weigel, and A. Koelpin, "Signal Processing Strategies for Six-Port Based Direction-Of-Arrival Detector Systems," in *Systems, Signals and Devices (SSD), 2012 9th International Multi-Conference on*, pp. 1-5, 2012.

- F. Barbon, G. Vinci, S. Lindner, R. Weigel, and A. Koelpin, "A Six-Port In-

terferometer Based Micrometer-Accuracy Displacement and Vibration Measurement Radar," in *Microwave Symposium Digest (MTT), 2012 IEEE MTT-S International*, pp. 1-3, 2012.

- A. Koelpin, S. Lindner, G. Vinci, B. Laemmle, and R. Weigel, "The Enhanced Six-Port Architecture: A Measurement Based Proof of Concept," in *Wireless Sensors and Sensor Networks (WiSNet), 2012 IEEE Topical Conference on,* pp. 29-32, 2012.

- A. Koelpin, G. Vinci, F. Barbon, S. Lindner, G. Fischer, and R. Weigel, "The Six-Port Technology: A Low-Cost Concept for Precise Position Measurements," in *Systems, Signals and Devices (SSD), 2012 9th International Multi-Conference on*, pp. 1-5, 2012.

- A. Koelpin, G. Vinci, B. Laemmle, S. Lindner, F. Barbon, and R. Weigel, "Six-Port Technology for Traffic Safety," in *Microwave Magazine, IEEE, vol. 13, no. 3*, pp. 118-127, 2012.

- B. Laemmle, G. Vinci, L. Maurer, R. Weigel, and A. Koelpin, "A 77-GHz SiGe Integrated Six-Port Receiver Front-End for Angle-of-Arrival Detection," in *Solid-State Circuits, IEEE Journal of, vol. 47, no. 9*, pp. 1966-1973, 2012.

- S. Lindner, F. Barbon, G. Vinci, R. Weigel, and A. Koelpin, "Initial Calibration Procedure of a Six-Port Receiver System for Complex Data Reception," in *Radar Conference (EuRAD), 2012 9th European*, pp. 570-573, 2012.

- G. Vinci, F. Barbon, B. Laemmle, R. Weigel, and A. Koelpin, "Wide-Range, Dual Six-Port Based Direction-Of-Arrival Detector," in *Microwave Conference (GeMiC), 2012 The 7th German,* pp. 1-4, 2012.

- G. Vinci, F. Barbon, B. Laemmle, R. Weigel, and A. Koelpin, "A Wide-Range 77 GHz Direction of Arrival Detector with Integrated Dual Six-Port Receiver," in *Microwave Symposium Digest (MTT), 2012 IEEE MTT-S International*, pp. 1-3, 2012.

- G. Vinci, F. Barbon, B. Laemmle, R. Weigel, and A. Koelpin, "Six-Port Based Direction Finding and Micrometer-Accuracy Displacement Detection," in *CST 8th European User Group Meeting*, 2012.

- G. Vinci, F. Barbon, S. Lindner, R. Weigel, and A. Koelpin, "Six-Port Based High Resolution Smart Antenna Alignment Sensor," in *Antennas and Propagation in Wireless Communications (APWC), 2012 IEEE-APS Topical Conference on*, pp. 280-283, 2012.

- G. Vinci, B. Laemmle, F. Barbon, R. Weigel, and A. Koelpin, "A 77 GHz Direction-Of-Arrival Detector System with SiGe Integrated Six-Port Receiver," in *Radio and Wireless Symposium (RWS), 2012 IEEE*, pp. 247-250, 2012,

- G. Vinci, S. Lindner, F. Barbon, M. Hofmann, G. Fischer, D. Kissinger, and A. Koelpin, "24 GHz Six-Port Medical Radar for Contactless Respiration Detection and Heartbeat Monitoring," in *Radar Conference (EuRAD), 2012 9th European*, pp. 75-78, 2012.

- G. Vinci, S. Lindner, F. Barbon, R. Weigel, and A. Koelpin, "Promise of a Better Position," in *Microwave Magazine, IEEE, vol. 13, no. 7*, pp. S41-S49, 2012.

- G. Vinci, S. Lindner, S. Mann, F. Barbon, S. Linz, R. Weigel, and A. Koelpin, "Six-Port Microwave Interferometer Radar for Mechanical Vibration Analysis," in *Radar Conference (EuRAD), 2013 10th European*, 2013.

- S. Mann, G. Vinci, S. Lindner, F. Barbon, S. Linz, R. Weigel and A. Koelpin, "Improved Dual Six-Port Receiver Structure for Two-Dimensional Direction of Arrival Detection Using pHEMT Power Detectors," in *Radar Conference (EuRAD), 2013 10th European*, 2013.

- A. Koelpin, G. Vinci, S. Lindner, S. Mann, F. Barbon, S. Linz, F. Oesterle, R. Weigel, "Six-Port Technology for Precise Geometrical Measurement Applications - An Overview," in *Radar Conference (EuRAD), 2013 10th European*, 2013.

- S. Lindner, G. Vinci, F. Barbon, S. Linz, S. Mann, R. Weigel, A. Koelpin, "Instantaneous Frequency Measurement Based on Low-Cost Six-Port Technology," in *Microwave Conference (EuMC), 2013 10th European*, 2013.

- G. Vinci, S. Lindner, F. Barbon, S. Mann, M. Hofmann, A. Duda, R.

Weigel, and A. Koelpin, "Six-Port Radar Sensor for Remote Respiration Rate and Heartbeat Vital-Sign Monitoring," in *Microwave Theory and Techniques, IEEE Transactions on, vol. 61, no. 5*, pp. 2093-2100, 2013.

- S. Mann, G. Vinci, S. Lindner, S. Linz, F. Barbon, R. Weigel, and A. Koelpin "61 GHz Six-Port Radar Front-End for High Accuracy Range Detection Applications," in *Antennas and Propagation in Wireless Communications (APWC), 2013 IEEE-APS Topical Conference on*, pp. 818-821, 2013.

- G. Vinci, S. Lindner, S. Mann, F. Barbon, R. Weigel, and A. Koelpin "Dual Six-Port Based Direction-of-Arrival Detector for FMCW Radar Tracking in the ISM Band at 24GHz," in *Sensors, 2013 IEEE*, 2013.

- S. Lindner, G. Vinci, F. Barbon, S. Mann, R. Weigel, and A. Koelpin "Dual Tone Approach for Unambiguous Six-Port Based Interferometric Distance Measurements," in *Microwave Symposium Digest, 2013 IEEE MTT-S International*, 2013.

- F. Oesterle, G. Vinci, R. Weigel, and A. Koelpin " A novel, W-band Microwave Based Contactless Test Method for Mechanical Sensitivity Analysis of MEMS," in *Microwave Symposium Digest, 2013 IEEE MTT-S International*, 2013.

- S. Linz, G. Vinci, S. Mann, S. Lindner, F. Barbon, R. Weigel, and A. Koelpin "A Compact, Versatile Six-Port Radar Module for Industrial and Medical Applications," in *Journal of Electrical and Computer Engineering, Special Issue on Multi-Port Technology: New Perspectives and Applications - Hindawi Publishing Corporation*, 2013.

Bibliography

[1] I. Molina-Fernandez, A. Moscoso-Martir, J. M. Avila-Ruiz, R. Halir, P. Reyes-Iglesias, J. de Oliva-Rubio, and A. Ortega-Monux, „Multiport Technology for Microwave and Optical Communications," in *Microwave Symposium Digest (MTT), 2012 IEEE MTT-S International*, 2012, pp. 1 –3.

[2] I. Molina-Fernandez, J. Wanguemert-Perez, A. Ortega-Monux, R.-G. Bosisio, and K. Wu, „Coherent Optical Frequency Domain Six-Port Measurement Technique," in *Optical Fiber Communication Conference, 2005. Technical Digest. OFC/NFOEC*, vol. 2, 2005, p. 3 pp. Vol. 2.

[3] A. Koelpin, G. Vinci, B. Laemmle, D. Kissinger, and R. Weigel, „The Six-Port in Modern Society," *Microwave Magazine, IEEE*, vol. 11, no. 7, pp. 35 –43, 2010.

[4] Z. Chen, *Introduction to Direction-Of-Arrival Estimation*. Boston: Artech House, 2010.

[5] S. Chandran, *Advances in Direction-Of-Arrival Estimation*. Boston: Artech House, 2006.

[6] B. Friedlander, *Classical and Modern Direction-Of-Arrival Estimation*. Amsterdam Boston: Academic, 2009.

[7] R. Collin, *Foundations for Microwave Engineering*. New York: IEEE Press, 2001.

[8] N. Kinayman, *Modern Microwave Circuits*. Boston, Mass: Artech House, 2005.

[9] J. Jackson, *Classical Electrodynamics*. New York: Wiley, 1999.

[10] D. Wolf, *Essentials of Electromagnetics for Engineering*. Cambridge New York: Cambridge University Press, 2001.

[11] D. Pozar, *Microwave Engineering*. Hoboken, NJ: Wiley, 2012.

[12] P. Russer, *Fields, Networks, Computational Methods, and Systems in Modern Electrodynamics : a tribute to Leopold B. Felsen*. Berlin New York: Springer, 2004.

[13] K. Warnick, *Problem Solving in Electromagnetics, Microwave Circuit, and Antenna Design for Communications Engineering*. Boston: Artech House, 2006.

[14] J. Volakis, *Antenna Engineering Handbook*. New York: McGraw-Hill, 2007.

[15] C. Balanis, *Modern Antenna Handbook*. Hoboken, NJ: Wiley, 2008.

[16] ——, *Antenna Theory : Analysis and Design*. Hoboken, NJ: Wiley Interscience, 2005.

[17] G. Fowles, *Introduction to modern optics*. New York: Dover Publications, 1989.

[18] H. Pollard, *Sound waves in solids*. London: Pion, 1977.

[19] M. J. P. Musgrave, „The propagation of elastic waves in crystals and other anisotropic media," *Reports on Progress in Physics*, vol. 22, no. 1, p. 74, 1959.

[20] J. Golio, *The RF and Microwave Handbook*. Boca Raton, Florida: CRC Press, 2001.

[21] W. Stutzman, *Antenna Theory and Design*. Hoboken, NJ: Wiley, 2013.

[22] D. Barton, *Radar technology encyclopedia*. Boston: Artech House, 1997.

[23] W. Deng, *Time Multiplexed Beam-Forming with Space-Frequency Transformation*. New York, NY: Springer, 2013.

[24] J. Hagen, *Radio-Frequency Electronics : Circuits and Applications*. Cambridge New York: Cambridge University Press, 1996.

[25] P. Horowitz, *The Art of Electronics*. Cambridge England New York: Cambridge University Press, 1989.

[26] W. Namgoong and T. Meng, „Direct-Conversion RF Receiver Design," *Communications, IEEE Transactions on*, vol. 49, no. 3, pp. 518 –529, 2001.

[27] V. D. Min Zou and J. Wong, „Quad Demodulators Arm Direct-Conversion Receivers," *Microwave and RF*, vol. 7470, p. 4 pages, 2005.

[28] D. Tucker, „The History of the Homodyne and Synchrodyne," *Radio Engineers, Journal of the British Institution of*, vol. 14, no. 4, pp. 143 –154, 1954.

[29] R. Fessenden, „"Wireless Signaling" (Heterodyne Principle)," U.S. Patent Patent 706,740, August 12, 1902.

[30] T. Sarkar, R. Mailloux, A. Oliner, and D. Sengupta, *History of Wireless*, ser. Wiley Series in Microwave and Optical Engineering. Wiley, 2006.

[31] N. Cotanis, „The Radio Receiver Saga: An Introduction To The Classic Paper By Edwin H. Armstrong," *Proceedings of the IEEE*, vol. 85, no. 4, pp. 681 –684, 1997.

[32] G. Beers and W. Carlson, „Recent Developments in Superheterodyne Receivers," *Proceedings of the Institute of Radio Engineers*, vol. 17, no. 3, pp. 501 – 515, 1929.

[33] C. Hoer, *Using six-port and eight-port junctions to measure active and passive circuit parameters*, ser. Technical note. U.S. Dept. of Commerce, National Bureau of Standards, 1975.

[34] G. Engen and R. Beatty, „Microwave Reflectometer Techniques," *Microwave Theory and Techniques, IRE Transactions on*, vol. 7, no. 3, pp. 351–355, 1959.

[35] R. Beatty, G. Engen, and W. J. Anson, „Measurement of Reflections and Losses of Waveguide Joints and Connectors Using Microwave Reflectometer Techniques," *Instrumentation, IRE Transactions on*, vol. I-9, no. 2, pp. 219–226, 1960.

[36] G. F. Engen, „A Method of Determining the Mismatch Correction in Microwave Power Measurements," *Instrumentation and Measurement, IEEE Transactions on*, vol. 17, no. 4, pp. 392–395, 1968.

[37] G. Engen, „A Transfer Instrument for the Intercomparison of Microwave Power Meters," *Instrumentation, IRE Transactions on*, vol. I-9, no. 2, pp. 202–208, 1960.

[38] G. F. Engen, „Power Equations: A New Concept in the Description and Evaluation of Microwave Systems," *Instrumentation and Measurement, IEEE Transactions on*, vol. IM-20, no. 1, pp. 49–57, 1971.

[39] G. F. Engen and C. A. Hoer, „Application of an Arbitrary 6-Port Junction to Power-Measurement Problems," *Instrumentation and Measurement, IEEE Transactions on*, vol. 21, no. 4, pp. 470–474, 1972.

[40] G. F. Engen, „Calibration of an Arbitrary Six-Port Junction for Measurement of Active and Passive Circuit Parameters," *Instrumentation and Measurement, IEEE Transactions on*, vol. 22, no. 4, pp. 295–299, 1973.

[41] G. Engen, „The Six-Port Reflectometer: An Alternative Network Analyzer," *Microwave Theory and Techniques, IEEE Transactions on*, vol. 25, no. 12, pp. 1075–1080, 1977.

[42] G. F. Engen, „An Improved Circuit for Implementing the Six-Port Technique of Microwave Measurements," *Microwave Theory and Techniques, IEEE Transactions on*, vol. 25, no. 12, pp. 1080–1083, 1977.

[43] ——, „Calibrating the Six-Port Reflectometer," in *Microwave Symposium Digest, 1978 IEEE-MTT-S International*, 1978, pp. 182–183.

[44] ——, „Calibrating the Six-Port Reflectometer by Means of Sliding Terminations," *Microwave Theory and Techniques, IEEE Transactions on*, vol. 26, no. 12, pp. 951–957, 1978.

[45] G. Engen and C. Hoer, „The Application of "Thru-Short-Delay" to the Calibration of the Dual Six-Port," in *Microwave Symposium Digest, 1978 IEEE-MTT-S International*, 1978, pp. 184–185.

[46] S. Winter, „A Six-Port Receiver Architecture for 60-GHz OFDM Communication Systems," Ph.D. dissertation, Friedrich-Alexander University of Erlangen-Nuremberg, 2008.

[47] A. Koelpin, „Der erweiterte Sechstor-Empfaenger - Ein systemuebergreifender Ansatz fuer Kommunikations- und Messaufgaben," Ph.D. dissertation, Friedrich-Alexander University of Erlangen-Nuremberg, 2010.

[48] F. M. Ghannouchi and A. Mohammadi, *The Six-Port Technique*. Artech House, 2009.

[49] S. Mann, G. Vinci, S. Lindner, F. Barbon, S. Linz, R. Weigel, and A. Koelpin, „Improved Dual Six-Port Receiver Structure for Two-Dimensional Direction of Arrival Detection Using pHEMT Power Detectors," in *Radar Conference (EuRAD), 2013 10th European*, 2013.

[50] K. C. Gupta, *Microstrip Lines and Slotlines*. Boston: Artech House, 1996.

[51] T. C. Edwards, *Foundations of Interconnect and Microstrip Design*. Chichester New York: John Wiley, 2000.

[52] H. Wheeler, „Transmission-Line Properties of a Strip on a Dielectric Sheet on a Plane," *Microwave Theory and Techniques, IEEE Transactions on*, vol. 25, no. 8, pp. 631–647, 1977.

[53] D. Swanson, *Microwave Circuit Modeling Using Electromagnetic Field Simulation*. Boston: Artech House, 2003.

[54] C. A. Hoer, „A Network Analyzer Incorporating Two Six-Port Reflectometers," *Microwave Theory and Techniques, IEEE Transactions on*, vol. 25, no. 12, pp. 1070–1074, 1977.

[55] K. Chang, *Handbook of RF/Microwave Components and Engineering*. Hoboken, N.J: Wiley-Interscience, 2003.

[56] B. Laemmle, G. Vinci, L. Maurer, R. Weigel, and A. Koelpin, „A 77-GHz SiGe Integrated Six-Port Receiver Front-End for Angle-of-Arrival Detection," *Solid-State Circuits, IEEE Journal of*, vol. 47, no. 9, pp. 1966–1973, 2012.

[57] ——, „An Integrated 77-GHz Six-Port Receiver Front-End for Angle-Of-Arrival Detection," in *Bipolar/BiCMOS Circuits and Technology Meeting (BCTM), 2011 IEEE*, 2011, pp. 219–222.

[58] B. Laemmle, „Design and Applications of Integrated Millimeter-Wave Six-Port Circuits," Ph.D. dissertation, Friedrich-Alexander University of Erlangen-Nuremberg, 2012.

[59] G. Vinci, A. Koelpin, F. Barbon, and R. Weigel, „Six-Port-based Direction-Of-Arrival Detection System," *Microwave Conference Proceedings (APMC), 2010 Asia-Pacific, Yokohama, Japan*, pp. 1817 –1820, 2010.

[60] G. Vinci, F. Barbon, R. Weigel, and A. Koelpin, „A High Accuracy Direction-Of-Arrival and Misalignment Angle Detector," in *Microwave Conference (GeMIC), 2011 German*, 2011, pp. 1–3.

[61] B. Laemmle, G. Vinci, L. Maurer, R. Weigel, and A. Koelpin, „An Integrated 77-GHz Six-Port Receiver Front End for Angle-of-Arrival Detection," in *Proc. Bipolar/BiCMOS Circuits and Technologies Meeting (BCTM) 2011, Atlanta, USA*, 2011, pp. 220–223.

[62] G. Vinci, B. Laemmle, F. Barbon, R. Weigel, and A. Koelpin, „A 77 GHz Direction of Arrival Detector System with SiGe Integrated Six-Port Receiver," in *Radio and Wireless Symposium (RWS), 2012 IEEE*, 2012, pp. 247–250.

[63] G. Vinci, F. Barbon, R. Weigel, and A. Koelpin, „A Novel, Wide Angle,

High Resolution Direction-Of-Arrival Detector," in *Radar Conference (EuRAD), 2011 European*, 2011, pp. 265–268.

[64] G. Vinci, F. Barbon, B. Laemmle, R. Weigel, and A. Koelpin, „Wide-Range, Dual Six-Port Based Direction-Of-Arrival Detector," in *Microwave Conference (GeMiC), 2012 The 7th German*, 2012, pp. 1–4.

[65] ——, „A Wide-Range 77 GHz Direction-of-Arrival Detector With Integrated Dual Six-Port Receiver," in *Microwave Symposium Digest (MTT), 2012 IEEE MTT-S International*, 2012, pp. 1–3.

[66] G. Vinci, S. Lindner, S. Mann, F. Barbon, R. Weigel, and A. Koelpin, „Dual Six-Port Based Direction-of-Arrival Detector for FMCW Radar Tracking in the ISM Band at 24GHz," in *Sensors, 2013 IEEE*, 2013.

[67] M. Skolnik, *Introduction to Radar Systems*. Boston: McGraw Hill, 2001.

[68] G. M. Brooker, „Understanding Millimeter Wave FMCW Radars," *1st International Conference on Sensing Technology, Palmerston North, New Zealand*, vol. 1, pp. 24–32, 2005.

[69] G. Brooker, *Long-range Imaging Radar for Autonomous Navigation*. Sydney, Australia: Australian Centre for Field Robotics, School of Aerospace, Mechanical and Mechatronic Engineering, University of Sydney, 2005.

[70] J. D. Taylor, *Introduction to Ultra-Wideband Radar Systems*. CRC Press, December 16, 1994.

[71] T. Musch, I. Rolfes, and B. Schiek, „A highly Linear Frequency Ramp Generator Based on a Fractional Divider Phase-Locked-Loop," *Instrumentation and Measurement, IEEE Transactions on*, vol. 48, no. 2, pp. 634–637, 1999.

[72] G. Vinci, S. Lindner, F. Barbon, R. Weigel, and A. Koelpin, „Promise of a Better Position," *Microwave Magazine, IEEE*, vol. 13, no. 7, pp. S41–S49, 2012.

[73] S. Piper, „FMCW Linearizer Bandwidth Requirements," in *Radar Conference, 1991., Proceedings of the 1991 IEEE National*, 1991, pp. 142 –146.

[74] J. Detlefsen, A. Dallinger, S. Schelkshorn, and S. Bertl, „UWB Millimeter-Wave FMCW Radar Using Hubert Transform Methods," in *Spread Spectrum Techniques and Applications, 2006 IEEE Ninth International Symposium on*, 2006, pp. 46 –48.

[75] S. Piper, „Homodyne FMCW Radar Range Resolution Effects With Sinusoidal Nonlinearities in the Frequency Sweep," in *Radar Conference, 1995., Record of the IEEE 1995 International*, 1995, pp. 563 –567.

[76] V. Brankovic and D. Krupezevic, „Six-Port Junction Device," EP Patent EP000 000 926 812A1, 1997. [Online]. Available: http://depatisnet.dpma.de/DepatisNet/depatisnet?action=pdf&docid=EP000000926812A1

[77] H.-O. Scheck, J. Hyyrylaeinen, and O. Pulkkinen, „A Method for Implementing a Direct Conversion Receiver With a Six-Port Junction," EP Patent EP000 000 805 561A3, 1997. [Online]. Available: http://depatisnet.dpma.de/DepatisNet/depatisnet?action=pdf&docid=EP000000805561A3

[78] C. M. Potter and G. Hjipieris, „Six-Port Reflectometer Test Arrangement," EP Patent EP000 000 234 112A1, 1986. [Online]. Available: http://depatisnet.dpma.de/DepatisNet/depatisnet?action=pdf&docid=EP000000234112A1

[79] E. J. Griffin, R. J. Collier, and G. Hjipieris, „Six-port Reflectometer," EP Patent EP000 000 166 524B1, 1985. [Online]. Available: http://depatisnet.dpma.de/DepatisNet/depatisnet?action=pdf&docid=EP000000166524B1

[80] ——, „Six-port Reflectometer," EP Patent EP000 000 166 524A1, 1985. [Online]. Available: http://depatisnet.dpma.de/DepatisNet/depatisnet?action=pdf&docid=EP000000166524A1

[81] Potter and Malcolm, „Six-port Reflectometer," GB Patent GB000 002 196 745A, 1986. [Online]. Available: http://depatisnet.dpma.de/DepatisNet/depatisnet?action=pdf&docid=GB000002196745A

[82] E. J. Griffin and G. J. Slack, „A six-port reflectometer," GB Patent GB000 002 139 362A, 1984. [Online]. Available: http://depatisnet.dpma.de/DepatisNet/depatisnet?action=pdf&docid=GB000002139362A

[83] F. Ghannouchi and R. Bosisio, „Frequency Balanced Six-Port Reflectometer With a Variable Test Port Impedance," US Patent US000 005 274 333A, 1992. [Online]. Available: http://depatisnet.dpma.de/DepatisNet/depatisnet?action=pdf&docid=US000005274333A

[84] J. Yang and S. Hon, „Distance Measurement Sensor and Method of

Measuring Distance Using the Same," JP Patent JP002 007 316 066A, 2007. [Online]. Available: http://depatisnet.dpma.de/DepatisNet/depatisnet?action=pdf&docid=JP002007316066A

[85] K. M. Jee and D. C. Park, „Six-Port for Direct Conversion Receiver," KR Patent KR102 004 022 686A, 2002. [Online]. Available: http://depatisnet.dpma.de/DepatisNet/depatisnet?action=pdf&docid=KR102004022686A

[86] V. Brankovic, „Non-Coherent Six-Port Receiver," KR Patent KR102 000 068 733A, 1999. [Online]. Available: http://depatisnet.dpma.de/DepatisNet/depatisnet?action=pdf&docid=KR102000068733A

[87] Davidovitz and Marat, „Six-port Junction / Directional Coupler with 0/90/180/270 Output Phase Relationships," US Patent US000 006 674 410B1, 2002. [Online]. Available: http://depatisnet.dpma.de/DepatisNet/depatisnet?action=pdf&docid=US000006674410B1

[88] V. Brankovic, „Non-Coherent Six-Port Receiver," US Patent US000 006 363 125B1, 1998. [Online]. Available: http://depatisnet.dpma.de/DepatisNet/depatisnet?action=pdf&docid=US000006363125B1

[89] B. Huyart and F. Wiedmann, „Device for the Vector Measurement of Ultra-High Frequency Signals of the Same Angular Frequency of the Six Port Junction Type," US Patent US000 005 498 969A, 1994. [Online]. Available: http://depatisnet.dpma.de/DepatisNet/depatisnet?action=pdf&docid=US000005498969A

[90] C. Potter and G. Hjipieris, „Six-Port Reflectometer Test Arrangement and Method Including Calibration," US Patent US000 004 808 912A, 1986. [Online]. Available: http://depatisnet.dpma.de/DepatisNet/depatisnet?action=pdf&docid=US000004808912A

[91] R. Bosisio, „Method and a Six Port Network for Use in Determining Complex Reflection Coefficients of Microwave Networks," US Patent US000 004 521 728A, 1982. [Online]. Available: http://depatisnet.dpma.de/DepatisNet/depatisnet?action=pdf&docid=US000004521728A

[92] V. Brankovic, „Non-Coherent Six-Port Receiver," EP Patent WO01 999 008 426A1, 1998. [Online]. Available: http://depatisnet.dpma.de/DepatisNet/depatisnet?action=

pdf&docid=WO0019990084 26A1

[93] G. Ossberger, T. Buchegger, E. Schimback, A. Stelzer, and R. Weigel, „Non-Invasive Respiratory Movement Detection and Monitoring of Hidden Humans Using Ultra-Wideband Pulse Radar," in *Ultra Wideband Systems, 2004. Joint with Conference on Ultrawideband Systems and Technologies. Joint UWBST IWUWBS. 2004 International Workshop on*, 2004, pp. 395 – 399.

[94] M. Pichler, P. Gulden, M. Vossiek, and A. Stelzer, „A 24-GHz Tank Level Gauging System with State-Space Frequency Estimation and a Novel Adaptive Model Order Selection Algorithm," in *Microwave Symposium Digest, 2003 IEEE MTT-S International*, vol. 3, 2003, pp. 1953 – 1956 vol.3.

[95] A. Stelzer, A. Fischer, and M. Vossiek, „A new Technology for Precise Local Position Measurement - LPM," in *Microwave Symposium Digest, 2004 IEEE MTT-S International*, vol. 2, 2004, pp. 655 – 658 Vol.2.

[96] A. Stelzer and C. Diskus, „A Ka-band Distance Sensor with 0.1 Millimeter Accuracy," in *Microwave Conference, 2000 Asia-Pacific*, 2000, pp. 465 –468.

[97] A. Stelzer, C. Diskus, K. Lubke, and H. Thim, „A microwave position sensor with submillimeter accuracy," *Microwave Theory and Techniques, IEEE Transactions on*, vol. 47, no. 12, pp. 2621–2624, Dec 1999.

[98] F. Barbon, G. Vinci, S. Lindner, R. Weigel, and A. Koelpin, „A six-port interferometer based micrometer-accuracy displacement and vibration measurement radar," in *Microwave Symposium Digest (MTT), 2012 IEEE MTT-S International*, 2012, pp. 1–3.

[99] I. Skyworks Solutions, *Mixer and Detector Diodes*, 2008.

[100] F. Barbon, G. Vinci, S. Lindner, R. Weigel, and A. Koelpin, „Signal Processing Strategies for Six-Port Based Direction of Arrival Detector Systems," *International Multi-Conference on Systems, Signals and Devices (SSD), 2012 Chemnitz, Germany*, 2012.

[101] G. Vinci, S. Lindner, F. Barbon, S. Mann, M. Hofmann, A. Duda, R. Weigel, and A. Koelpin, „Six-Port Radar Sensor for Remote Respiration Rate and Heartbeat Vital-Sign Monitoring," *Microwave Theory and Techniques, IEEE Transactions on*, vol. 61, no. 5, pp. 2093–2100, 2013.

[102] T. Yakabe, F. Xiao, K. Iwamoto, F. M. Ghannouchi, K. Fujii, and

H. Yabe, „Six-Port Based Wave-Correlator With Application to Beam Direction Finding," *IEEE Transactions on Instrumentation and Measurement*, vol. 50, no. 2, pp. 377–380, 2001.

[103] S. Lindner, G. Vinci, F. Barbon, S. Mann, R. Weigel, and A. Koelpin, „Dual Tone Approach for Unambiguous Six-Port Based Interferometric Distance Measurements," in *Microwave Symposium Digest, 2013 IEEE MTT-S International*, 2013.

[104] G. Vinci, S. Lindner, S. Mann, F. Barbon, S. Linz, R. Weigel, and A. Koelpin, „Six-Port Microwave Interferometer Radar for Mechanical Vibration Analysis," in *Radar Conference (EuRAD), 2013 10th European*, 2013.

[105] R. Linbo, T. Geng, W. Jing, L. Haitao, and H. Hongfa, „Development of High-Speed Non-Contact Vibration Measurement System," in *Electronic Measurement Instruments (ICEMI), 2011 10th International Conference on*, vol. 2, 2011, pp. 244 –247.

[106] S. Piper, „Homodyne FMCW Radar Range Resolution Effects With Sinusoidal Nonlinearities in the Frequency Sweep," in *Radar Conference, 1995., Record of the IEEE 1995 International*, 1995, pp. 563 –567.

[107] S. Max, M. Vossiek, and P. Gulden, „Fusion of FMCW Secondary Radar Signal Beat Frequency and Phase Estimations for High Precision Distance Measurement," in *Radar Conference, 2008. EuRAD 2008. European*, 2008, pp. 124 –127.

[108] S. Ayhan, M. Pauli, T. Kayser, S. Scherr, and T. Zwick, „FMCW Radar System with Additional Phase Evaluation for High Accuracy Range Detection," in *Radar Conference (EuRAD), 2011 European*, 2011, pp. 117 –120.

[109] P. Pahl, T. Kayser, M. Pauli, and T. Zwick, „Evaluation of a High Accuracy Range Detection Algorithm for FMCW/Phase Radar Systems," in *Radar Conference (EuRAD), 2010 European*, 2010, pp. 160 –163.

[110] S. Ayhan, P. Pahl, T. Kayser, M. Pauli, and T. Zwick, „Frequency Estimation Algorithm for an Extended FMCW Radar System with Additional Phase Evaluation," in *Microwave Conference (GeMIC), 2011 German*, 2011, pp. 1 –4.

[111] D. Banerjee, *PLL Performance, Simulation, and Design*, 4th ed. Indianapolis, IN: Dog Ear Publishing, 2006.

[112] G. Vinci, A. Koelpin, and R. Weigel, „Employing Six-Port Technol-

ogy for Phase-Measurement-Based Calibration of Automotive Radar," in *Microwave Conference, 2009. APMC 2009. Asia Pacific*, 2009, pp. 329–332.

[113] A. Koelpin, G. Vinci, B. Laemmle, S. Lindner, F. Barbon, and R. Weigel, „Six-Port Technology for Traffic Safety: Aligning Radar Modules with the Thrust Vector of a Vehicle through Angle of Arrival Analysis," *IEEE Microwave Magazine 2011*, 2011.

[114] G. Vinci and A. Koelpin, „Verfahren und Vorrichtung zur Ermittlung einer Ausrichtung von Sensoren eines Fahrzeugs - Method for Determining Orientation of e.g. Pulsed Radar Sensor, of Sensor System that is Coupled with e.g. Distance Controller, of Vehicle, Involves Emitting Sensor Signal, and Determining Orientation of Sensor Relative to Reference Axis," DE Patent DE102 009 017 369A1, April 14, 2009. [Online]. Available: https://depatisnet.dpma.de/DepatisNet/depatisnet?action=bibdat&docid=DE102009017369A1

[115] S. Linz, G. Vinci, S. Mann, S. Lindner, F. Barbon, R. Weigel, and A. Koelpin, „A Compact, Versatile Six-Port Radar Module for Industrial and Medical Applications," *Journal of Electrical and Computer Engineering, Special Issue on Multi-Port Technology: New Perspectives and Applications - Hindawi Publishing Corporation*, 2013.

[116] C. Gu, C. Li, J. Lin, J. Long, J. Huangfu, and L. Ran, „Instrument-Based Noncontact Doppler Radar Vital Sign Detection System Using Heterodyne Digital Quadrature Demodulation Architecture," *Instrumentation and Measurement, IEEE Transactions on*, vol. 59, no. 6, pp. 1580 –1588, 2010.

[117] J. Lin, „Microwave Sensing of Physiological Movement and Volume Change: A Review," *Bioelectromagnetics*, vol. 13, no. 6, pp. 557–565, 1992.

[118] N. Andre, S. Druart, P. Gerard, R. Pampin, L. Moreno-Hagelsieb, T. Kezai, L. Francis, D. Flandre, and J.-P. Raskin, „Miniaturized Wireless Sensing System for Real-Time Breath Activity Recording," *Sensors Journal, IEEE*, vol. 10, no. 1, pp. 178 –184, 2010.

[119] K. Watanabe, T. Watanabe, H. Watanabe, H. Ando, T. Ishikawa, and K. Kobayashi, „Noninvasive Measurement of Heartbeat, Respiration, Snoring and Body Movements of a Subject in Bed via a Pneumatic Method," *Biomedical Engineering, IEEE Transactions on*, vol. 52, no. 12, pp. 2100 –2107, 2005.

[120] N. Pohl, T. Jaeschke, and K. Aufinger, „An Ultra-Wideband 80 GHz FMCW Radar System Using a SiGe Bipolar Transceiver Chip Stabilized by a Fractional-N PLL Synthesizer," *Microwave Theory and Techniques, IEEE Transactions on*, vol. 60, no. 3, pp. 757 –765, 2012.

[121] J. H. Choi and D. K. Kim, „A Remote Compact Sensor for the Real-Time Monitoring of Human Heartbeat and Respiration Rate," *Biomedical Circuits and Systems, IEEE Transactions on*, vol. 3, no. 3, pp. 181 –188, 2009.

Direction finding and ranging techniques find a large number of applications from security purposes through the medical sector to industrial automation. In this work, an innovative technique based on the Six-Port receiver principle is presented together with hardware prototypes developed by the author. Angular measurements in the range of a few milli-degrees for direction-of-arrival detection as well as a distance measurement resolution in a one-digit micrometer range have been achieved.

Gabor Vinci obtained the Bachelor's degree in Microelectronics at the University of Padua, Italy, and concluded the Master of Science in Microwave Engineering at the Technische Universität in Munich, Germany. He worked at the Daimler Research Center and at the Institute for Electronics Engineering at the University of Erlangen-Nuremberg. His PhD Studies were focused on research topics related to innovative radar technology for automotive and industrial applications. He earned his doctoral degree with „Summa cum Laude" for the work presented in this publication.

Furthermore, he authored or co-authored over 40 publications in the areas of interest and serves as a reviewer for several journals and conferences, being a member of the IEEE and MTTS. He worked on several industrial projects in different technical areas and registered three international patents. At present, he works as a Lead Engineer for R&D Industrial and Automotive Division at InnoSenT GmbH. Currently, his research interests are in the areas of microwave circuits and systems, local positioning, Six-Port technique, antenna design and short-range, high resolution radar.

ISBN 978-3-944057-16-3
9 783944 057163

FAU UNIVERSITY PRESS 2014